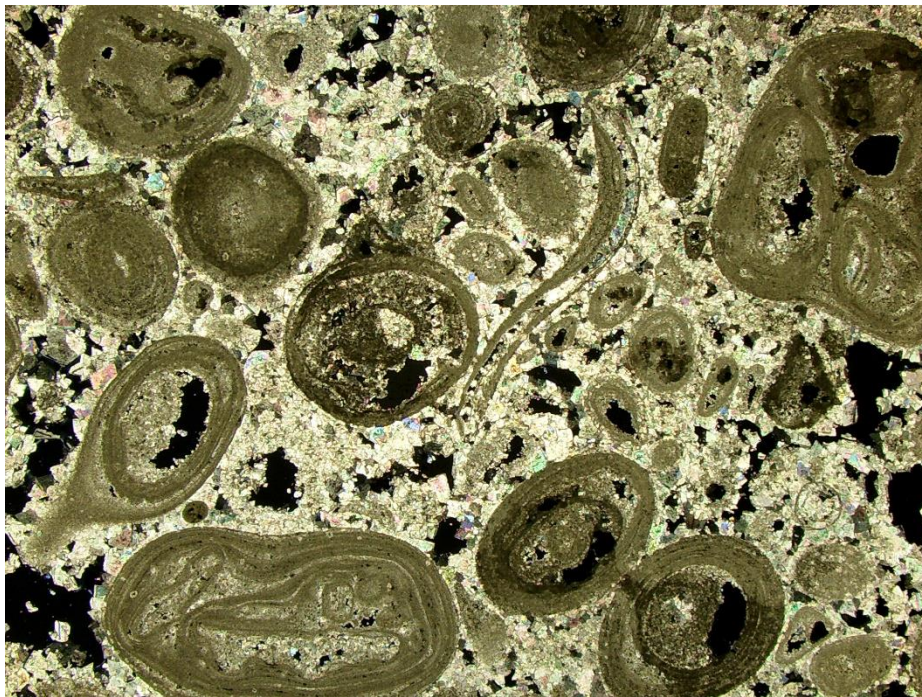


**Quantitative Petrographic Analysis of  
Carbonate Reservoir Rocks for Hydrogen  
Injection in Underground Gas Storage Facilities  
in the Netherlands: A Case Study of the Z3-  
Zechstein Reservoirs of Alkmaar Field**



**Ta-Kai Wang**  
**Student Number: 7045913**

MSc Earth's Structure and Dynamics  
Department of Geoscience  
Utrecht University

May 2022



## 1. Abstract

Sustainable energy development is a potential solution for replacing fossil fuel power stations to reduce the CO<sub>2</sub> emission and lower the rate of global warming scale. However, sustainable energy is often intermittent. Underground Hydrogen Storage (UHS) is a potential solution for sustainable energy storage. UHS is usually operated in salt caverns or depleted gas/oil fields. This research focuses on the depleted carbonate (Zechstein 3 carbonate group) gas field in Alkmaar (Boekelemeer (BKLM)-01 and -04 wells). The study aims to understand the UHS potential of the Alkmaar field by understanding the characterization and inferred hydrogen injection impact of the reservoir and non-reservoir rocks and the overall potential impact on Zechstein 3 hydrogen storage. To do so, two stratigraphic logs from BKLM-01 and BKLM-04 were created. Then twenty-five samples (ten from BKLM-01; fifteen from BKLM-04) were selected for quantitative analysis. Integrating well logs (wireline), sedimentology and quantitative petrography was done with EasyTrace (IFPEN) software, leading to simplified correlation and characterization of the reservoir and sealing layers within the observed Z3 interval. Finally, a literature review about hydrogen impact on reservoirs to apply to this case. The result shows that the entire well cores from both wells generally have good reservoir properties. Then the research concludes with the potential of the Z3 carbonate reservoir and internal sealing at the Alkmaar/Boekelermeer field and the uncertainties and future studies. The best reservoir properties in BKLM-01 are at 1978-1989m depth and 1972-1998m depth in BKLM-04. And water-saturated layers can be found in the reservoir and might potentially be internal sealing. The geochemical reaction in the reservoir might consume the injected hydrogen, and precipitation might lead to well reservoir clogging. However, the geochemical reaction is buffered by carbonate rock. Furthermore, hydrogen does not dissolve in the formation water in the reservoir. Hence, the pH value does not change in the reservoir. Therefore the clay swelling is limited. It can be boldly assumed that the impact of hydrogen injection is not significant enough to lead to a high risk for long-term hydrogen storage, and the internal sealing has low potential. However, there are many uncertainties remain. For example: the correlation of the well in the Alkmaar field, microbial in carbonate reservoir, reservoir integrity, and faults. Furthermore, evaluating the economic value hydrogen storage in Alkmaar before the injection is also important.



# Contents

1. Abstract.....	1
2. Introduction.....	3
3. Geological and Tectonic Background of the Netherlands, the Southern Permian Basin (SPB) and Zechstein 3 (Z3) Members.....	5
3.1. Ordovician to Carboniferous: The creation of Laurussia .....	7
3.2. Late Paleozoic: Late Carboniferous to Permian .....	8
3.3. Mesozoic.....	11
3.4. Tertiary.....	14
3.5. Zechstein 3 Formation Lithology .....	14
3.6. Groundwater Chemistry and Potential Hydrogen Impact.....	18
4. Methodology .....	22
4.1. Part 1: Quantitative Petrography.....	22
4.2. Part 2: Well Data Analysis and Correlation .....	25
4.3. Part 3: Hydrogen Impact on Reservoir .....	25
5. Result.....	27
5.1. Stratigraphy and Sedimentology.....	27
5.2. Quantitative Petrography .....	39
5.3. Well Data Analysis and Correlation.....	74
5.4. Hydrogen Impact on Reservoir .....	78
6. Discussion .....	80
6.1. Characterization and inferred impact of the reservoir rocks.....	80
6.2. Characterization and inferred impact of the non-reservoir rocks .....	81
6.3. Overall potential impact on Z3 carbonate hydrogen storage .....	82
7. Conclusion.....	84
8. Reference.....	86



## 2. Introduction

Energy and electrical power are crucially critical for economic development. However, the pollution and the CO<sub>2</sub> emission caused by the energy industry have impacted the environment severely. The atmospheric CO<sub>2</sub> levels rose from pre-industrial levels of 280 ppm to 387 ppm in 2005 (Hangx et al., 2015). In 2020, the CO<sub>2</sub> concentration is 471 ppm (CarbonBrief, 2021). The rise of atmospheric CO<sub>2</sub> levels leads to global warming and extreme weather, damaging the ecosystem and society. Hence, developing sustainable energy is a vital task for researchers. The electricity generated by sustainable energy is often intermittent. Therefore, energy storage is essential to optimize and successfully manage hybrid energy systems. Mass underground hydrogen storage (UHS) is a potentially viable method to store sustainable energy and assist renewable energy production (e.g., wind, solar) in stabilizing the overall output and achieving societal demands. However, the impacts of the injected hydrogen on the reservoir rock properties are poorly understood to date. Heinemann et al. (2021) highlighted the major challenges for large-scale storage of hydrogen in porous media, including the impacts of at least three principal geochemical reactions: (1) dissolution and/or precipitation of mineral species resulting in enhanced or reduced reservoir porosity (hence causing changes in injectivity and productivity); (2) dissolution and/or precipitation of mineral species affecting the sealing integrity of caprocks (i.e. potentially leading to loss of containment); and (3) diagenesis altering the mechanical properties of the reservoirs and caprocks.

According to Juez-Larre et al. (2019), there are two types of underground storage capacities. The first one was the theoretical capacity, which is the total storage capacity (Gas-Initially-in-Place. GIIP), and the second type was effective capacity, which had to fulfil the technical and economic value. Furthermore, the theoretical capacity only applied to the gas field, which fulfilled the following criteria: 1. Developed and accessible through production wells at the time of evaluation; 2. A minimum depth of 1000m; 3. No significant amount of H<sub>2</sub>S (<< 10ppm); 4. Permeability higher than 0.1 mD; 5. not being used as storage yet. (Juez-Larre et al., 2019). This research has targeted the depleted gas field at Alkmaar for the following reasons: The reservoir rock at the Alkmaar field belongs to Zechstein 3 (Z3) carbonate group. The information of the Alkmaar field is documented by Acoma Netherlands B.V. while performing the gas operation. The targeted Z3 carbonate is located below 1950m depth. Furthermore, according to Acoma Netherlands B.V. well report, there is no significant H<sub>2</sub>S in the field, and the permeability is between 1-100 mD. And most importantly, the field has not been used as storage yet.

To understand the potential impact of the injected hydrogen on the reservoir properties, particularly on carbonate rocks, this research will evaluate and analyze well cores from the Z3 reservoir intervals Boekelemeer-01 and -04. This research consists of three parts: (1)



Sedimentary/Stratigraphic Logging and Quantitative Petrography/Diagenesis; (2) Well Data Analysis and Correlation; (3) Potential Geochemical Reactions. In part one, the quantitative petrography was done by microscopic analyses of thin sections and the quantification under JMicroVision. In the second part, the correlation of the reservoir intervals was done by using EasyTrace (IFPEN) software, including the assessment of flow properties across the reservoir interval through well-data (cores, logs). Henceforth, a quantitative characterization of the most optimal reservoir interval within Z3 Zechstein and the possible internal seals (less permeable layers) has been achieved on both Boekelemeer-01 and -04 wells. In the third part, the possible geochemical reactions resulting from increasing hydrogen content to 0.5%, 10%, and 100% were deduced, resulting in conceptual models and highlights for the investigated reservoir: (1) Inferred impact of hydrogen storage on reservoir rock intervals; (2) Inferred impact of hydrogen storage on internal non-reservoir layers; and (3) Overall potential impact on hydrogen storage in Zechstein Z3 reservoirs. With the information provided by this research, the potential of hydrogen storage at the Alkmaar field and its possible impacts are at least partially revealed. Further work, including reservoir and geochemical modelling, may find the results of this research study beneficial. The same approach can also be applied (and upgraded) to investigate other similar carbonate reservoirs that might host hydrogen in the future for sustainable energy underground storage.

### 3. Geological and Tectonic Background of the Netherlands, the Southern Permian Basin (SPB) and Zechstein 3 (Z3) Members

Currently, there are six operational (June, 2022) underground natural gas storage facilities in the Netherlands (figure 3.2), four of them are within porous reservoirs (Grijpskerk, Norg, Bergermeer, and Alkmaar), and two are within salt caverns (Zuidwending and Heiligerlee), and figure 3.1 shows the area of oil/gas reservoir and salt cavern. This research will focus on the carbonate porous reservoir at Alkmaar UHS (Zechstein 3 (Z3) carbonate group), also known as Alkmaar Piekgasinstallatie. The technical details of the Alkmaar gas storage are shown in Table 3.1. The Z3 carbonate member consists of brownish dolomitic limestone or coarse-crystalline dolomite (Plattendolomit). It is around 50 m thick and lies at 1900 to 2100 m depth. The porosity of the rock can be at most 20%, but the pore space is poorly connected, so the permeability is less than 10 mD. The underground gas storage (UGS) facilities in the Netherlands (Alkmaar Field) will increase the hydrogen admixture content to the stored natural gas (DBI GUT, 2017). However, no associated quantitative petrographic and reservoir characterization work has been done to our knowledge. Furthermore, previous studies have not targeted a quantitative assessment of mineral/fluid interaction in the reservoir, particularly the reactions that might occur upon injecting hydrogen.

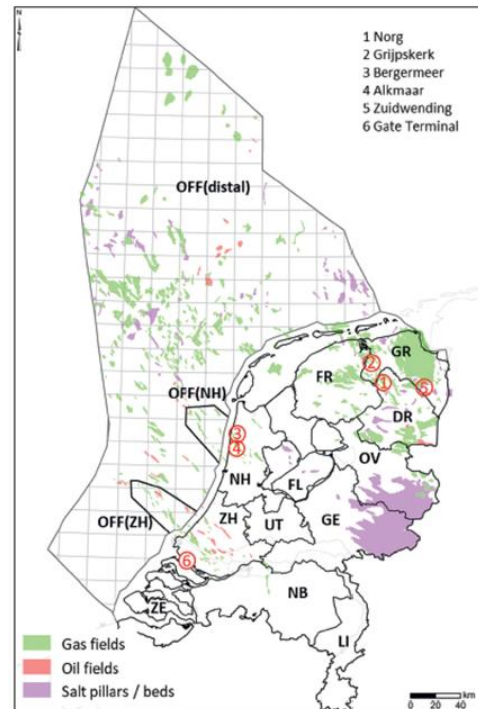


Figure 3.1. Gas/oil fields and salt caverns of the Netherlands. (Juez-Larré, et al., 2019)

Table 3.1. Technical details of Alkmaar gas field (Juez-Larre, et al., 2019).

Location	Storage	Start year	Working/cushion volume (billion m <sup>3</sup> )	Production/injection capacity (million m <sup>3</sup> /day)	Number of wells
Alkmaar	Gas field	1997	0.5/3.1	36/4	9

The targeted UGS reservoir, the Zechstein 3 (Z3) carbonate at Alkmaar, is part of the Zechstein Carbonates deposited under the marine environment during the Late Permian. The Zechstein Carbonate group is part of the South Permian Basin (SPB) (figure 3.3), which is the largest sedimentary basin and a long-term focus of oil and gas reservoirs in Europe (Doornenbal et al., 2010). SPB crosses over Northern Poland, Northern Germany, Denmark, Netherlands, and part of England. In the south of SPB, the basin is in contact with Rhenish and Bohemian massif, which are part of the Variscan Orogen. To western margin of the basin is outlined by the Variscan Thrust Belt, and the basin sits on top of the Precambrian European Craton at the east.



Although the deposition happened during the Permian, the tectonic events presented in the modern setting occurred post-Permian. The earliest event that eventually led to the formation of SPB can be traced back as early as the Early Ordovician (Ter Borgh et al., 2018). The evolution of the SPB is described below, in chronological order.



Figure 3.2. Location map of underground gas storages in the Netherlands (DBI GUT, 2017)

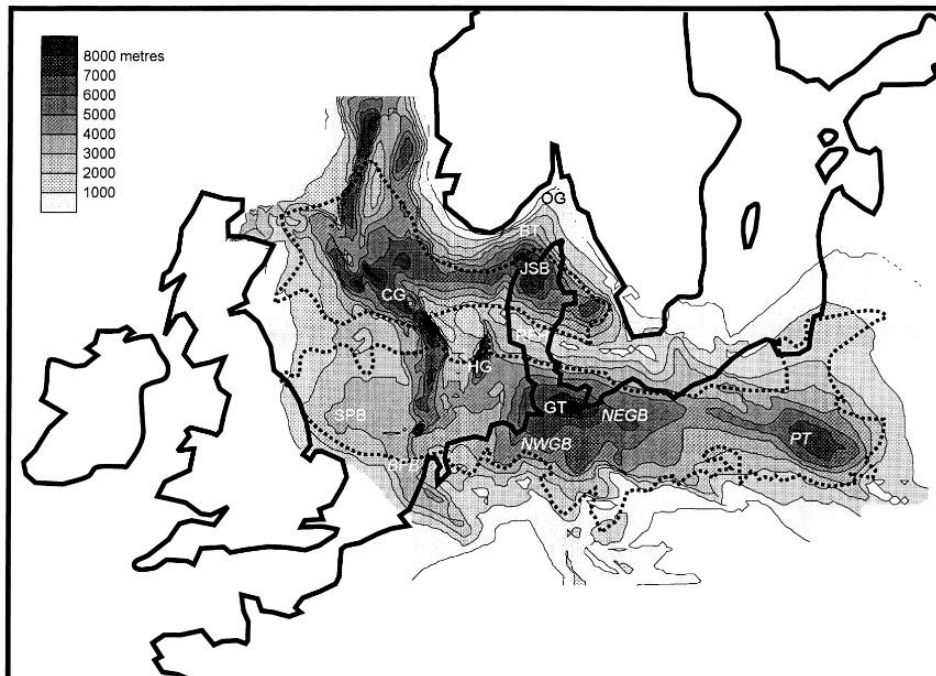


Figure 3.3. Map of SPB. SPB spreads across from North Sea through the Northwestern Europe to Poland (van Wees et al., 1999).

### 3.1. Ordovician to Carboniferous: The creation of Laurussia

The Netherlands is often considered a part of the Avalonia microcontinent. Avalonia detached and moved northward from Gondwana during rifting in the Early Ordovician (figure 3.4), which led to the opening of the Rheic Ocean. The northward movement continued, and at the end of Ordovician, Baltica and Avalonia collided, which led to the closure of the Tornquist Ocean. Later in Silurian and Early Devonian, Laurentia collided with Baltica and Avalonia, which led to the closure of the Iapetus Ocean and the formation of the new continent, Laurussia.

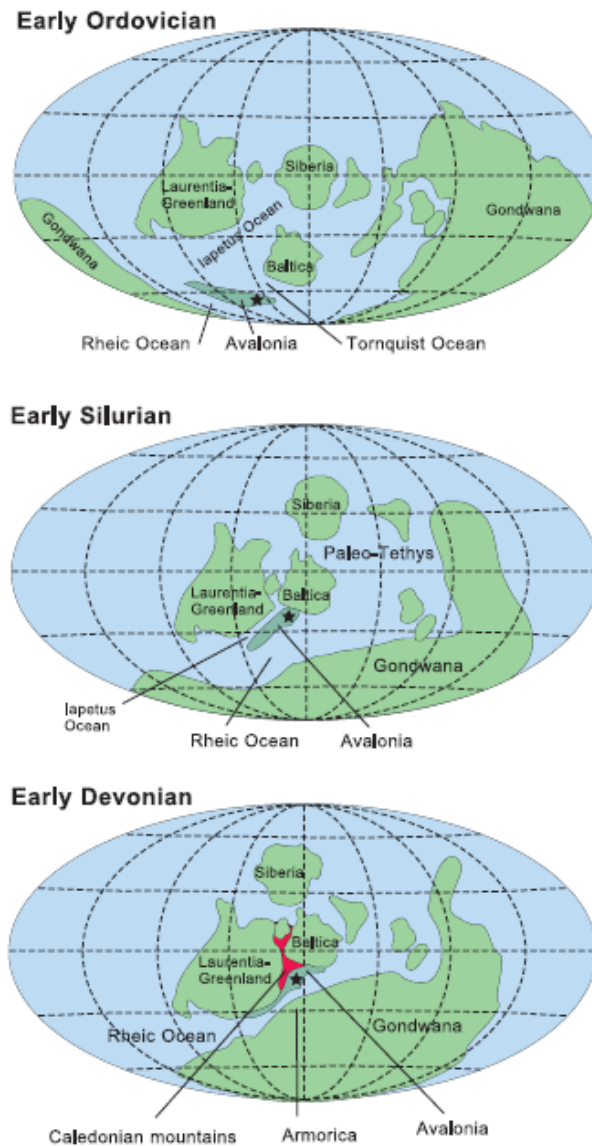


Figure 3.4. Map of Iapetus Ocean (Geluk et al., 2007)

During Late Devonian and Early Carboniferous, Laurussia and Gondwana started to collide with each other in a clockwise rotation and formed the Variscan Orogeny (figure 3.5(C)). The extension of the subducting slab was documented in the Rheno – Hercynian, Saxo – Thuringian, and Moldanubian belts. Furthermore, the opening of the Rheno – Hercynian Ocean Basin might be caused by the subsidence of the mid-ocean ridge in the Rhenic Ocean or mantle plumes

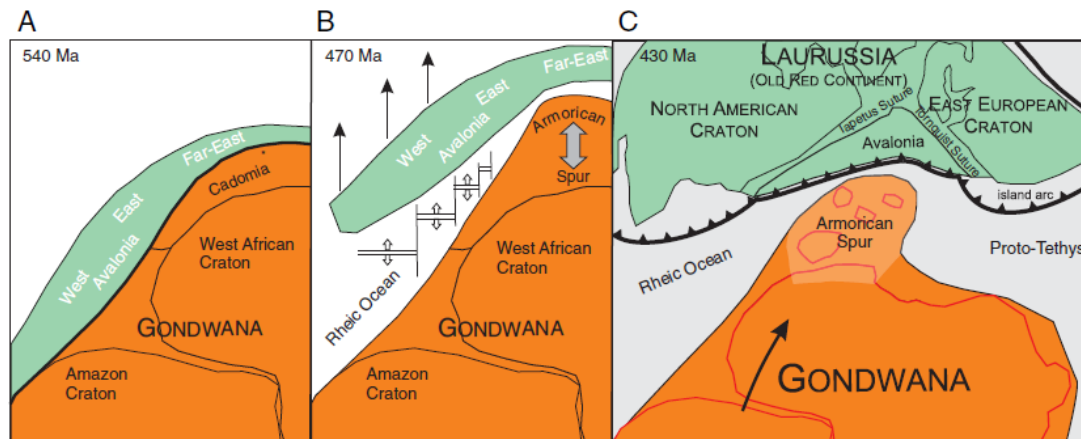


Figure 3.5. The evolution of the Armorican Spur coeval with the post-Cadomian formation of the Rheic Ocean in peri-Gondwana (A, B) is eventually followed by the subduction of the Rheic Ocean during convergence between Laurussia and Gondwana (C) (Kroner & Romer, 2013)

under eastern and central Europe (Franke, 2015). There were three different high-pressure events during the formation of the Variscan Orogeny, which were Variscan Subduction Zone Systems I, II, and III (VSZS I, II, and III) (Kroner & Romer, 2013). During VSZS I in Silurian, the collision resulted in the closure of the Rheic Ocean, in which the Laurussia Plate with an island arc constituted the upper plate, and the subducting oceanic Gondwana Plate was the lower plate. The Earliest Variscan high-pressure subducting event was preserved in the units of Iberia, France, and the Bohemian Massif. Later the Cadomian Block of Brittany collided with the Midland Micro Craton and resulted in the Early Variscan event, the Acadian Orogeny of Anglo-Brabant Massif (Kroner & Romer, 2013). The VSZS II was characterized by subduction of the Gondwana plate beneath the Cadomian Block. The continuous subducting of the Gondwana Plate led to the opening of the Paleotethys and the continued closure of the Rheic Ocean (figure 3.6(E)). Furthermore, the upper Gondwana plate partly overrode the former plate boundary zone and overprinted the previous Variscan record (Kroner & Romer, 2013). The final phase of the subduction (VSZS III) (340 Ma) was described by the continent-continent collision, which was driven by the Central Bohemian Shear Zone, which constituted a transform plate boundary linking the subduction zone of the Bohemian Massif with the intra-continental subduction zone (figure 5.2F) (Kroner & Romer, 2013). The driven forces on the continuously subducting Gondwana were the ridge push of the active Paleotethys ridge and slab pull of the subducting Rheic Ocean outside the Variscan Orogeny. The continuous collision of the two-plate led to the initiation of lithospheric scale dextral and sinistral shear zone (figure 3.6) (Kroner & Romer, 2013).

### 3.2. Late Paleozoic: Late Carboniferous to Permian

During the Late Carboniferous to Early Permian, due to the ongoing NW trending dextral strike-slip faults and subordinate NNE striking sinistral faults, the crustal shortening and the collapse of the Variscan Orogen occurred. The westward movement of Gondwana led to the opening of

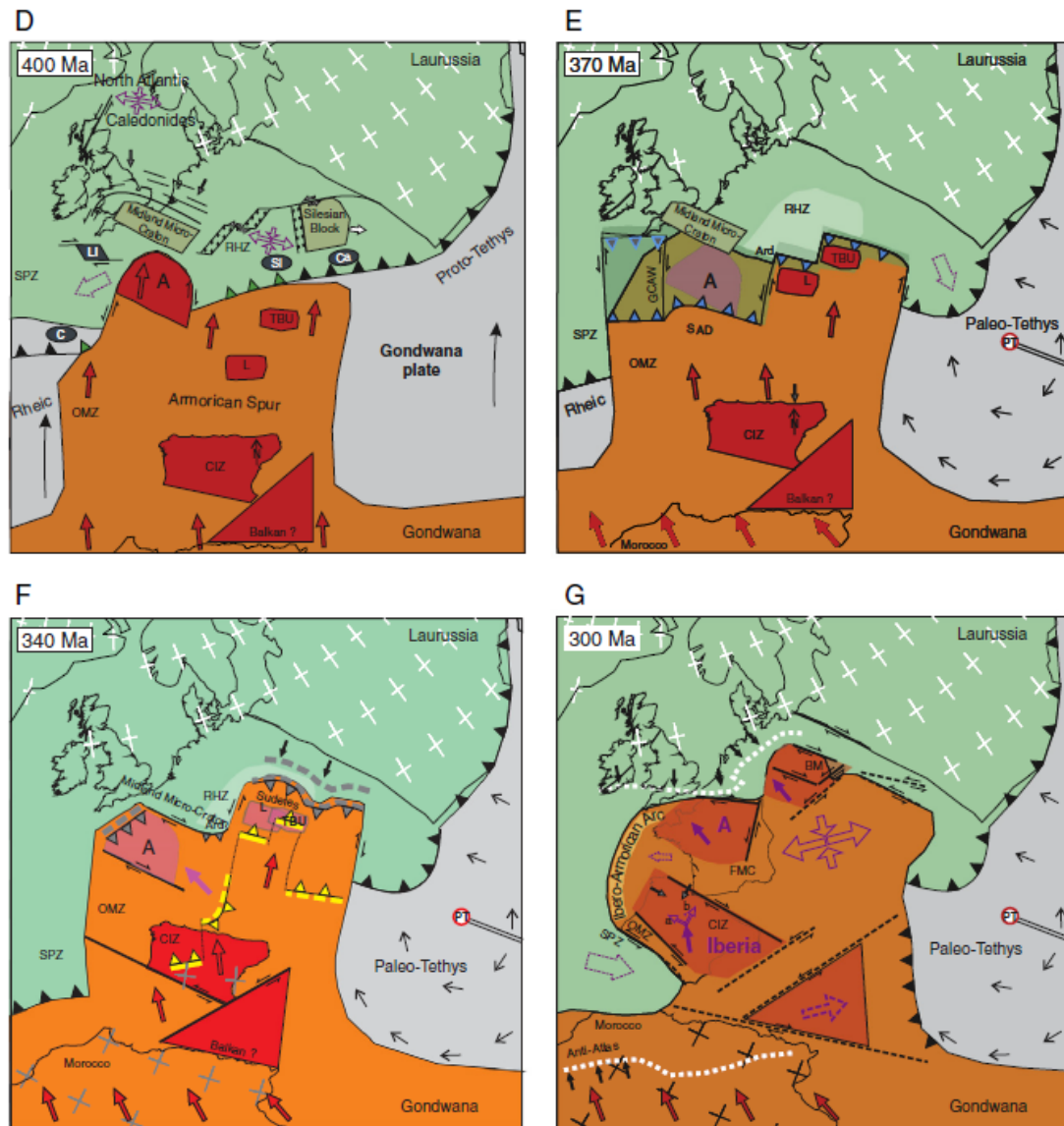


Figure 3.6. (D) Initial collision of the Armorican Spur and Laurussia between Armorica and the Midland Micro-Craton respectively. (E) Variscan subduction accretion stage and the evolution of the Variscan Subduction Zone System 2 (VSZS II: blue triangles). (F) Intracontinental subduction stage at 340 Ma. Note that the subduction zones of the Variscan Subduction Zone System 3 (VSZS III: yellow triangles) are spatially unrelated to the VSZS I and VSZS II. (G) Late-Variscan transpressional stage of the orogeny. (C — Careón; Li — Lizard; SI — Sleza; Ca — Carpathian; TBU — Teplá-Barrandian Unit; L — Lausitz; CIZ — Central Iberian Zone; OMZ — Ossa Morena Zone; SPZ — South Portuguese Zone; RHZ — Rheno-Hercynian Zone.) (Kroner & Romer, 2013)

the Paleotethys Ocean (Franke, 2015). During the same period, the subducting lithospheric slab on Gondwana detached from the orogen, which led to the wrench-induced collapse and caused an upwelling of the asthenosphere, thermal thinning and partial delamination of lithospheric mantle and regional uplift (Doornenbal, H., 2010). Furthermore, due to the volcanism and associated wrench tectonics during the Early Permian, SPB started to form and begin to subside in response to thermal contraction of the lithosphere. The modern-day Southern North Sea basin was dominated by the thermal subsidence and its gradual incorporation into the westward

expanding Rotliegend basin, where the Rotliegend sandstone dominates the oldest part of the Southern Permian Basin (SPB). By Mid-Permian, the thinning and mechanical stretching of the crusts continued, and the regional erosional unroofing led to the formation of the Base Permian (Variscan) Unconformity (BPU).

The Late Permian tectonic setting of Europe was dominated by the continuous northward subduction of the Paleotethys Ocean beneath the southern margin of Europe. The Arctic – North Atlantic Rift System and the glacioeustatic sea level rise facilitated the development of a seaway linking the Arctic Ocean with the Permian Basin of Western to Central Europe. The area of the SPB was flooded very rapidly (Glennie, 1998) and formed a large inland sea where Zechstein carbonates and evaporites deposited in 5 cyclical sequences, as shown in figure 3.6. (TNO-NITG, 2004). Z1 sediments are shales of copper shale member and a large anhydrite platform-covered area that was heavily affected by volcanic activities. Z2 was an extensive carbonate platform with lagoons and shoals. Moving toward the southern part of the unit, the unit was covered by river system, mud flats, sabkhas, and salt lakes. And a sudden fall of sea level allowed evaporite layers of halite, and gypsum to accumulate. A carbonate – anhydrite platform covered most of the area around the Texel – IJsselmeer High, and carbonate deposition prevailed in the southern part of the Netherlands. The Z3 salt was deposited in the modern-day

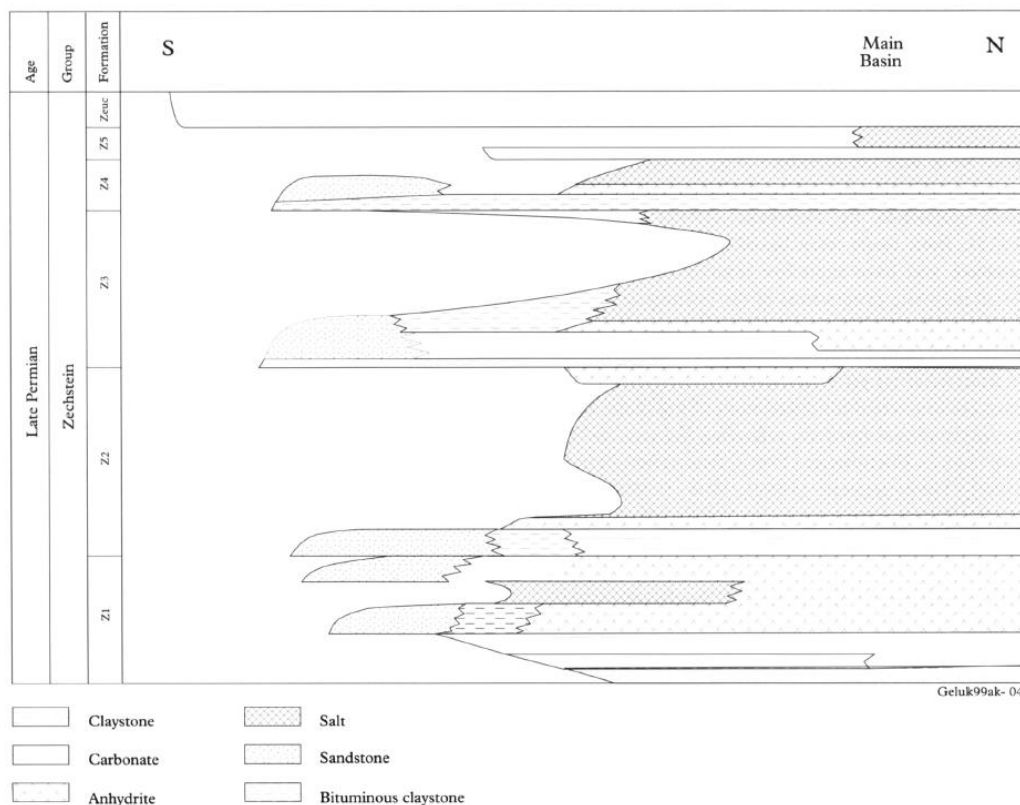


Figure 3.7. Schematic stratigraphic diagram of the Zechstein Group (Late Permian) from basin fringe to basin centre. The carbonates discussed in the present contribution occur in the Z1, Z2 and Z3 Formations. Z1: Z1 (Werra) Formation; Z2: Z2 (Stassfurt) Formation; Z3: Z3 (Leine) Formation; Z4: Z4 (Aller) Formation; Z5: Z5 (Ohre) Formation; ZEUC: Zechstein Upper Claystone Formation (Geluk, 1999).

NE Netherlands, where the depositional layer for Z3 salt is completely dried out and accumulated highly soluble magnesium salts, which are not known from any other part of the SPB. Z4 and Z5 units were hypersaline. 4 units started as marine sediments but gradually changed into a playa lake, and the Z5 unit started as a playa-type plain.

### 3.3. Mesozoic

#### 3.3.1. Triassic

Early Triassic deposits are often considered the continuous formation within the Southern Permian Basin. There are two phase of extensional tectonic events which happened during the Triassic (figure 3.8). The first one was The Hardegsen Phase (Early Triassic), where the Variscan tectonic elements were reactivated (TNO-NITG, 2004). The second phase was The Early Kimmerian phase (Late Triassic). The evidence of the extensional phase can be spotted on the ESE-WNW trending fault at Netherlands Swell, and the extension continued until the Cretaceous.

Early Triassic deposits were similar to the Zechstein group, where the deposition happened in a large continental basin. The oolites in the brackish water were found in a high-energy environment during periods when the influx of clastics was limited (Peryt, 1975), which led to the formation of the Main Buntsandstein Group. The oolites and fine-grained interbedded deposits suggest that the environment experienced episodic sea-level changes. The Main Buntsandstein Group was massively eroded after the tectonic uplift, which resulted in the Hardegsen Unconformity below the Solling Formation (figure 3.9). The Solling Formation is a series of claystone deposited in

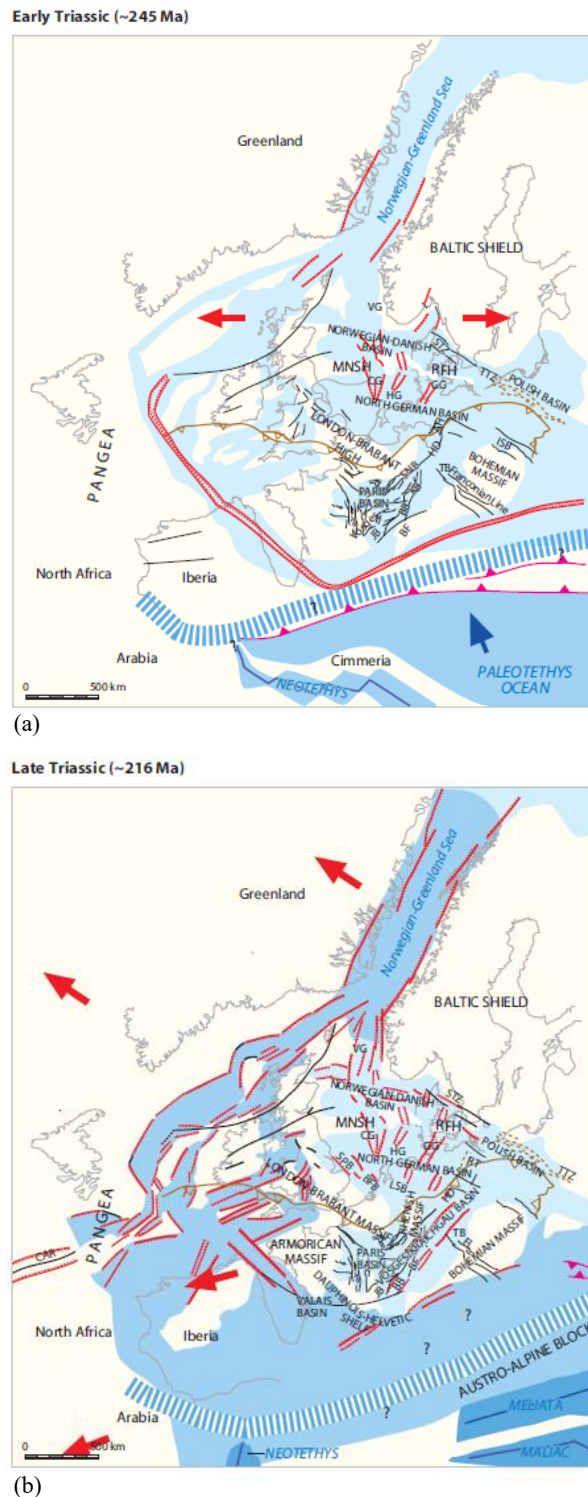


Figure 3.8. Structural overview map of: (a) Early Triassic; (b) Mid-Late Triassic (Doomenbal, H., 2010).



a marine environment. After the rifting, the inland sea was separated from the Paleotethys Sea, salt and evaporite deposited as the Rot Evaporite Group. When the inland oceans were reconnected, the clastic sedimentation deposited in the inland sea was replaced by the carbonate-dominated deposition of the Muschelkalk Formation (TNO-NITG, 2004).

Uplift of the Fennoscandian Shield during the Mid-Late Triassic generated a supply of clastic material, which led to the termination of carbonate sedimentation and brought about the clastic sedimentation at the base of the Keuper Formation. Later, during the Early Kimmerian Phase, rapid subsidence created the Ems Low. Meanwhile, the Brabant Massif and the surrounding areas were uplifted, which resulted in widespread erosion. The last Rhaetian transgression caused a long period of marine deposition, which continued until the Mid-Jurassic.

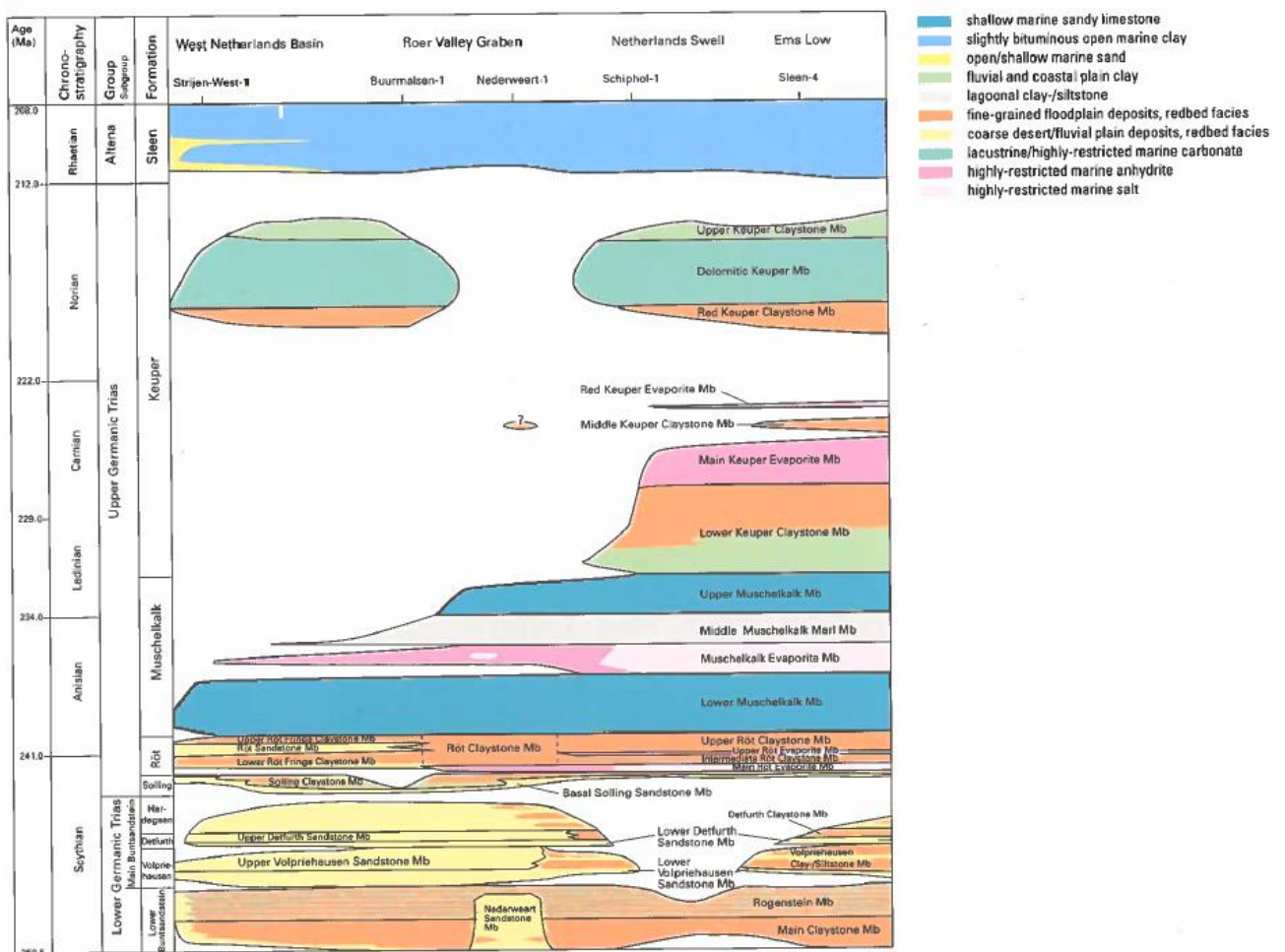


Figure 3.9. Schematic stratigraphic diagram for the Triassic (Van Adrichem Boogaert, and Kouwe, 1993)

### 3.3.2. Jurassic

During Late Triassic, the environment turned from continental/shallow marine to an open marine environment, Altena Group, which extended over a large part of NW Europe. In the eastern part of the Netherlands, the transgressive deposits in the Late Triassic–Early Jurassic sit uncomfortably above the Muschelkalk Formation. During the Early–Mid Jurassic, the thermos-

hyaline layering of the water in the marine circulation system resulted in the deposition of the Bituminous clays of the Posidonia Shale Formation in NW Europe (TNO-NITG, 2004). During Mid-Late Jurassic, the open marine environment turned into a shallow marine environment again. At the same time, the break-up of the Pangea and the opening of the Atlantic Sea continued.

The Late Jurassic – Early Cretaceous tectonic movement was marked by the Late Kimmerian rifting phases, which were associated with mafic volcanic rocks. The phases were similar to the Permo-Triassic extension, with an increased tendency toward extensional reactivation of E-W trending Variscan thrusts (figure 3.10). The extensions were ubiquitously N-S and strongly suggested a dominantly N-S extensional stress field (Chadwick et al., 1989).

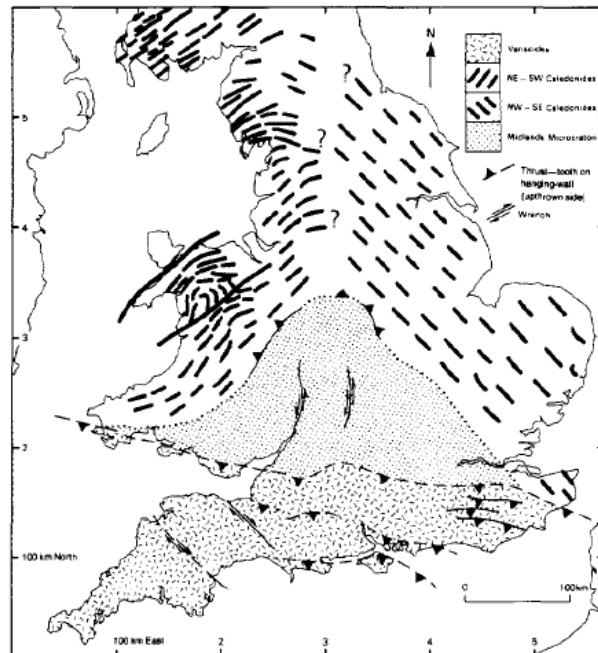


Figure 3.10. Structural elements of the orogenic basement of southern Britain. Grid shows 100 km ticks from British National Grid origin (Chadwick et al., 1989).

### 3.3.3. Cretaceous

Due to the rising sea level in the Early Cretaceous, combined with subsiding cooling crust during the Late Kimmerian post-rift phase, a large transgression spread across NW Europe deposited the coastal sand and clays (TNO-NITG, 2004). During the Aptian, brief regression and Austrian tectonic pulse led to the deposition of greensands along the margins of the West and Central Netherlands Basins. At the end of Albian, the tectonic events were less significant. The highs in Europe were gradually flooded by the transgression, the supply of clastic sediments decreased, and the deposition contained more marl. Later, the rapid sea-level rise during the Later Albian and Cenomanian Flooded the original clasts in Europe. By the end of the Cenomanian, the sea level reached the temporary maximum, which led to an anoxic environment and organic-rich deposits. Entering the Late Cretaceous, during the Coniacian, the collision between Europe and Africa started and initiated a compressive tectonic event. The tectonic event was the inversion of the Late-Jurassic to Early Cretaceous faults. The inversion occurred with two series of pulses, the first one was the Sub-Hercynian pulse during Coniacian, and the second one was the Laramide pulse at Early Tertiary (TNO-NITG, 2004).

### 3.4. Tertiary

The opening of the Atlantic Ocean continued, as well as the collision of the Eurasian and African Plates, which resulted in the formation of the Alpine Orogeny. After the Laramide pulse in the Paleocene, the deposits at the North Sea were a series of a transgressive marine succession of siliciclastic sediment. During the Eocene, the environment turned to near shore with coastal sands and clays. The volcanism during the Early Eocene covered NW Europe with tuff, which made a good marker horizon for regional correlation (TNO-NITG, 2004). Entering Oligocene, a vast, shallow sea covered the Netherlands and formed uniformed marine deposits. During Oligocene-Miocene, the final inversion, Savian Tectonic Phase, caused regional uplift and low sea level, which led to regional erosion of Upper Oligocene sediments. Finally, the modern position of the Netherlands was accentuated during the Miocene and Pliocene.

### 3.5. Zechstein 3 Formation Lithology

The targeted potential reservoir for hydrogen storage is the Zechstein 3 Carbonate member (ZEZ3C), which is in a wider Zechstein 3 (Leine) (Z3) Formation (figure 3.11) at the Southern Permian Basin (SPB). The SPB became a land-locked brine-filled depression and was isolated from the sea during the Z3 Formation (as mentioned above). The thickness of the Z3 formation is roughly up to 350 m. From bottom to top, the Z3 Formation can be separated into seven layers (figure 3.12), Salt Clay Member (ZEZ3G), Z3 Carbonate Member (ZEZ3C), Z3 Main Anhydrite Member (ZEZ3A), Z3 Anhydrite-Carbonate Member (ZEZ3B), Z3 Salt Member (ZEZ3H), Z3 Fringe Claystone Member (ZEZ3U), and Z3 Fringe Sandstone Member (ZEZ3S), where Z3 Carbonate Member is the concern of this research.

The ZEZ3G was a series of grey claystone with high gamma ray response and corresponding low velocity on sonic log. It was deposited in a shallow marine transgressive unit at the base of the 3<sup>rd</sup> evaporite cycle of the Z3 Formation (figure 3.12(a)). Above the Salt Clay Member is the Z3 Carbonate Member (ZEZ3C), which was the most important transgression of the Zechstein Formation (figure 3.12(b)). It flooded the entire basin margin area of the SPB (Geluk, 2000), and almost all the Z3 carbonates were dolomitized (Van Der Baan, 1990).

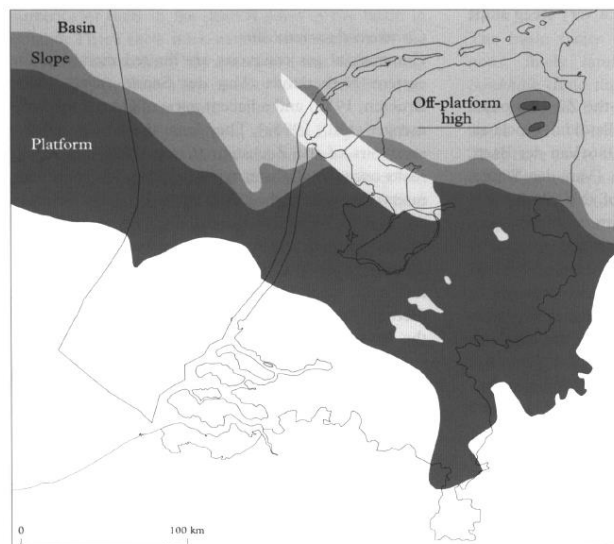


Figure 3.11. Facies map of the Z3 carbonate Member. The light areas in the onshore part of the map are highs where the Zechstein were eroded in Late Jurassic to Early Cretaceous (Van Der Baan, 1990).

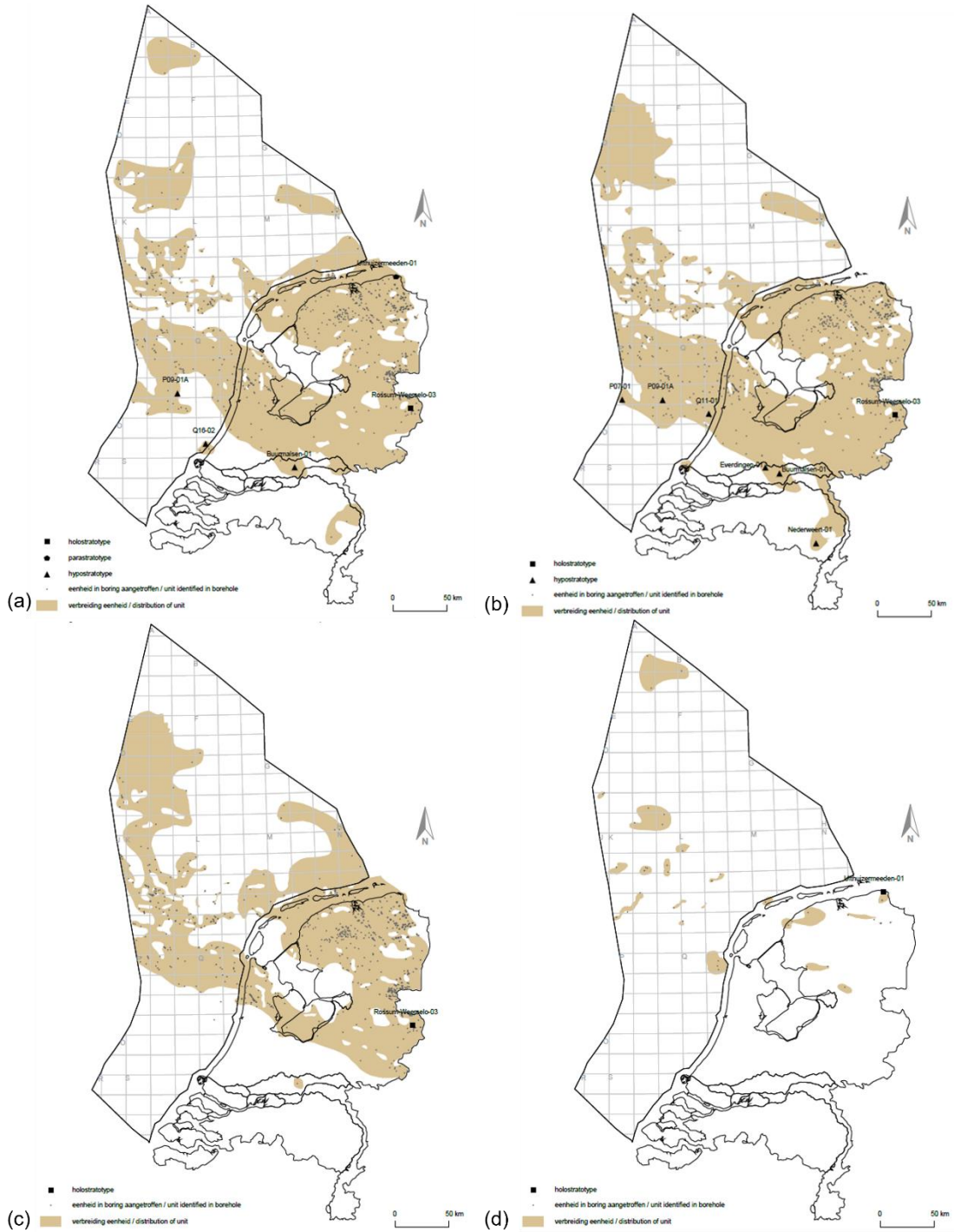


Figure 3.12 Geographic Distribution of Z3 Formation. (a) Grey Salt Clay Member (ZEZ3G); (b) Z3 Carbonate Member (ZEZ3C); (c) Z3 Main Anhydrite Member (ZEZ3A); (d) Z3 Anhydrite-Carbonate Member (ZEZ3B); ■: Holostatotype; ●: Parastratotype; ▲: Hypostratotype; ·: unit identified in boreholes; the brown colored area is the distribution of the unit.



Figure 3.13. Geographic Distribution of Z3 Formation. (e) Z3 Salt member (ZEZ3H); (f) Z3 Fringe Claystone Member (ZEZ3U); (g) Z3 Fringe Sandstone Member (ZEZ3S); ■: Holostatotype; ●: Parastratotype; •: unit identified in boreholes; the brown colored area is the distribution of the unit.



ZEZ3C can be separated into three facies, basin facies, slope facies, and Platform facies (figure 3.11). The basin facies comprised a dark-coloured limestone that was not easy to distinguish from Main Anhydrite Member above (Geluk, 2000); the slope facies were composed of laminated and bioturbated carbonates and silty dolomites. However, the slope facies were very well developed during Z3 carbonate formation; the platform facies consisted mostly of grey microcrystalline dolomite and algal boundstones (Geluk, 2000). The platform deposits were related to near-surface, shallow marine diagenesis. In the early phase of diagenesis, carbonate deposits from restricted platform facies were characterized by hypersaline groundwater, resulting in rapid porosity destruction through dolomite cementation and anhydritization (Van Der Baan, 1990). The large, interconnected pore network in grain-supported Z3 carbonates acted as pathways for various diagenesis fluids such as meteoric water and hypersaline brines. These fluids caused porosity destruction by dolomite and anhydrite cementation or porosity enhancement through leaching (Van Der Baan, 1990). Furthermore, at deep burial environment, calcification might also occur. Calcitization with dolomite leaching at the upper layers and the availability of carbon dioxide in the reservoir weakened the carbonate minerals.

The Z3 Main Anhydrite Member (ZEZ3A) above the Z3 Carbonate member was formed under a playa/sabkha environment. Hence, the layer was relatively pure anhydrite, often with dolomite or claystone intercalations (figure 3.12(c)). The original limestone was completely replaced by dolomite through a very early stage of reflux of hypersaline brines. And the variation within the layer can be explained by river water influx during episodic exposure events associated with regional or global sea-level fluctuations (Peryt & Scholle, 1996). Furthermore, the Z3 carbonate at Alkmaar/Boekelermeer is around 80°C (GBI DUT, 2017). Above ZEZ3A is the Z3 Anhydrite-Carbonate Member, which is similar to the previous sequence, but this sequence composed anhydrite- carbonate interbedding. Furthermore, ZEZ3B only appeared at limited area of the northern Netherlands and offshore region (figure 3.12(d)). Moving on to the next sequence, the Z3 Salt Member (ZEZ3H) was a pure K-Mg rich salt layer consisting of grey/reddish halite deposited in a deep saline marine environment (figure 3.13(e)). The layer also included magnesium sulfate monohydrates like kieserite ( $\text{MgSO}_4 \cdot \text{H}_2\text{O}$ ), and hydrous chloride minerals such as carnallite ( $\text{KMgCl}_3 \cdot 6\text{H}_2\text{O}$ ) and bischofite ( $\text{MgCl}_2 \cdot 6\text{H}_2\text{O}$ ). Suppose the hydrogen leached from the potential storage in the Z3 Carbonate Member. In that case, the hydrogen might react with the salt member and release toxic gas such as hydrogen chloride and hydrogen sulfide. The following two basin fringe members of Late Permian were assigned to the Zechstein Member to construct isopach map in order to show the facies development of certain selected time intervals (Van Adrichem Boogaert & Burgers, 1983). The lower basin fringe layer was the Z3 Fringe Claystone Member (ZEZ3U) (figure 3.13 (f)). It was a series of red, brown claystone with silty and sandy interbedding. The layer was above Z3 carbonate and below Red Salt Clay Member (Zechstein 4 Member). The last sequence of the



Z3 Member is the Z3 Fringe Sandstone Member (Z3S), a series of white/light white, fine/very fine-grained sandstone deposited in playa/sabkha, fluvial channels of sand flats. However, the upper and lower boundaries of the sequence remained unknown (figure 3.13(g)).

### 3.6 Groundwater Chemistry and Potential Hydrogen Impact

The groundwater of the reservoir was also an important factor for underground storage since the injected hydrogen reacted with the free ions (cations and anions) in the brine water. As shown in Table 3.2, the groundwater can be separated into three types: (1) shallow semi-confined aquifers; (2) deep, buried aquifers; (3) deep oil and gas reservoir. (Griffioen et al., 2016). Meteoric water entered the Permian Rotliegend reservoir in the Netherlands during the Early Cretaceous. And the topography flow could reach the Triassic and Lower Cretaceous reservoir, which was above Zechstein evaporate (Griffioen et al., 2016). This could be evidence of overpressure of the Permian Rotliegend reservoir and the Zechstein Group. Furthermore, the Z3 carbonate sits above the Z3 anhydrite group. According to Griffioen et al. (2016), the Ca concentration was higher than SO<sub>4</sub> if the main source was from gypsum and anhydrite, unless the saline or hypersaline groundwater lied below halite brine. For the process (eq. (3.1)) to happen, the temperature for microbial reaction should be 80°C, and 100~160°C for thermochemical reaction. And in anaerobic oxidation, methane is associated with SO<sub>4</sub> reduction in hydrothermal systems.

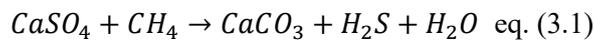


Table 3.2. Groundwater characteristics of groundwater composition of Netherlands (Griffioen, et al., 2016).

Compound	Shallow, semi-confined aquifers (65 samples)			Deep, buried aquifers (58)			Deep oil and gas reservoirs (59)		
	median	15-percentile	85-percentile	median	15-percentile	85-percentile	median	15-percentile	85-percentile
pH	7.7	6.9	8.5	7.5	7.0	8.4	6.4	5.5	7.2
Na	582	110	4718	3480	800	16,196	30,400	24,520	75,900
K	25	8.0	97	67.2	27.3	213	310	132	2088
Ca	46.5	12.1	242	106	23.7	1434	3958	2620	17,335
Mg	19.8	4.59	102	85.1	20.0	845	920	734	3405
Li				1.30			0.389		
Ba				0.37			24.5	0.21	42.7
Sr				131.5			410	26.5	630
Fe	0.71	0.08	11.7	3.53	0.62	14.9	35	16.6	419
Mn	0.21	trace	5.0	0.2			1.38		
NH <sub>4</sub>	1.16	0.29	2.38	11.9					
SiO <sub>2</sub>	15.35	9.35	50.1	18.5			102		
Cl	460	24.8	3198	5200	968	29,271	59,130	46,680	160,000
SO <sub>4</sub>	43.2	2.53	703	93.7	13.5	613	78.8	<1	507
Alkalinity	458	199	795	595	261	948	231	92.5	546
B				17.9			28.4		
F				0.5					
Br				41.7					
I				2.5					



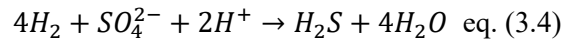
The research report: The Effect of Hydrogen Injection in Natural Gas Networks for the Dutch Underground Storage done by DBI GUT had well documented the impact of hydrogen on reservoir properties. In natural gas reservoir, it did not contain hydrogen. Hence, problems that did not exist could occur after hydrogen UGS operation. First of all, when injecting hydrogen mixture into subsurface, hydrogen would dissolve into reservoir liquids. The solubility of hydrogen increases in deeper and warmer reservoirs, but this is not an issue in Netherlands reservoirs (Pray, 1951). Furthermore, the molar solubility of hydrogen is higher than methane, leading to higher one-time loss (De Lucia et al., 2015). Hydrogen might also dissolve into oil, if there is oil left in the oil reservoir. And 1~3% of the injected hydrogen can mix with cushion gas (Srinivasan, 2006).

At the beginning of a UGS operation, partial pressure would increase, and higher partial pressure leads to an increased possibility of hydrogen leakage through diffusion, which is the only way for hydrogen to travel through caprocks. The diffusion of hydrogen depends on the concentration gradient, and the concentration of the gas component depends on the solubility of the gas in water. The solubility of hydrogen is lower than that of natural gas. However, the diffusion rate is four times higher (DBI GUT, 2017). Seals and caprock in the Netherlands are made up of salt or salt-clay layers. The Z3 carbonate member is sandwiched between the Grey Salt Clay member and the Z3 Anhydrite member. Hydrogen storage under the planned operational conditions is a novelty due to the specific properties of hydrogen, like molecular size and weight. The geological tightness of a porous formation caprock's ability is to withstand gas infiltration mechanically and hydraulically (DBI GUT, 2017). In dry porous media, the diffusion speed of hydrogen is 0.05 cm/min. However, in 100% water-saturated porous media, the diffusion rate decreases by a factor of  $10^8$  for clay, and salt clay layer is considered to be 100% water saturated in the Z3 group. The water saturation can prevent hydrogen from leaking for ~100,000 years. On the other hand, the salt layer had elastic-plastic properties, and the permeability of the salt formation was  $10^{-17} \sim 10^{-21} \text{m}^2$  (Liu et al., 2016). Hydrogen gas can enter salt matrix along the grain boundaries. The process is called percolation. Percolation can decrease the sealing integrity of salt rock formations.

Geochemical reactions are another aspect that might impact the reservoir and cap rock. The reactant of reactions of hydrogen with carbonates are sulphates, sulphides, and oxygen. However, geochemical reactions with minerals are slow and less relevant for gas storage (DBI GUT, 2017). Microbiological reactions are also important for reservoir and cap rocks, and the temperature of the carbonate reservoir at the Alkmaar field is around 80°C. There are two types of reaction, autochthonic and anthropogenic. Autochthonic reaction is when the reactants are buried in the reservoir millions of years ago when the sediments are deposited. Anthropogenic reaction is when the reactants are brought into the reservoir during drilling and operation.



The microbiological reaction included methanogenic, acid-forming, and sulphate-reducing reaction (DBI GUT, 2017):

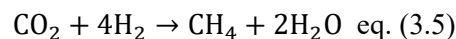


Common impacts caused by microbiological reaction included corrosion and acidification of the reservoir fluids through accumulation of hydrogen sulphide ( $H_2S$ ) and organic acids, decrease of permeability through iron sulphide (FeS) precipitation, biofilms and extra-cellular, reduction of gas quality through hydrogen consumption and hydrogen sulphide ( $H_2S$ ) formation, microbial induced corrosion, stimulation of microbial processes through additional hydrogen energy potential, precipitation respectively solving of matrix components in carbonates, Sedimentation of sulphur/biofilms in surface facilities through increased hydrogen sulphide share in the withdrawn gas.

The DBI GUT report tested 0.5% of hydrogen to the admixture to natural gas, and the maximum partial pressure raised to 2 bar in UGS Grijskerk, where partial pressure affected diffusion rate and embrittlement of steel grades. However, in this case, the partial pressure is very low, and the risk of hydrogen diffusing through caprock is minimal (Chen et al., 1977). 0.5% of hydrogen in the mixture is too low to lead to any measurable effect on the reservoir brine or changes in the transport mechanism in the reservoir. Furthermore, the risk for microbiological reaction is also relatively low. 0.5% of hydrogen mixture and free sulphur in the brine can generate a certain amount of  $H_2S$ , but the carbonate rocks buffer the reaction.

When increasing the hydrogen percentage to 10%, there is less volume that can be stored in UGS because hydrogen is less compressible than methane. The partial pressure is higher, which causes the one-time loss also to be higher. Higher hydrogen percentage increases the reaction potential for iron, sulphur and carbon dioxide ions:

Methanogenesis:



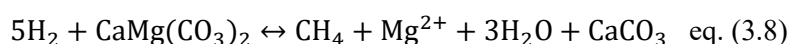
Sulphate Reduction:



Iron Reduction:



Calcification (only geochemical)



With 10% hydrogen in the gas mix, the potential for changes in the brine composition is high enough to consider for reactions with the reservoir rock (Paterson, 1982). Methanogenesis only causes loss in volume and energy, and it is not harmful. On the other hand, once leaked,



hydrogen sulphate is toxic to the environment and human society. Iron reduction and calcification can lead to precipitation, which leads to plugging of pores and loss of total permeability in the reservoir. However, the geochemical reaction is also buffered by carbonate reservoir rocks.

## 4. Methodology

As mentioned in the introduction, this research aims to quantitatively characterise the Z3 Zechstein reservoir interval in the Alkmaar field and to deduce potential geochemical reactions on such rocks upon hydrogen storage. This will help in learning about carbonate reservoirs at Alkmaar/Boekelermeer field for UHS application. It is crucially important to understand the diagenesis of the carbonate reservoir rocks. This research included three parts. The first part consists of a quantitative petrography analysis. In the second part, I will evaluate the available well data on the NLOG website by EasyTrace software. In the last part of the research, I will focus on the possible effects of hydrogen on the properties of the reservoirs. In this research, I evaluated and analyzed well data from two wells, Boekelermeer-01 and 04 (BKLM-01 to -04). The well data included stratigraphic logs and core samples from Alkmaar Field (figure 4.1). The well logs from NLOG data provided gamma-ray, resistivity, sonic data, and a stratigraphic log with basic rock lithology information.

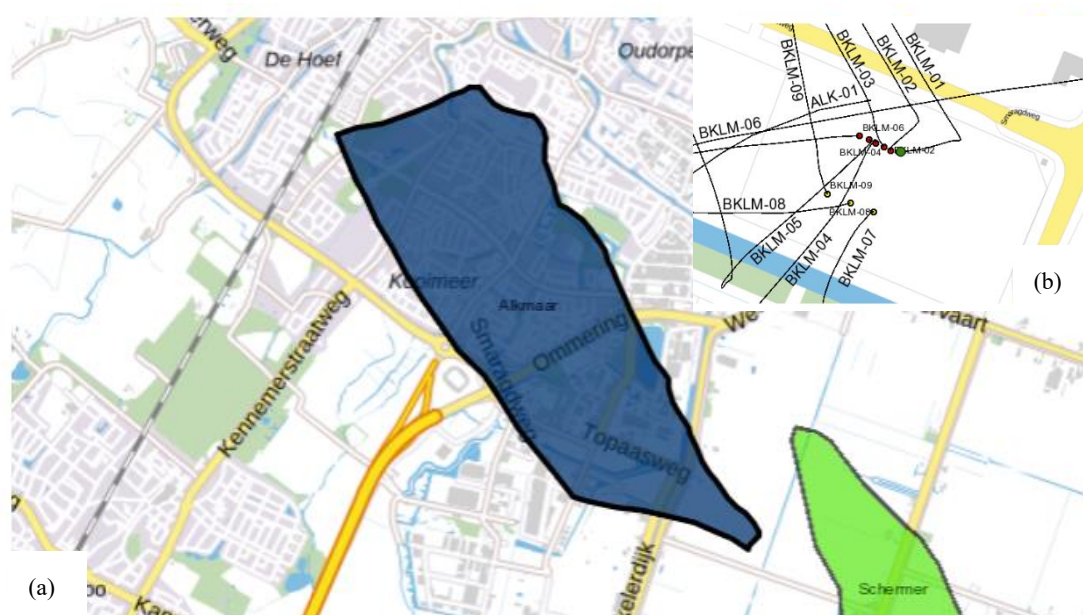


Figure 4.1. (a) The map of the depleted Alkmaar Gas Field; (b) The location of the wells (ALK-01, BKLM-01~09), the distance between BKLM-01 and -04 is 14m (NLOG, 1975).

### 4.1. Part 1: Quantitative Petrography

However, only BKLM-01 and -04 had the core samples stored at the TNO Core Repository at Zeist, Netherlands, and the sedimentary logs provided on the NLOG website were not documented in detail. Hence, before performing quantitative analysis, new sedimentary/stratigraphic logs of BKLM-01 and -04 were made with more detailed information, including porosity typology, cementation types, bioclasts (allochems), dolomite and anhydrite. After the production of the well logs, twenty-five rock samples from potential storage and caprocks were selected for preparing thin sections and subsequent quantitative petrography

analysis, ten from BKLM-01 and fifteen from BLKM-04. The selected thin section samples were based on the representativeness of a core sample sequence, with the most characters shown. After selecting the thin sections, the quantitative petrographic analysis was done by microscopic analysis of the thin sections (conventional and cathodoluminescence techniques) to identify the carbonate rock constituents, diagenetic phases, and porosity type. Furthermore, image analysis and point-counting will be performed on JMicroVision to quantify the analyzed features. JMicrovision was designed especially for the analysis of high-definition images of rock thin sections and had the function of describing, measuring, quantifying and classifying components of all kinds of images. JMicroVision v1.3.4 (<https://jmicrovision.github.io/>), like a microscope, allows a dynamic observation of a specimen with the possibility of combining various focus or lighting modes (polarized light, fluorescence, etc.). Moreover, the magnifying

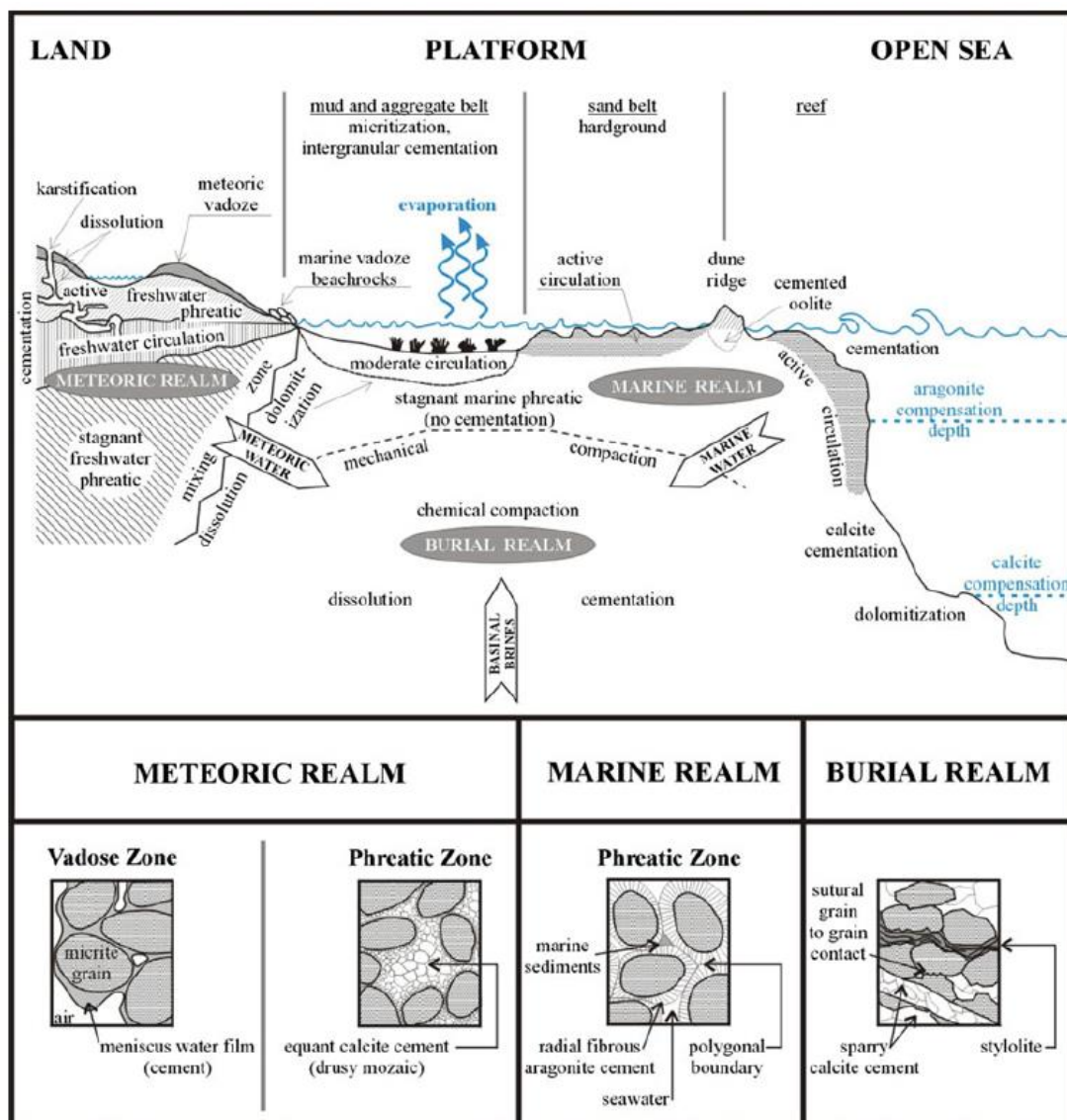


Figure 4.2. Schematic representation of major carbonate diagenetic realms, related processes and resulting products in a carbonate platform (Nader, 2017)

lens and the multi-view tool allow a simultaneous view of several images, each with its magnification, while maintaining a common position in the centre (JmicroVision, 2019). The purpose of the quantitative petrography is to understand the information in the core rocks and the thin section samples. By analyzing the thin sections with the diagenetic features, it is possible to recognize a certain depositional environment. The main carbonate realms can be separated into marine, meteoric, and burial realms (Nader, 2017) (figure 4.2). The marine realm can be further classified into a stagnant and active zone, where the stagnant zone represents the environment with minimal water circulation and minor cementation (micritization). On the other hand, the active zone, like its

name, is an active water circulation zone with massive cementation. The meteoric zone can also be separated into two zones. The first zone is the upper vadose environment, which includes a zone of carbonate dissolution by undersaturated meteoric water and a zone of precipitation where minor cementation happens. The second zone of the meteoric realm is the lower phreatic environment, which can be split into three subsections, dissolution zone, precipitation zone, and stagnant zone. The dissolution zone results in moldic and vuggy porosity; the

precipitation zone included porosity destruction, which might be caused by water circulation and rapid cementation; the stagnant zone included cementation within the pore space. The burial realm is a freshwater phreatic zone characterized by crystal replacement and chemical reaction, which might lead to the formation of drusy mosaic patterns, syntaxial overgrowth, and poikilotopic cement. The lithology of this realm is dependent on compaction and pressure solution. Furthermore, the porosity development and evolution give clues for the major diagenetic processes, their magnitude, and their extent. The porosity in carbonate rocks can be classified as fabric and not fabric (figure 4.3). Fabric porosity included primary and secondary porosity. Primary porosity is created during the deposition. It usually included inter- and intra-particle, fenestra, shelter, and growth framework. The secondary fabrics are moldic or intercrystalline porosity types, which occurred after deposition. On the other hand, the no fabric porosity types are all secondary porosity, including fractures, channels, vugs, and caverns. The

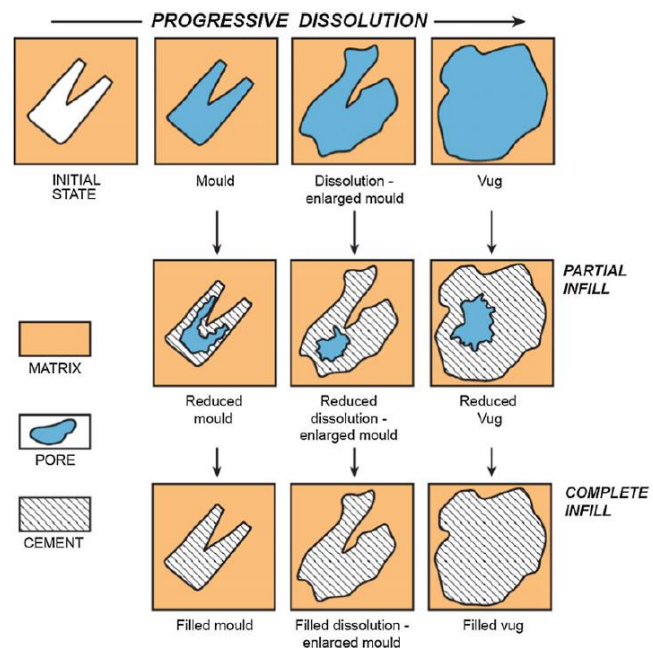


Figure 4.3. Schematic illustration of porosity evolution during diagenesis: progressive dissolution (from mould to vug) and porosity reduction by cementation (Nader, 2017).



depositional environment and possible geological events can be recognised with the diagenetic and porosity information from BKLM-01 and -04.

In addition, in this research, I used the cathodoluminescence microscopy at IFPEN (CL: Technosyn Cold Cathodoluminescence Model 8200 Mark II; operation conditions were 16-20 kV gun potential, 350-600  $\mu$ A beam current, 0.05 Torr vacuum and 5mm beam width) to analyze the thin section. The CL microscopy technique (figure 4.4) uses the luminescence emitted by minerals when they

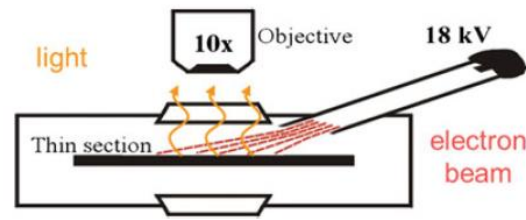


Figure 4.4. Cathodoluminescence (CL) microscopic technique. Electron beam focused on the polished surface of the sample. (Nader, 2017).

are excited with radiation caused by an electron beam (Nader, 2017). The technique is used to visualize growth textures and other internal structures that are not discernable with other analytical techniques. It can help reconstruct the process of mineral formation and alteration, provide information about the real structure of minerals, and prove the presence and type of lattice incorporation or several trace elements (Gotze, 2012). At the end of the quantitative analysis, it stained the thin sections with Alizarin Red S and Potassium Ferricyanide to test the content and the richness of iron in the carbonate reservoir rocks.

#### 4.2. Part 2: Well Data Analysis and Correlation

In the second part of the research, I combine the information mentioned above and available well logs using EasyTrace software (available at IFPEN). EasyTrace was developed for quick and high-grade digitizing of well logs and diverse cartographic materials and has the capability for both extractions from images and vector data correction. The various sedimentologic, diagenetic and porosity attributes were correlated across the available wells (cf. ten wells) by applying well log interpretation and the integration of core data. Multiple 2D well-correlation panels were produced, which gives a better understanding of the distribution of the reservoir characteristics across the Alkmaar field.

#### 4.3. Part 3: Hydrogen Impact on Reservoir

The permitted hydrogen content within the Dutch gas distribution system varies in respective parts of the country between 0.02% and 0.5% (DBI BUT, 2017). DBI proposed the study with hydrogen admixture with higher hydrogen concentration (10% and 100%). When the hydrogen concentration and the admixture are higher, the amount of dissolved hydrogen is higher. However, DBI did not consider the petrography and the rock stratigraphy. In the third part of the research, with the stratigraphy log, the quantitative petrography, and the well-correlation



panels of the Alkmaar field, it was possible to deduce a conceptual understanding of the effect of hydrogen admixture and brine to the carbonate reservoir rock alongside a literature review of associated geochemical reactions. This research reviewed the literature about the chemical and physical reactions of hydrogen with the properties found in the core rocks from observation of core samples and thin sections, which included dolomite, sulfide, chloride, anhydrite, salt, clay/shale clay, brine, and the limited amount of silicate minerals. As well as considered the effects of temperature and pressure. Then the literature review, mostly from the DBI GUT report from 2017, and the article by Heinemann et al. in 2021, was applied to the Z3 carbonate to predict the consequences of hydrogen injection, and I propose some measures to mitigate potential risks.

## 5. Result

### 5.1. Stratigraphy and Sedimentology

The depositional environment of carbonate rocks, in general, can be divided into four units (figure 5.1): Basin Unit, Subtidal Unit, Intertidal Unit, and Supratidal Unit. The Basin Unit is a thin layer at the bottom of the sequence. It indicates an initial transgression over pre-existing deposits, which usually happens in high-energy environments. The Subtidal Unit is usually an open marine or lagoon with low energy, where the depositions are finer-grained and more uniform. On the other hand, the Intertidal Unit happens within the range of tidal movement. The unit can be separated into two types of environments. The first environment is quiet, with a low energy situation, which usually refers to tidal flats. The second environment is agitated with a high-energy situation like a beach. The upper Supratidal Unit is the area covered by high energy, abnormal, windblown or storm tidal deposits. By analyzing the core samples, it is possible to understand the depositional environment of the Z3 Carbonate Unit .

As mentioned in the previous chapter, the research provided more detailed sedimentary logs from analyzing core samples from wells BKLM-01 and BKLM-04. Both well cores show shallowing upward sequences, which can be seen in both sedimentary logs and gamma ray data (figure 5.1 and 5.2). On the sedimentary logs, as the depositional environment moved to shallower depth, the grain size increases, and on the basis of the change in grain size, both BKLM-01 and -04 core samples can be separated into different sequences. On the other hand, when the gamma-ray value increases, the core sample consists of more clay/shale material. As it went to a shallower depth, the gamma-ray signal became weaker, which is a sign of shallowing upward sequence. Because the clay percentage decreases, the rocks became more grain-supported instead of matrix-supported. The cause of the shallowing upward sequence is that the rate of the carbonate sediment accumulation is higher than the rate of subsidence of the shelf or platform upon which the sediment is deposited. Hence, the sediment repeatedly accumulated and built up to sea level resulting in a sequence of deposition (James, 1997).

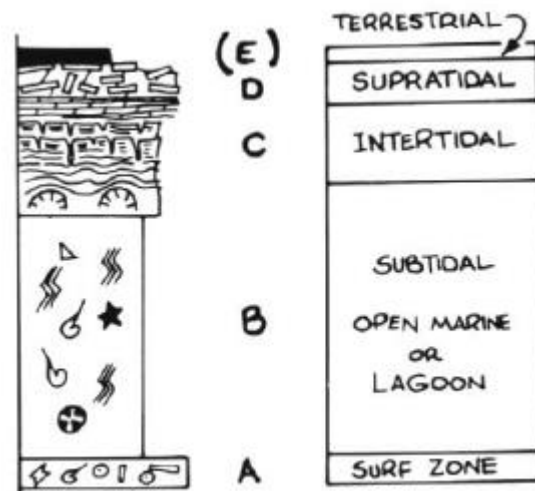


Figure 5.1. The classification of different units in shallowing upward model for carbonate. (A) Basin Unit (surf zone): lithoclast rich conglomerate or sand; (B) Subtidal Unit: fossiliferous carbonate; (C) Intertidal Unit: stromatolitic, mud-cracked cryptalgal limestone or dolomite; (D) well laminated dolomite or limestone; (E) Terrestrial Unit: shale or calcite, bracketed to emphasize that the unit is often missing (James, 1997).

### 5.1.1. BKLM-01

The BKLM-01 core samples are from 1969-2006 m depth in the Z3 carbonate group. The section can be divided into three sequences on the basis of the gamma-ray data provided by TNO and systematic analysis: 1996-2007 m (Sequence 1), 1978-1996 m (Sequence 2), and 1969-1978 m (Sequence 3). Figure 5.2 shows the gamma-ray and simplified sedimentary log, while figure 5.3 shows the detailed stratigraphic log.

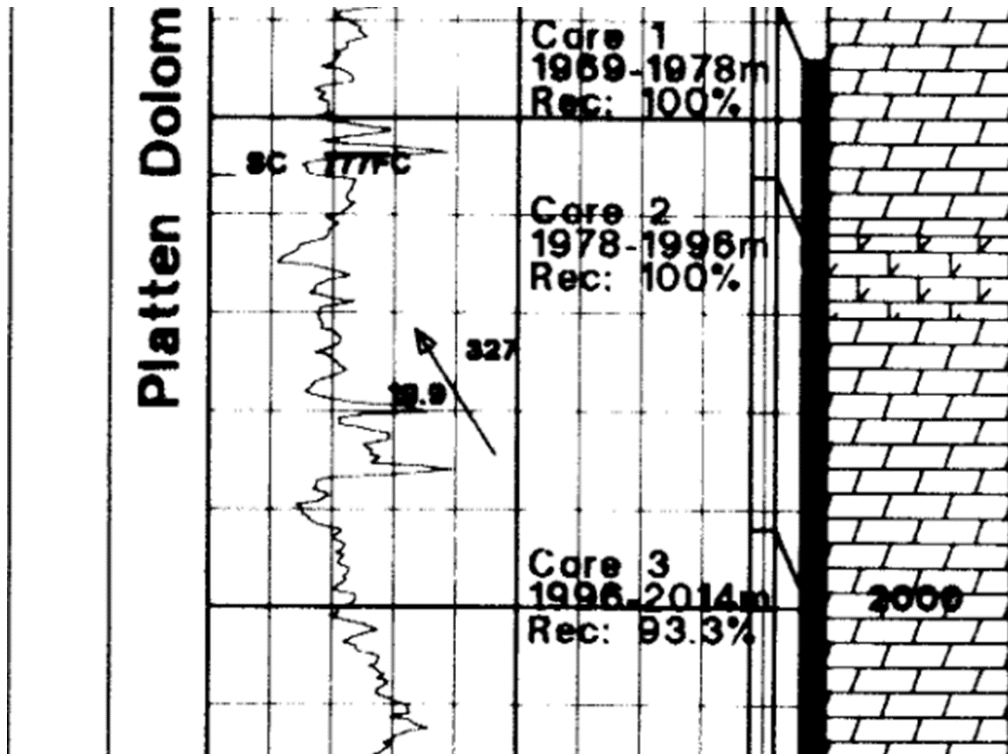


Figure 5.2. Three sequences of BKLM-01 by Gamma ray data: (1) 1996-2007 m; (2) 1978-1996 m; (3) 1969-1978 m.

The first sequence of BKLM-01 is at the depth of 1996-2006 m, and the whole sequence showed strong lamination (figure 5.4). At the bottom, the rock is generally fine-grained, which can be classified as wackestone. Between 1996m and 1998 m, the rock became more fine-medium-grained floatstone. The gamma-ray signal is higher at the bottom and decreased gradually up to depths ~1996 m, which fits with the shallowing upward observation from the core samples. At the first sequence, small anhydrite/gypsum clasts (1-2 mm) can be found all over the core samples. Some of the crystals are removed or dissolved by brine water, which forms small vugs (1-2 mm). Toward shallower depth, there are more and more pore spaces and frequently filled with salt (figure 5.4(c), (d)). Bed parallel stylolite can also be found all over the place and is often filled with organic matters.



Figure 5.3. Sedimentary log of BKLM-01 and rock samples with potential storage ((b), (c)) and seal ((a), (d)).



Figure 5.4. BKLm-01 sequence 1 core samples. (a) 2005 m depth; very fine grained; limited porosity; bed parallel stylolite filled with organic matters. (b) 2002.5 m depth; very fine grained; increase in porosity comparing to (a); bed parallel stylolite filled with organic matters; large anhydrite formation. (c) 1999.8 m depth; fine grained, the grains are easier to spot than previous two; more pore holes, but they are filled with anhydrite/gypsum clasts; bed parallel stylolite. (d) 1998.2 m depth; fine grained; visible pore spaces and few vuggy structures; bed parallel stylolite; several 1 cm thick anhydrite inclusion layers.



The second sequence of the BKLM-01 ranged from 1978-1996 m depth. The bottom part of the sequence is a transition between the first and the second sequence. It has similar lithology but with finer grain size. At about 1991-1993 m depth, broken shelly fossils started to appear (figure 5.5(a)). However, from 1986-1990 m, the grain size turned from fine/mid-grained to very fine/fine-grained, and the gamma-ray signal increased even higher than the bottom of sequence 1 (figure 6.2). From 1980-1986 m, the grain size gradually turned from mid-grained (floatstone) to coarse-grained (packstone), and the rocks became very porous, containing a massive amount of broken shelly fossils (crinoids, unidentified bioclasts), ooids, and lithoclasts (figure 6.5 (b) and (c)). However, many of the pore spaces are filled with anhydrite/gypsum cementation. The anhydrite/gypsum clasts also often appeared as needle-shaped all over the rock samples. Furthermore, at 1980-1982 m, 5 cm thick floatstone layers are interbedded with the packstones. Lamination can also be spotted at 1980-1986 m depth. The lamination started up weak. However, it got stronger as it went upward to the shallower depth. From 1978-1980 m, the grain size dropped to fine-grained and became less porous (figure 5.5 (d)), but the gamma-ray signal is low, which means it is low in clay minerals. This could be a transition phase between the second and third sequences.

The core observation of the sequence 3 (1969-1978 m) showed different results from the gamma-ray data (figure 5.6). At the bottom of the sequence, the lithology and grain size remained similar to the top of the sequence 2. However, it is a lot more porous, containing more bioclasts, and the colour of the rock turned from grey to light grey, yellowish colour. Above 1973 m, the observed facies became fine to very fine-grained, without any significant feature. The rock appeared more like shale clay.



Figure 5.5. BKLm-01 sequence 2 core samples. (a) 1992.2 m depth; fine-mid grained; more porous than the rock samples from sequence 1; bed parallel stylolite; porous layers and non-porous layers interbedding; weak lamination. (b) 1984.5 m depth; mid grained; very porous, some pore spaces are cemented by anhydrite/gypsum; broken shelly fossils and ooids can be spotted; multi-scale grain supported; weak lamination. (c) 1981.8 m depth; coarse grained; very porous; shelly fossils and ooids can be spotted; grain supported; weak lamination. (d) 1978.8 m depth; fine/fine-mid grained; bed parallel stylolite filled with organic matters; lack of pore spaces; no bioclasts; strong lamination.

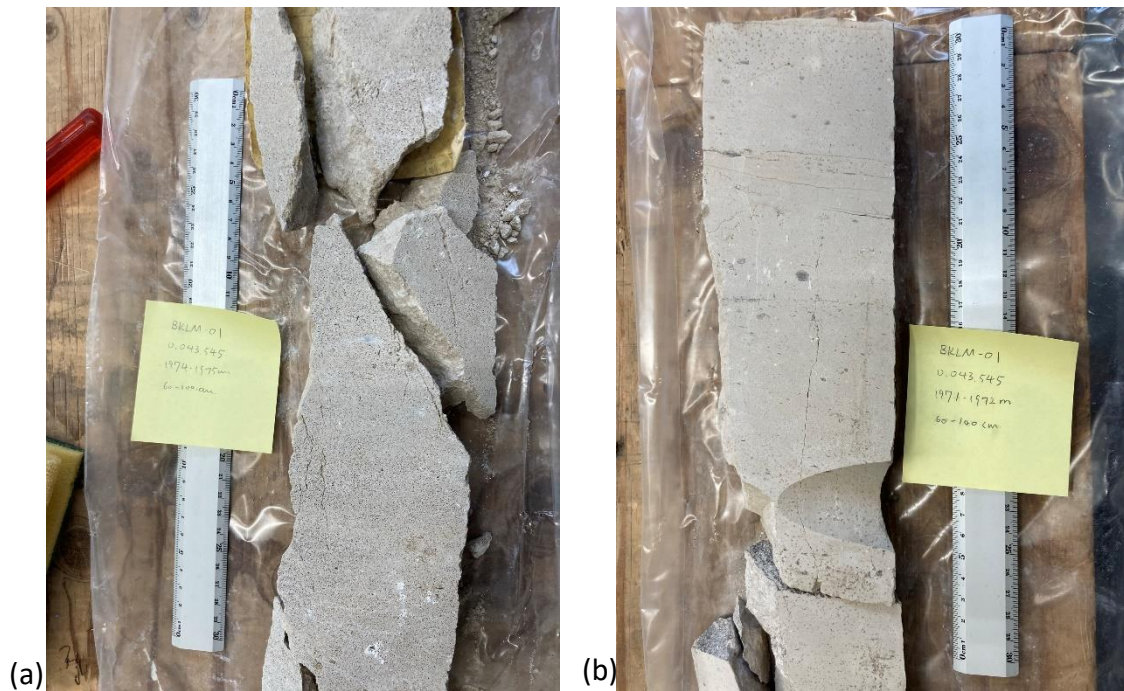


Figure 5.6. BKLM-01 sequence 3 core samples. (a) 1974.5 m depth; fine-mid grained; more porous than the rock samples from the top of sequence 2; anhydrite cement and needle-shaped anhydrite clasts; weak lamination. (b) 1971.2 m depth; fine grained; lack in pore sparsity; bed parallel stylolite; more likely to be clay/shale clay material; weak lamination.

#### 5.1.2. BKLM-04

The Z3 carbonate core samples from the BKLM-04 well are from 1945 to 2007 m depth. The samples can be separated into four sequences by gamma-ray data and systematical analysis. The core samples can be separated into four sequences: 1975-2007 m (Sequence 1), 1957-1975 m (Sequence 2); 1950-1957 m (Sequence 3), and 1945-1950 m (Sequence 4). Figure 5.7 shows the gamma-ray date, and figure 5.8 shows the detailed stratigraphic log. But the core samples from sequence 1 showed it is a perfect example of shallowing upward sequence.

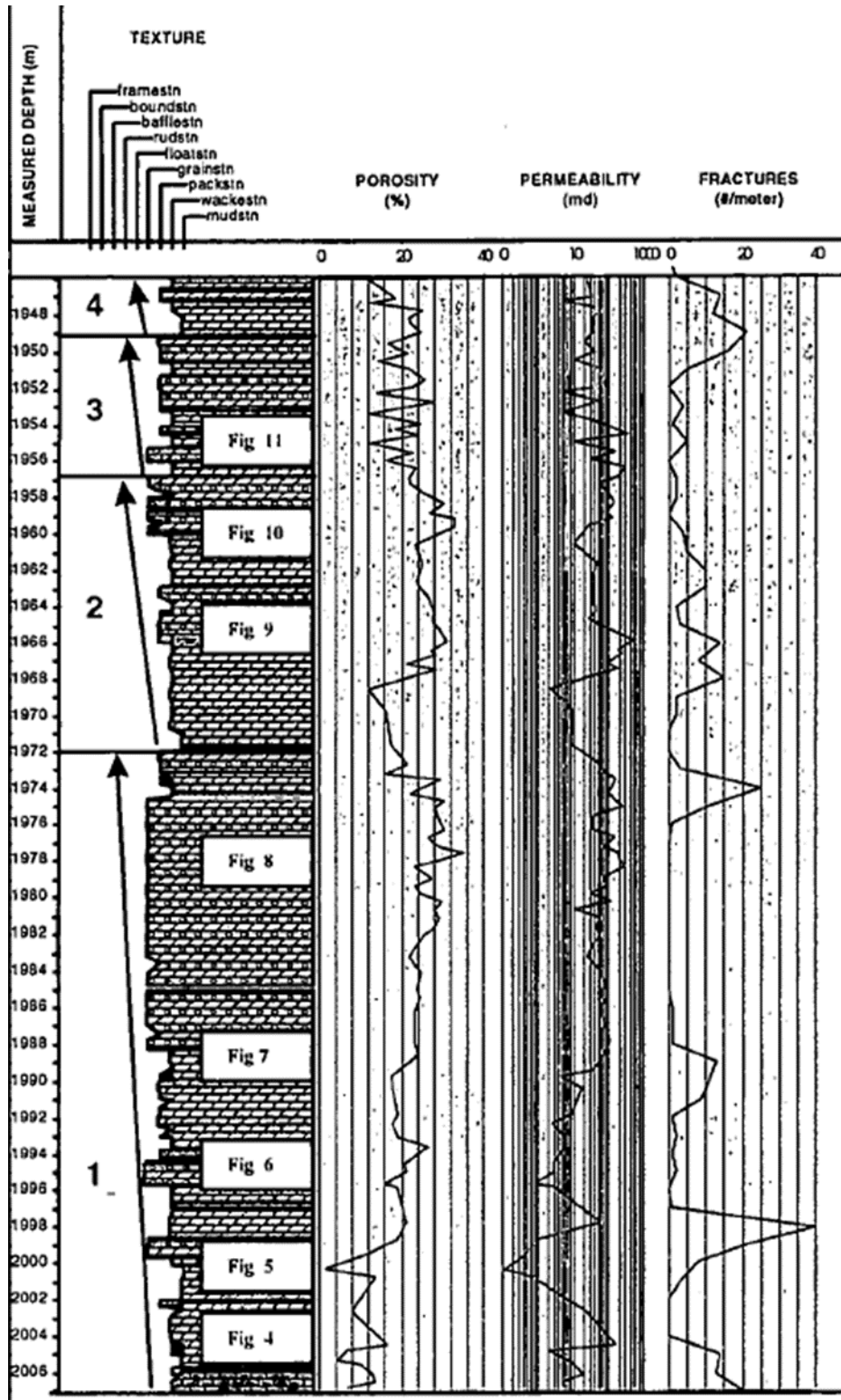


Figure 5.7. Four sequences of BKL4 by Gamma ray data: (1) 1975-2007 m; (2) 1957-1975 m; (3) 1950-1957 m; (4) 1945-1950 m. (Acomco Netherlands B.V., 1996)

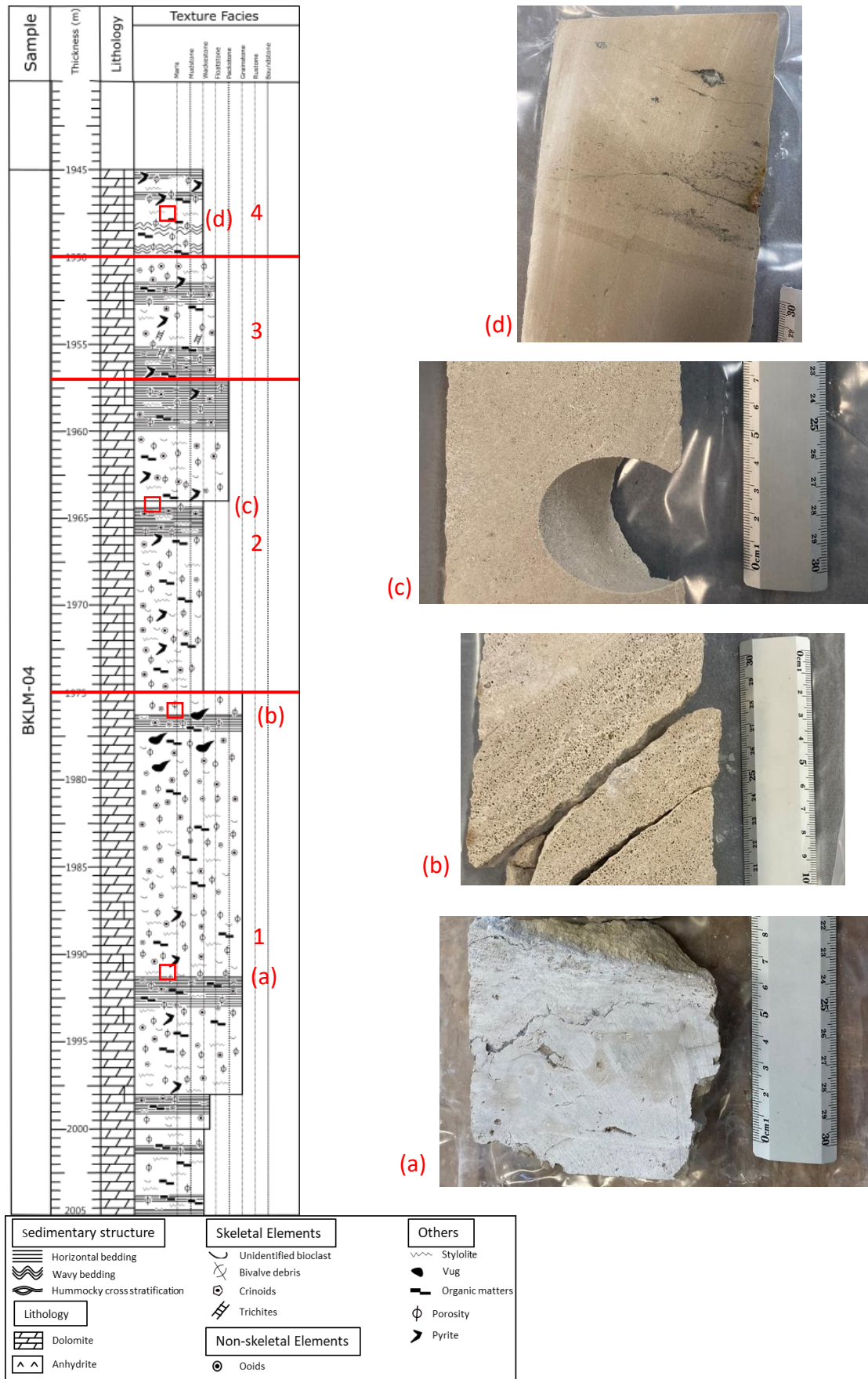


Figure 5.8. Sedimentary log of BKLM-04 and rock samples with potential storage ((b), (c)) and seal ((a), (d)).



At the very lower part of the sequence 1 (2000-2007 m), the rock samples are very fine-grained, low in porosity, and the stylolite is often filled with organic matters. However, the rock samples also showed sedimentary structures of wavy bedding and lenticular bedding (figure 5.9(a)), which indicated that the original carbonate rocks were deposited in the high-energy intertidal environment. At 1998.5 m depth, there is a clear boundary between wackestone and grainstone (figure 5.9(b)). After the boundary, the rock samples became increasingly porous, gradually moving upward to a shallower depth. The colour of the observed facies also turned from pale grey to yellowish colour (figure 5.9(d)) as it moved upward. Anhydrite cementation and needle-shaped anhydrite clasts are often seen in the pore space. Furthermore, broken shelly fossils are often seen, including crinoids, bivalves, and unidentified bioclasts, so as ooids. However, there is a 2-3 m thick layer of clay-rich material in the grainstone sequence (figure 5.9(c)), which can be seen in the gamma-ray data.

The second sequence (1957-1975 m) of BKLM-04 started with fine-grained clay-rich wackestone interbedded with grainstone (figure 5.10(a)). The wackestone is low in porosity, and the pore holes are not well connected. It also contained gypsum and needle-shaped anhydrite. The grainstone is similar to the ones at the top of sequence 1. As it went to shallower depth in the core sample, the wackestone became more consistent and contained more prominent anhydrite veins and clasts (figure 5.10(b)). After 1965 m, the rock samples turned into packstone/grainstone (figure 5.10(c)). The samples are not as porous as the grainstone in sequence 1, but the sample contained more stylolite, which is often filled with organic matters. The grainstones in the sequence 2 also had more anhydrite/gypsum clasts compared to sequence 1, and the size of sulphate minerals increased as it reached shallower depth.

Sequence 3 (1950-1957 m) is a sequence with mostly wackestone/floatstone. At the bottom of the sequence, the samples are more fine-grained. Moving toward the top, the samples became more mid/coarse-grained. The entire sequence did not contain grainstone, but the porosity is relatively high (25-30%) compared to the wackestone/floatstone in previous sequences. The pore spaces are often filled with anhydrite cementation. The sequence contained small anhydrite/gypsum clasts and needle-shaped anhydrite, and like other sequences, as it went shallower depth, the samples usually included larger anhydrite/gypsum crystals (1-3 cm). The 4th sequence (1945-1950 m) is a sequence of fine-grained wackestone, also without grainstones. The sequence has more bed parallel stylolite filled with organic matters. Furthermore, like the sequence 3, sequence 4 had a similar distribution of anhydrite/gypsum crystals, but the size of the crystal is smaller (0.5-1 cm).



Figure 5.9. BKLm-04 sequence 1 samples. (a) 2006 m depth; fine grained; low porosity; wavy bedding/lenticular bedding. (b) 1998 m depth; boundary between wackestone (lower) and grainstone (upper); shelly fossils. (c) 1989 m depth; fine grained; clay/ shale clay material; 2-3 m thick clay-rich layer in the shallowing upwards sequence, which can be seen in the gamma ray data (figure 6.8); (d) 1976 m depth; grainstone; pore spaces are not filled with cementation; potential storage section.





Figure 5.11. BKLM-04 sequence 3 and 4 samples. (a) Sequence 3; 1953 m depth; floatstone; larger gypsum crystal (1-3 cm) and 1-3 mm thick anhydrite/gypsum veins. (b) sequence 4; 1947 m depth; wackestone; smaller gypsum crystals (0.5-1 cm); no significant sedimentary or structural features.

## 5.2. Quantitative Petrography

As mentioned in the methodology, twenty-five rock samples (ten from BKLM-01, fifteen from BKLM-04) are selected based on the representativeness of the samples to each sequence of the well cores (presented above). The samples are first quantitatively analyzed with polarized microscopy. Then the samples are examined under cathodoluminescence (CL) microscopy to reconstruct the processes of mineral formation and alteration to provide information of the real structure of the minerals and several trace minerals (Gotze, 2012). The thin sections are also stained with Alizarin Red S and potassium ferricyanide. Alizarin Red S will make calcite appear red, and it will be colourless if it is dolomite. Potassium ferricyanide will make the minerals appear blue if the minerals are iron-rich.



### 5.2.1. BKLM-01

#### 5.2.1.1. BKLM-01-1, Sequence 1, 2003.9m

The dolomiticrite is fine-grained, and the largest crystal is less than 25  $\mu\text{m}$ . The dolomite is matrix replacive and unimodal. The crystals are curved, irregular, and anhedral. The porosity type of the sample is intercrystalline, 10% (figure 5.12). The other type of observed porosity is related to fracture at only 1% (figure 5.13). However, the intercrystalline porosity is often filled with an opaque material (figure 5.13), which might be organic matters. Some of the opaque materials are semi-transparent. It might be oil that is trapped inside the pore space.

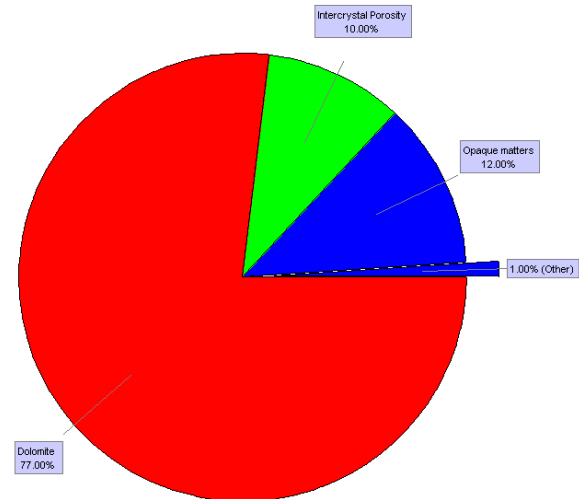


Figure 5.12. Quantification of BKLM-01-1.

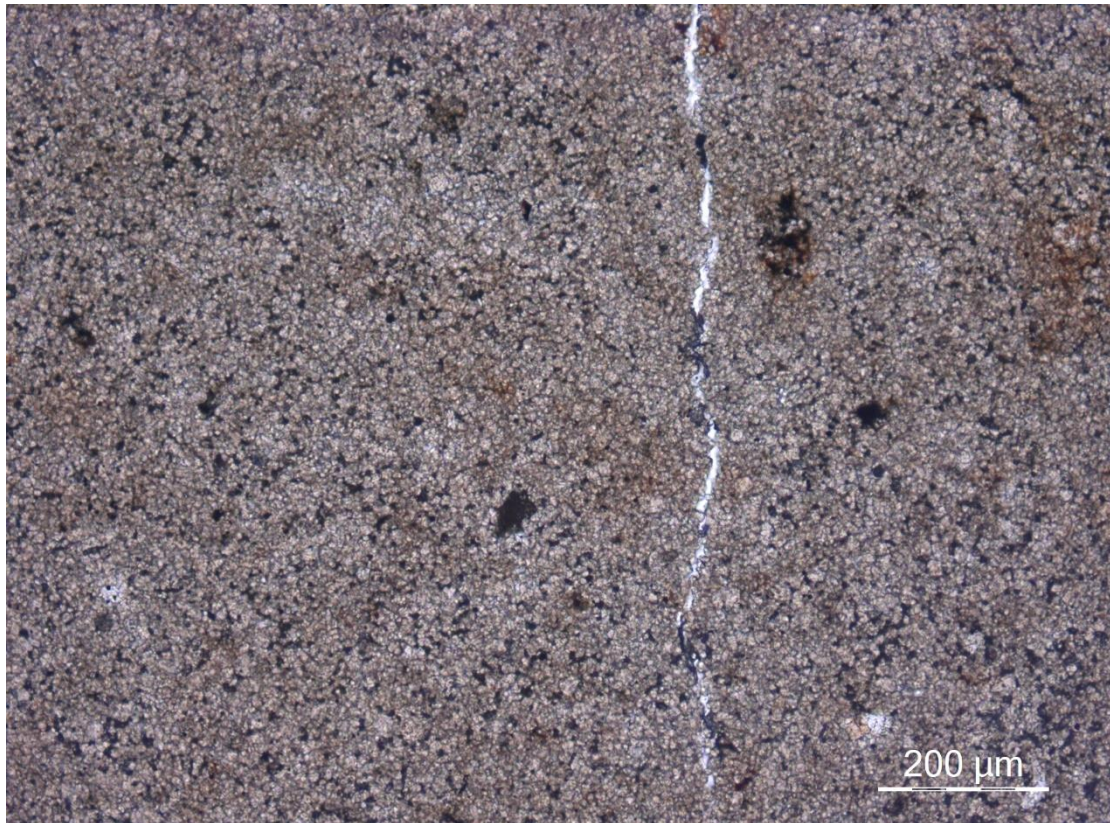


Figure 5.13. BKLM-01-1 under plane polarized light. A clear fracture can be seen in the photo. Significant amount of the pore spaces is filled with organic matters. Some of the opaque minerals showed reddish brown color, which might be oxide minerals.

## 5.2.1.2. BKLM-01-2, Sequence 1, 1995.5m

The second sample is dolomiticrite, with slightly coarser-grained (~40 $\mu$ m). The rock is matrix replacive, non-planar, and unimodal. The porosity types included intercrystal, fracture, and vugs. However, most of the pore spaces are intercrystal (9%). The pore spaces are often filled with opaque materials, which might be organic matters.

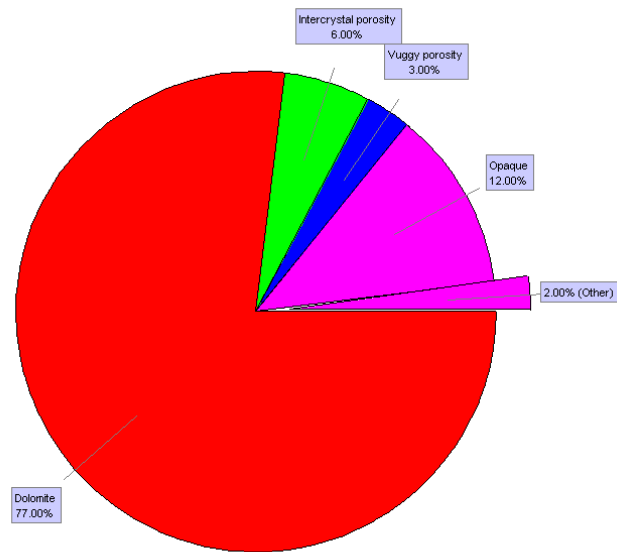


Figure 5.14. Quantification of BKLM-01-2.

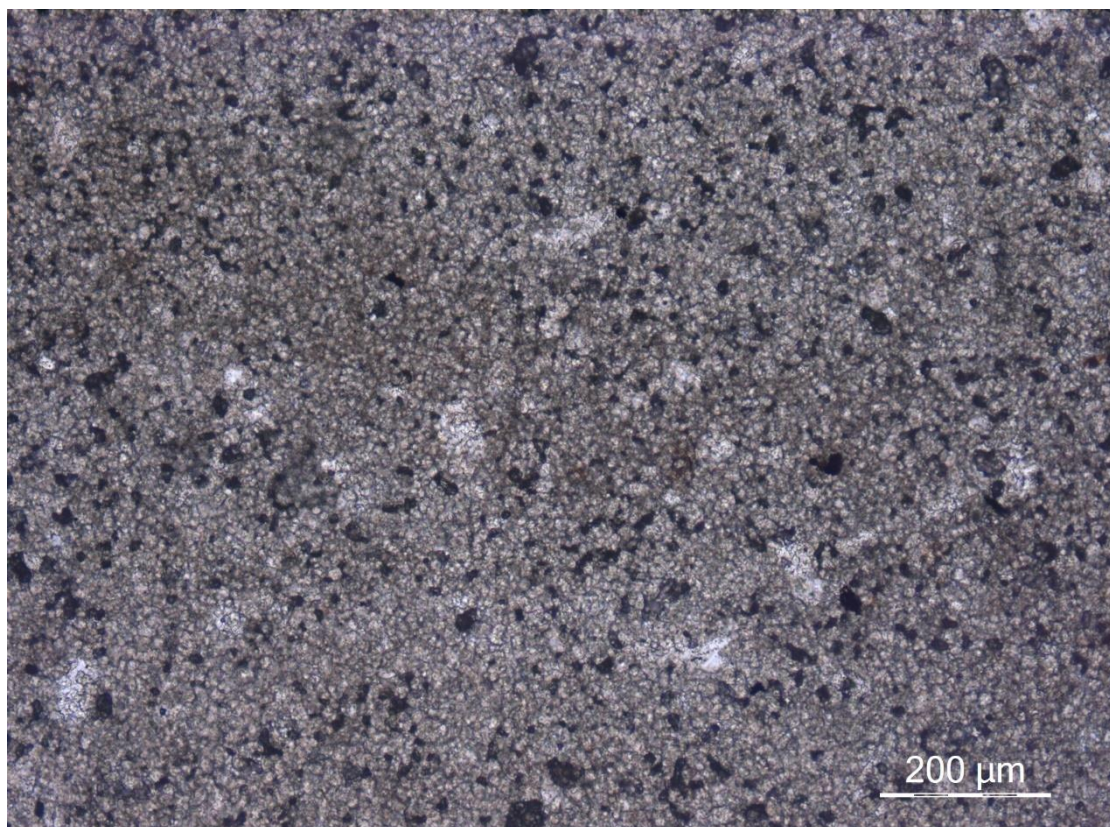


Figure 5.15. BKLM-01-2 under plane polarized light. Very similar to BKLM-01-1, but the grain size is larger, and the porosity is lower.

### 5.2.1.3 BKLM-01-3, Sequence 1, 1993.5m

The sample is also 100% dolomiticrite. Most of the intercrystal porosity is filled with opaque organic materials. The dolomite crystals in the sample are planar, irregular, varied in size, and very compacted with lower porosity. The fine-grained dolomite is around 20  $\mu\text{m}$  (46%), and the coarse-grained crystals are around 60  $\mu\text{m}$  (30%). Furthermore, a limited amount of small cubic pyrite minerals is present, which can be better seen under CL microscopy.

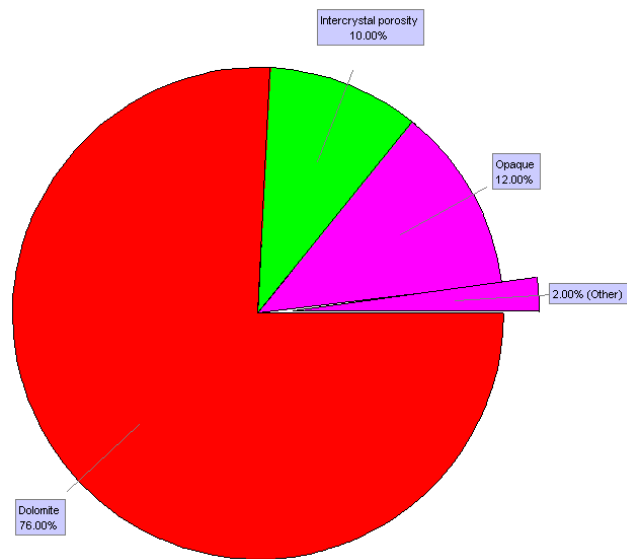


Figure 5.16. Quantification of BKLM-01-3.

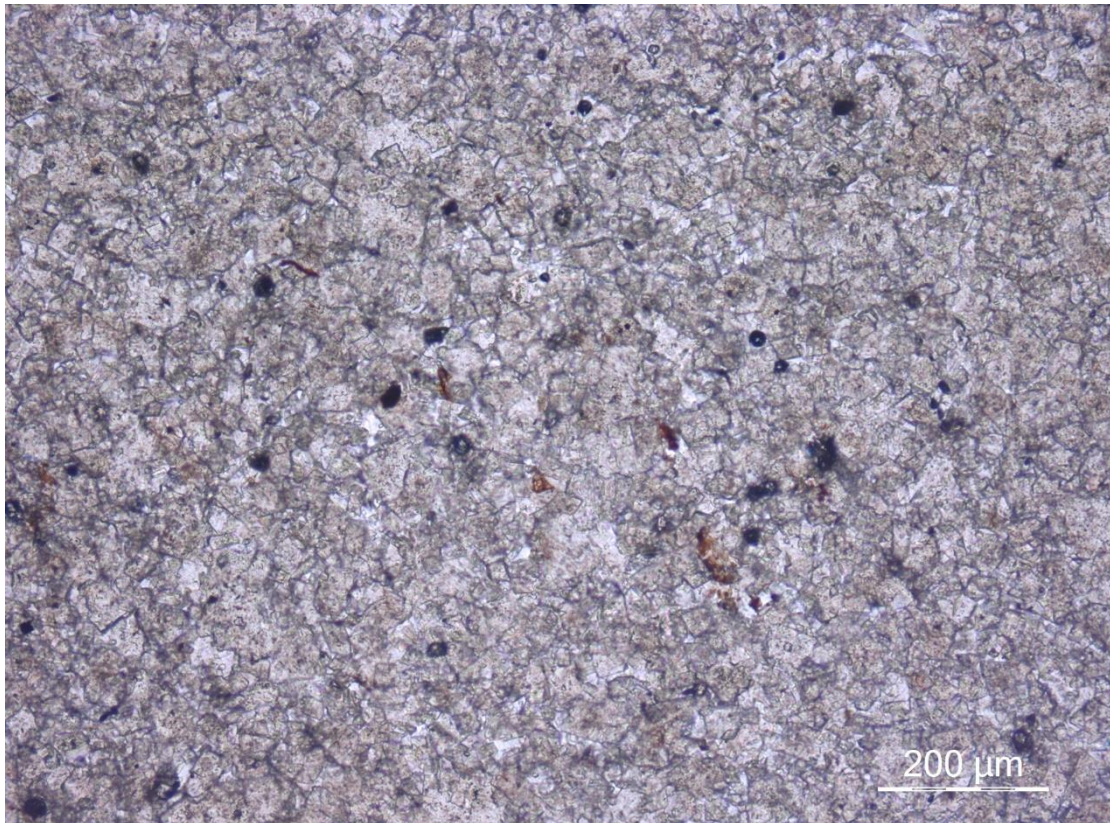


Figure 5.17. BKLM-01-3 under plane polarized light. Coarse grained dolomiticrite. Less pore space is filled with

#### 5.2.1.4 BKLM-01-4, Sequence 1, 1991.2m

The 4<sup>th</sup> is coarse-grained dolomiticrite. As mentioned previously, more anhydrite/gypsum crystals are at the top of sequence 1. There is a ~4cm long, 0.2~0.3cm wide gypsum veins in the thin section, as shown in figure 5.20. The sulphate salt had second-order interference colour, with one clear cleavage and lower relief. Hence, it is clear that the salt would possibly be gypsum instead of anhydrite since the two minerals often coexisted. The dolomite in this

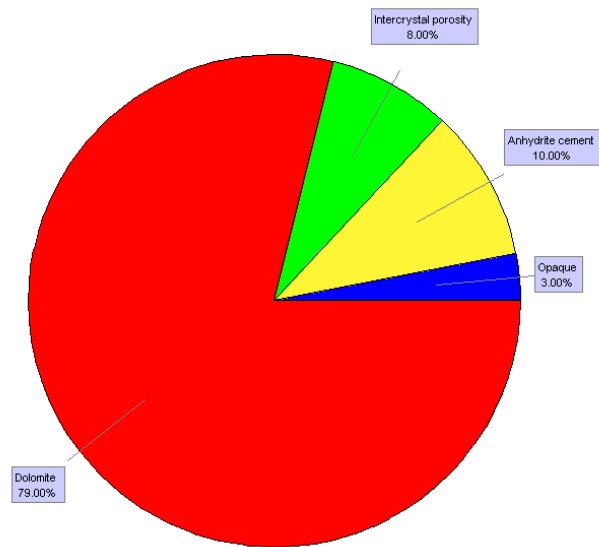


Figure 5.18. Quantification of BKLM-01-4.

sample is unimodal, matrix replacive with irregular crystalline. And the crystals are very compacted, lacking intercrystal porosity (figure 5.18). Furthermore, the pore spaces are often filled with opaque organic materials (figure 5.20). Fracture porosity is also seen in the thin section, but not common.

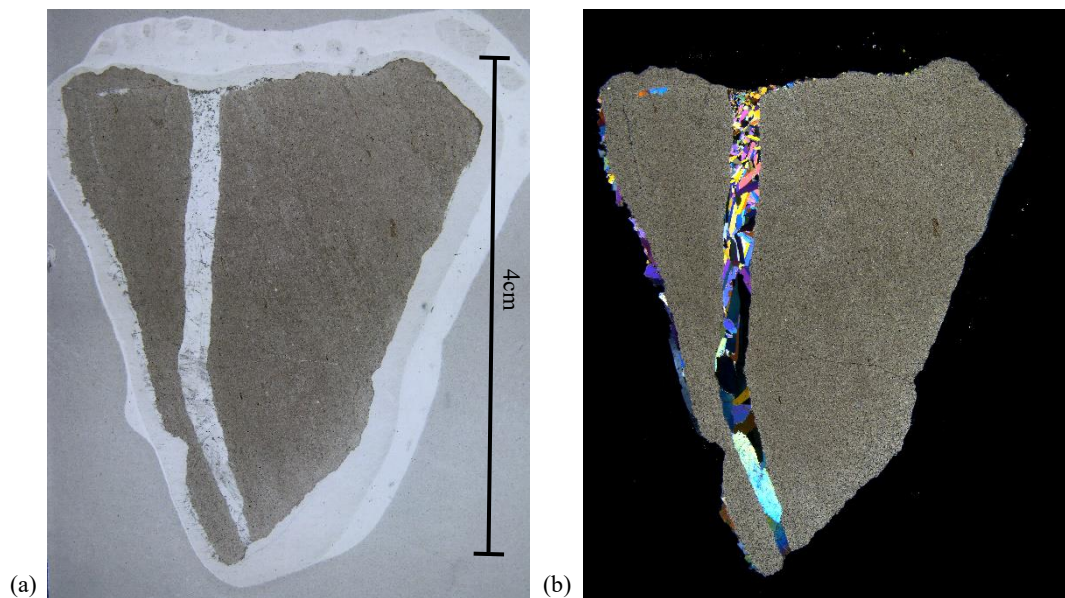


Figure 5.19. BKLM-01-4 thin section scan with gypsum vein. (a) PPL; (b) XPL.

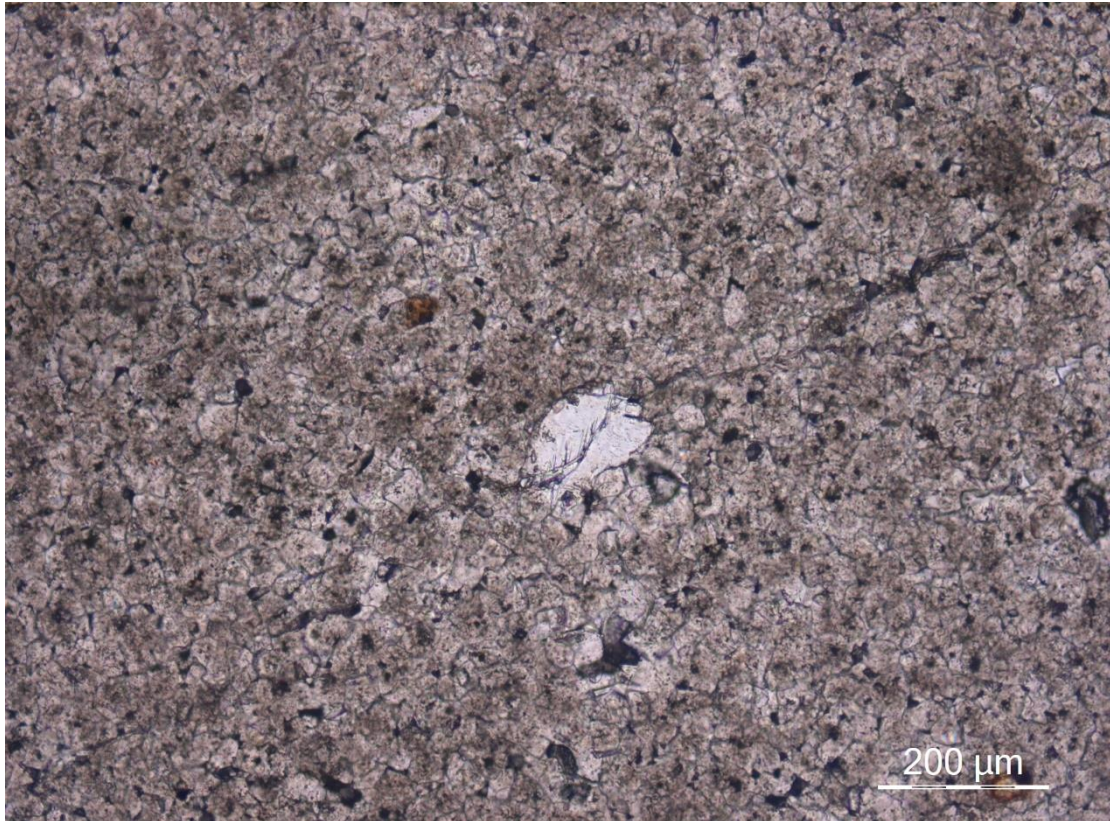


Figure 5.20. BKLM-01-4 under plane polarized light. Coarse dolomiticrite (~60µm); compacted crystals with limited pore spaces, and the pore spaces are often filled with organic matters.

#### 5.2.1.5 BKLM-01-5, Sequence 2, 1986.2m

The observed rock sample is packstone with fine-grained dolomite cementation (figure 5.22). The rock is an oosparite before dolomitization. The dolomite crystals are planar, replacive dolomite, mimic texture (dolomitized ooids), and vary in size. The crystals of the mimic grains are 20-40µm, and the dolomite cement range from 40 to 100µm. There is also a second phase of recrystallization, where the larger dolomite cementation formed in the mimic grain after dissolution of the original grain (figure 5.23). The

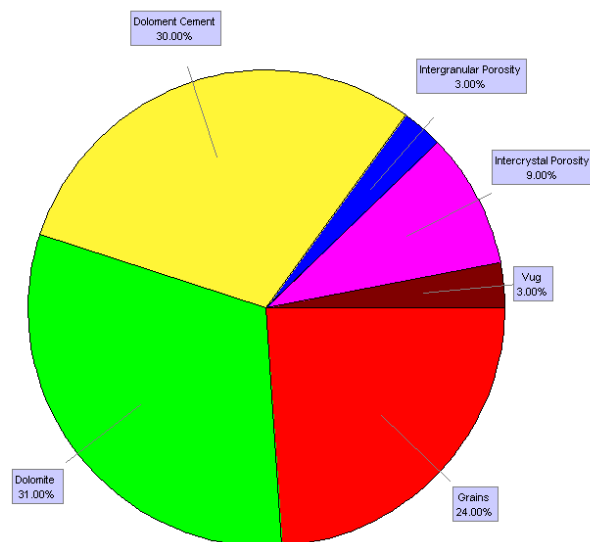


Figure 5.21. Quantification of BKLM-01-5.

The dolomite cement in the sample is usually dog tooth, bladed, and meniscus. However, most of the fabric is equant mosaic. The most common seen porosity types in BKLM-01-5 are intergranular (3%), intercrystal (9%), and vug (3%) (figure 6.20). Furthermore, the intercrystal pore spaces are often filled with opaque organic materials.

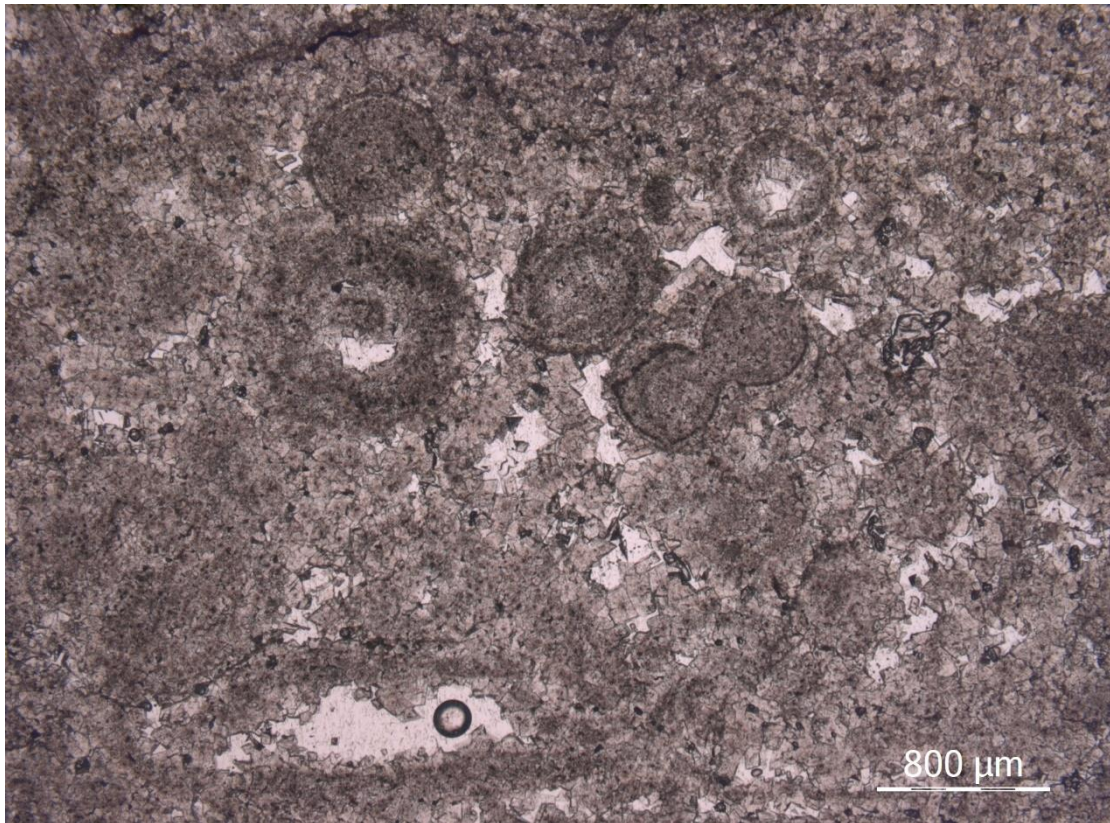


Figure 5.22. BKLM-01-5 under plane polarized light. Packstone with fine grained dolomite cement. Large pore space like vugs and intergranular porosity can be seen.



Figure 5.23. BKLM-01-5 under plane polarized light. Equant mosaic cement and second phase cementation in the mimic grain.

### 5.2.1.6 BKLM-01-6, Sequence 2, 1981.8m

The sample is grainstone with mid-grained dolomite cementation (80~100 $\mu$ m). The dolomite crystals are planar, polymodal, and matrix replacive. The mimic texture grains are large (1~2 $\mu$ m). Interclasts can be seen in the thin section (figure 5.25), and partial dolomitization can also be found between the interclasts. However, the mimic texture dolomites are fine-grained (20~40 $\mu$ m). Furthermore, the sample is more porous than previous samples. The porosity types included intergranular, intraparticle, intercrystal, moldic, and vug (figure 5.24).

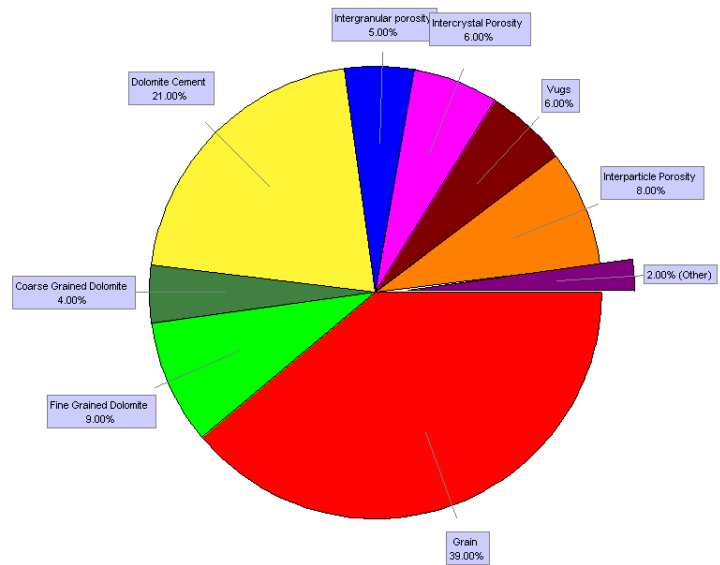


Figure 5.24. Quantification of BKLM-01-6.

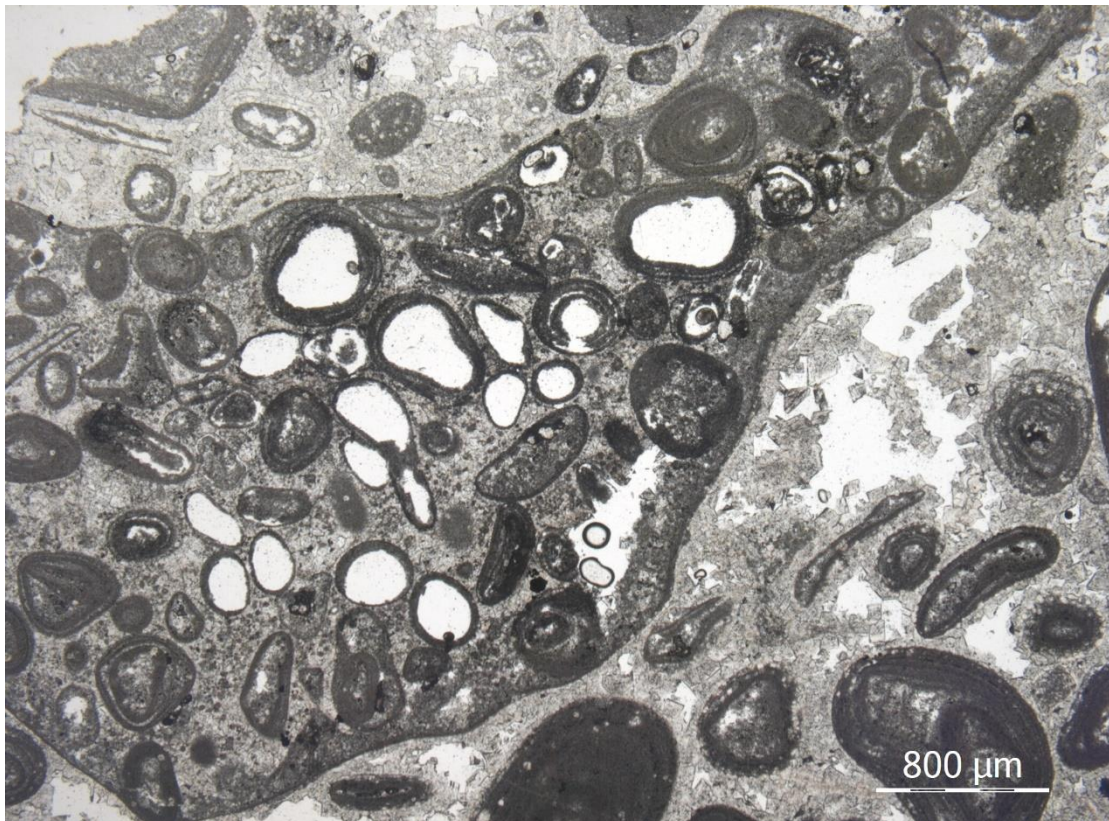


Figure 5.25. BKLM-01-6 under plane polarized light. Large interclast with moldic, and vuggy porosity. The grains in the interclast and the larger grains outside showed different stage of dissolution.

## 5.2.1.7 BKLM-01-7, Sequence 2, 1978.7m

The sample is a coarse-grained dolomiticrite (~100 $\mu$ m). The sample is matrix replacive, unimodal, planar, and the crystals are very compacted (figure 5.27(b)). The sample is low in porosity. The porosity types are intercrystal and vuggy (figure 5.26). And the intercrystal pore spaces are often filled with opaque organic matters. Furthermore, there is a 1x1cm cubic space on the thin section (figure 5.27(a)), possibly caused by the preparation of the thin section because the crystals at the edge of the space show a sharp cut. The space is unlikely to be recrystallised by larger minerals that cut through the dolomite matrix.

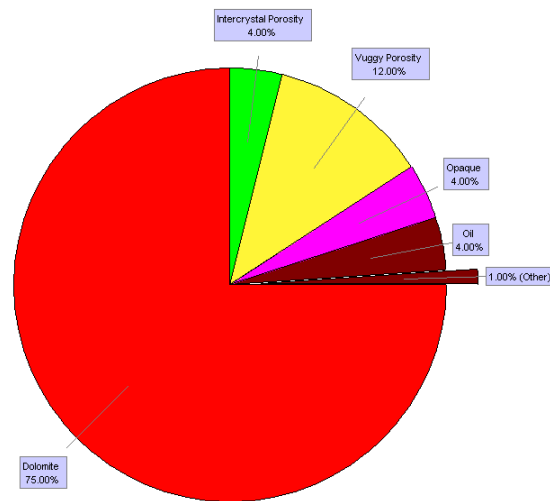


Figure 5.26. Quantification of BKLM-01-7.

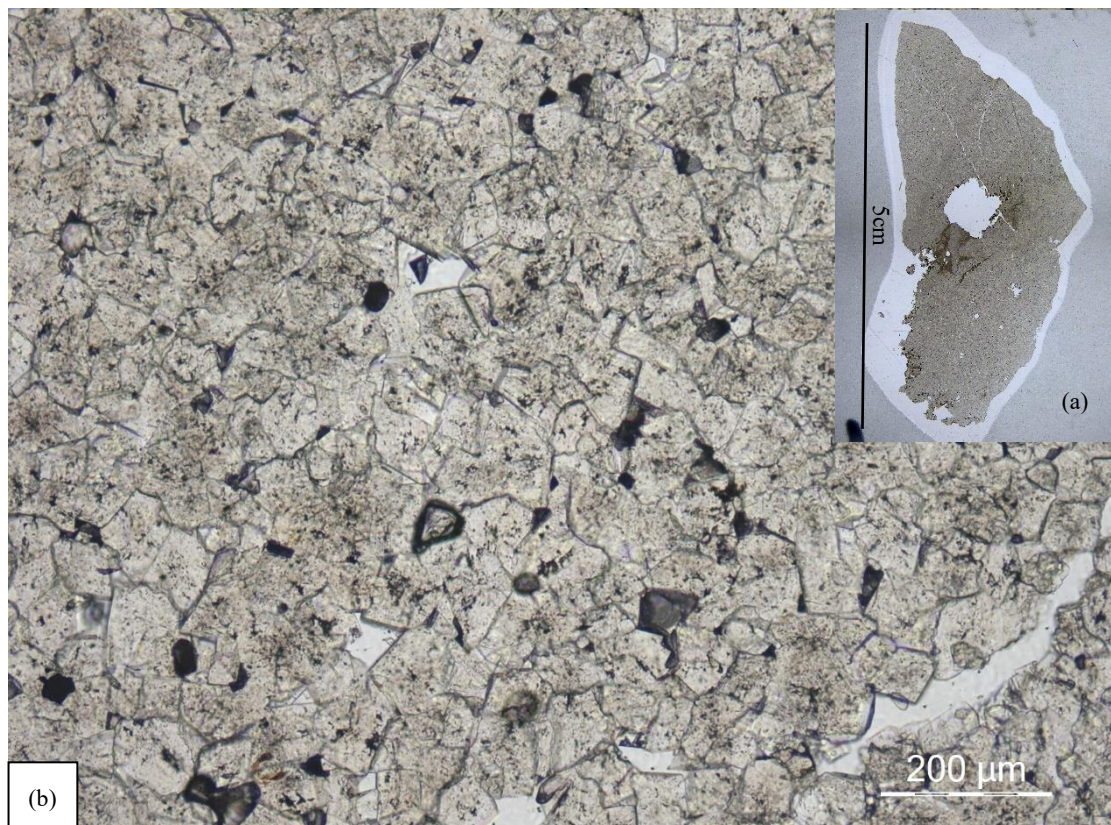


Figure 5.27. (a) The thin section of BKLM-01-7 with cubic space in the middle. (b) BKLM-01-7 under plane polarized light. Coarse grained dolomiticrite with compacted crystalline and lacking porosity.

### 5.2.1.8 BKLM-01-8, Sequence 3, 1975.2m

The sample is originally oosparite. The dolomite crystals are matrix replacive, planar, and polymodal, with fine-grained mimic textured grains (20-40 $\mu$ m) and coarse-grained dolomite cement (80-100 $\mu$ m). The dolomite cement is often drusy mosaic or granular mosaic (figure 5.29). The porosity types of the sample included intergranular, intraparticle, intercrystal, moldic and vugs. The most abundant types are vugs (figure 5.28). And the intercrystal porosity is often filled with opaque organic matters. Furthermore, there are two phases of the formation of the anhydrite/gypsum salt. The first phase is the small clasts that appeared over the thin section. The second phase is the ones in the mimic grain that formed after the dissolution of the dolomite (figure 5.30).

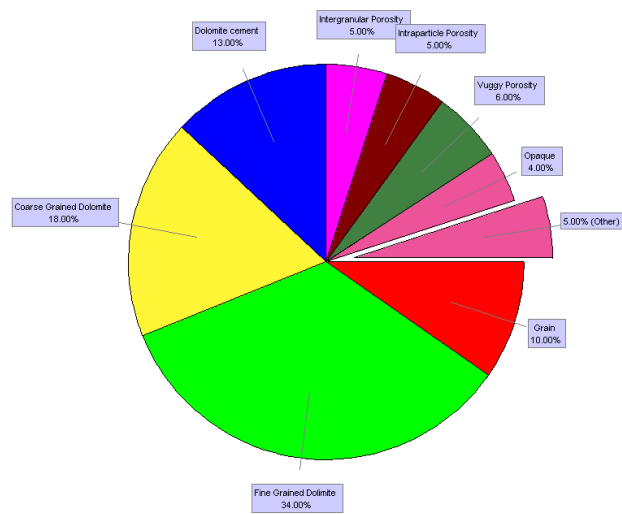


Figure 5.28. Quantification of BKLM-01-8.

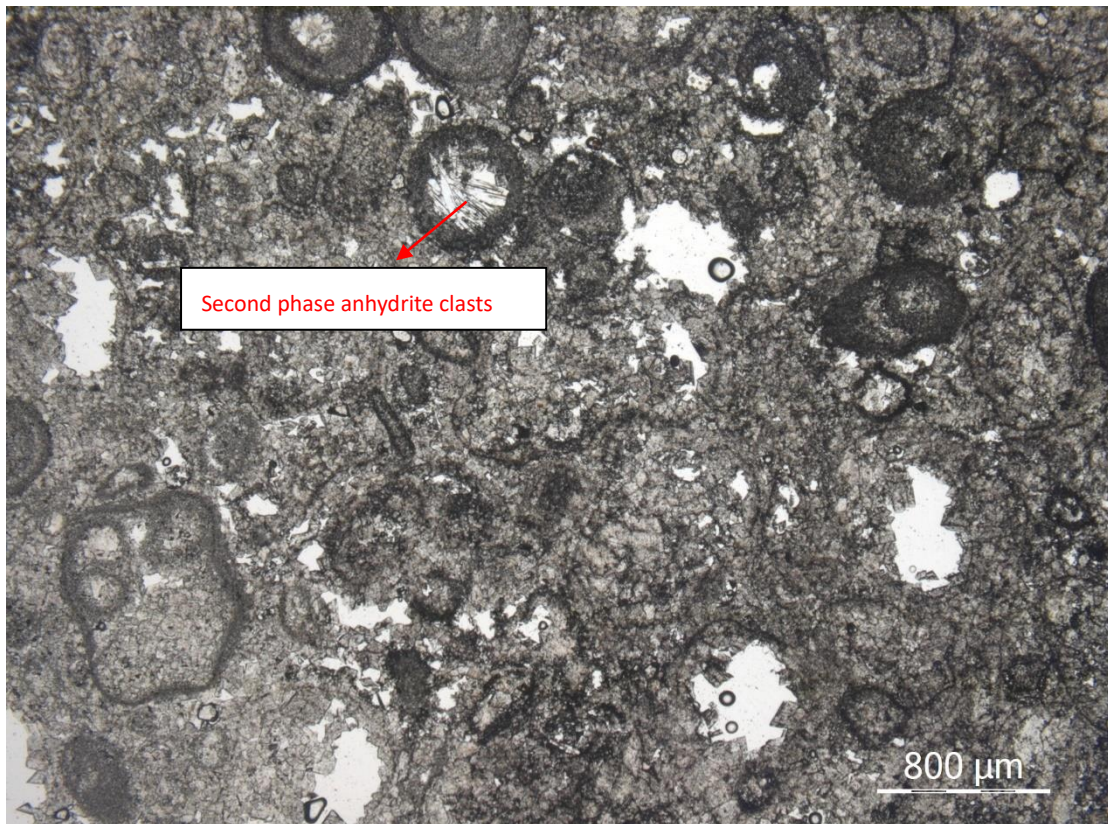


Figure 5.29. BKLM-01-8 under plane polarized light.

### 5.2.1.9. BKLM-01-9, Sequence 3, 1973.8m

The sample showed extensive diagenesis, matrix replacive, and polymodal. The fine-grained crystals are 20~40 $\mu\text{m}$  and planar texture. The coarse-grained crystals are ~100 $\mu\text{m}$ , but the crystals are non-planar. However, the sample lacks significant porosity. Intercrystal porosity is the most abundant type of porosity, which only accounts for 5% (figure 5.30). Clear stylolite can be seen in figure 5.30, which separates the two different grain-sized dolomite.

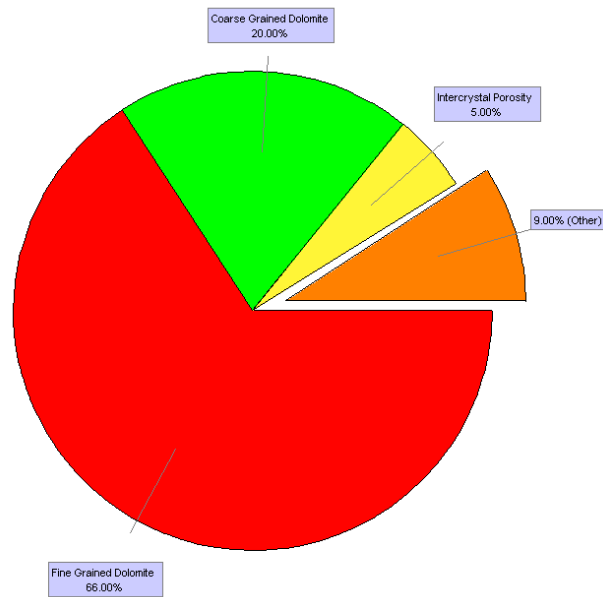


Figure 5.30. Quantification of BKLM-01-9.

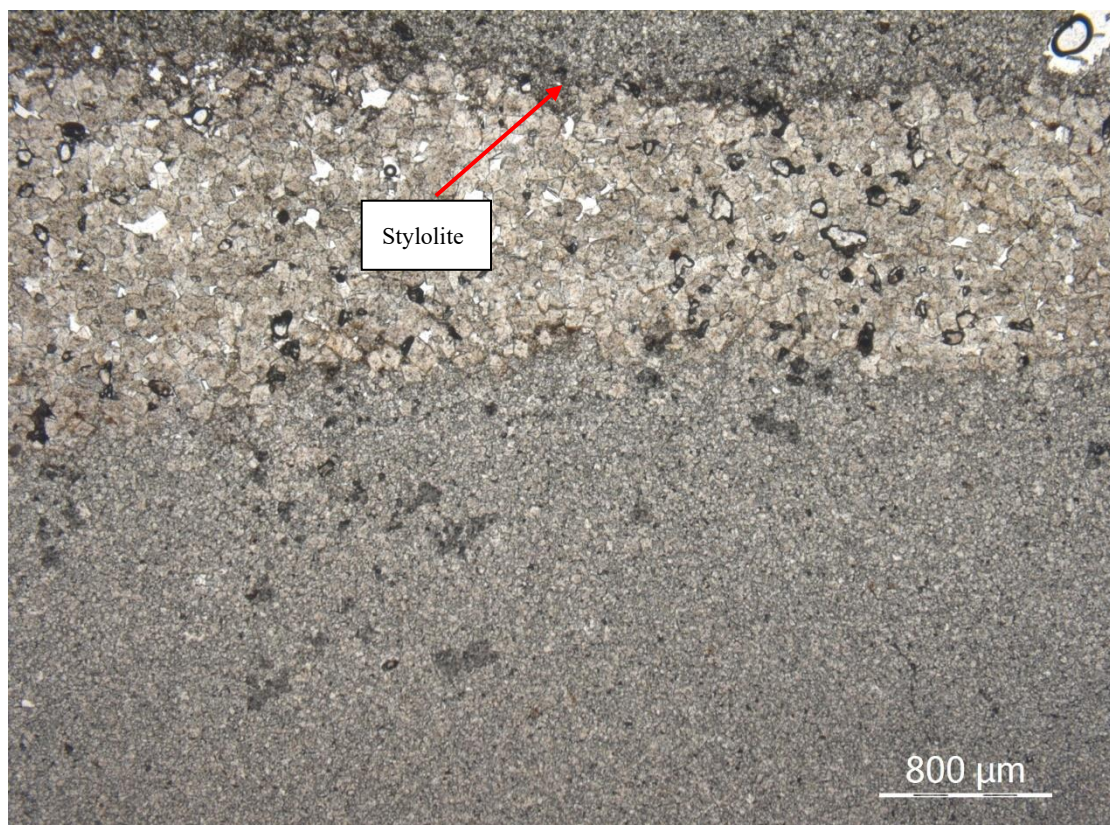


Figure 5.31. BKLM-01-9 under plane polarized light. Stylolite separated fine grained and coarse grained layer. Intercrystal porosity filled with opaque organic material.

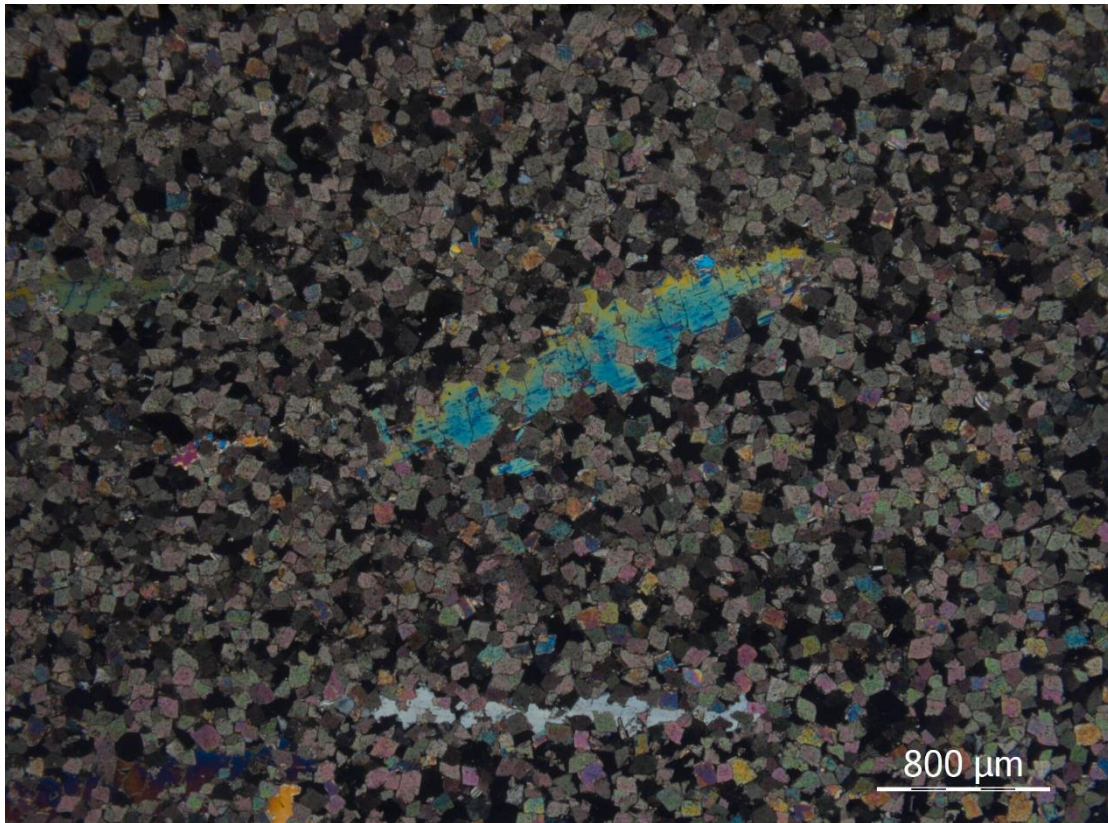


Figure 5.32. BKLM-01-9 under cross polarized light. Large anhydrite clast in between non-planar dolomite grains.

#### 6.2.1.10 BKLM-01-10, Sequence 3, 1969.2m

The last sample from BKLM-01 is a fine-grained dolomicrite (20-40 $\mu$ m). The dolomite crystals are matrix replacive, unimodal, and non-planar. The most abundant porosity type is intercrystal at 18%. The intercrystal pore spaces are often filled with opaque organic materials.

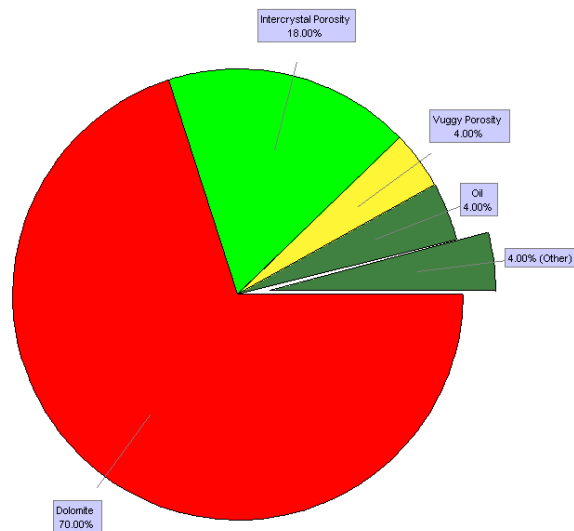


Figure 5.33. Quantification of BKLM-01-10.

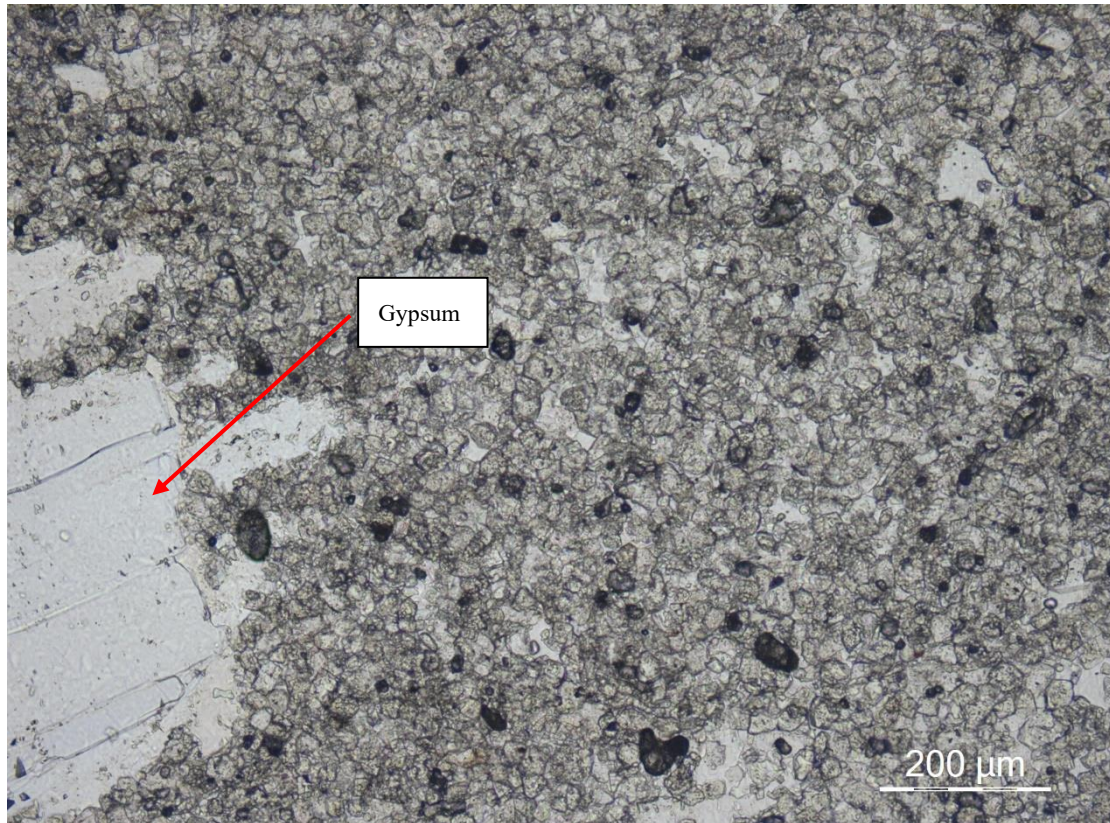


Figure 5.34. BKLM-01-10 under plane polarized light. Fine grained, non-planar dolomicrite. Pore spaces often filled with opaque organic matters. Colorless, low relief gypsum crystal at the left side of the figure.

## 5.2.2 BKLM-04

### 5.2.2.1 BKLM-04-1, Sequence 1, 2005m

The sample is matrix replacive, planar, and polymodal. The fine-grained mineral is around  $40\mu\text{m}$ , and the mid-grained mineral is around  $100\mu\text{m}$  (figure 5.35). Furthermore, the fine-grained crystals are often seen at stylolite (figure 5.36). There is also coarse-grained ( $\sim 200\mu\text{m}$ ) dolomite cement that formed during the burial of the

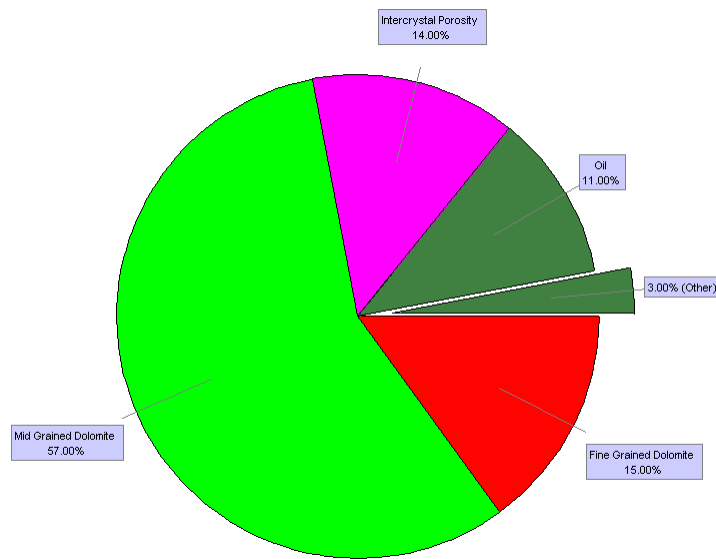


Figure 5.35. Quantification of BKLM-04-1.

dolomitization (figure 5.38). The dolomite cement in general, is granular mosaic texture that fills in the fractures. The sample lacks significant porosity. Porosity type is intercrystal, vug. The intercrystal porosity is often filled with opaque organic materials.



Figure 5.36. BKLM-04-1 under plane polarized light. Mid grained dolomicrite with stylolite in the middle which is composed of fine grained dolomite crystals.

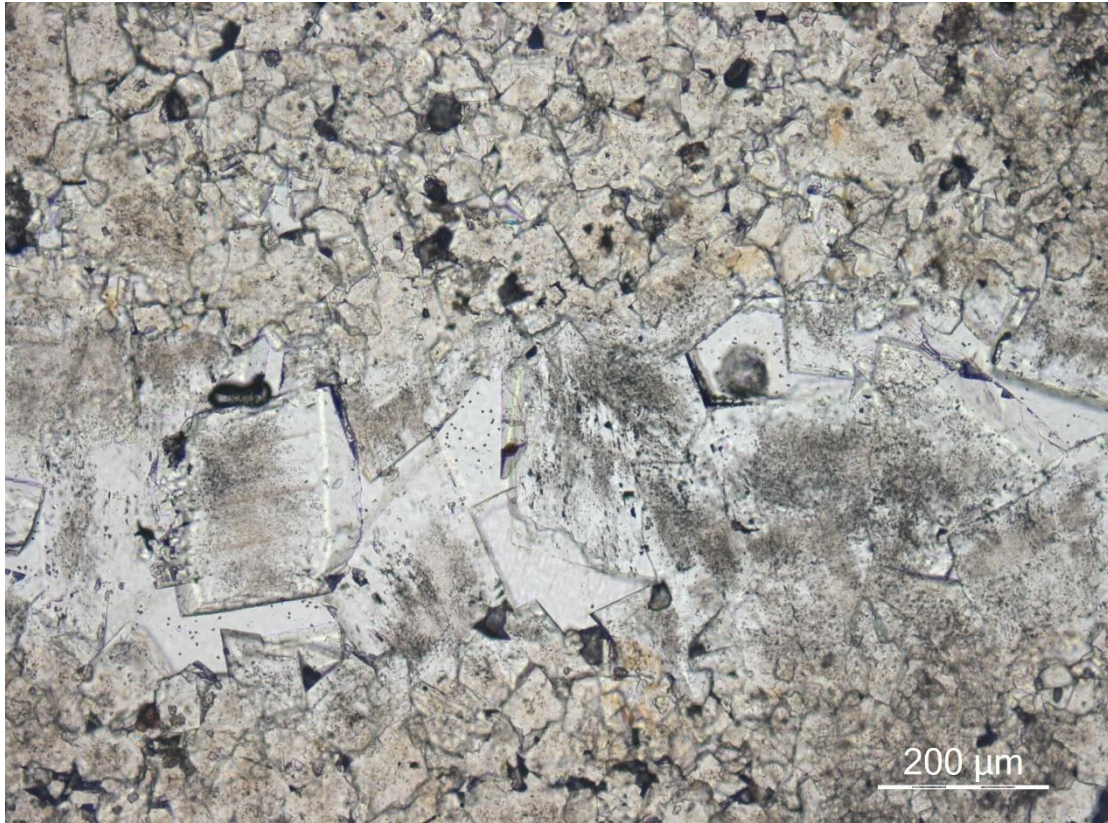


Figure 5.37. BKLM-04-1 under plane polarized light. Coarse grained dolomite cement (~200µm).

#### 5.2.2.2 BKLM-04-2, Sequence 1, 2000m

The sample contained moldic, vuggy porosity types, which are possibly evidence of oosparitic origin (figure 5.39). It is matrix replacive, non-planar, and polymodal. The fine-grained crystals are the mimic replacive grains (20-40µm), and the fine/mid-grained dolomites are the dolomitic matrix (figure 5.40). Intercrystal and vuggy porosities are the most common types. However, some of the dolomitic matrix is dissolved, and the vugs are connected and form channel porosity. In this particular sample, there are a massive amount of yellowish/light brown coloured minerals, which might be clay minerals or early stage of silicification, since tiny quartz minerals (~0.1-0.2mm) are also found in the sample.

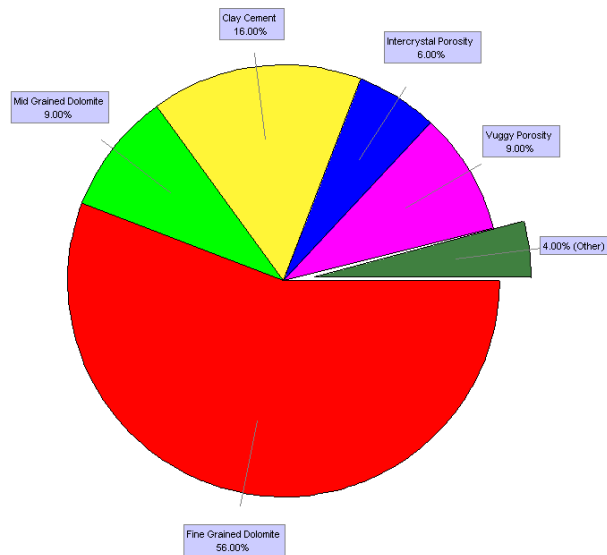


Figure 5.38. Quantification of BKLM-04-2.

there are a massive amount of yellowish/light brown coloured minerals, which might be clay minerals or early stage of silicification, since tiny quartz minerals (~0.1-0.2mm) are also found in the sample.

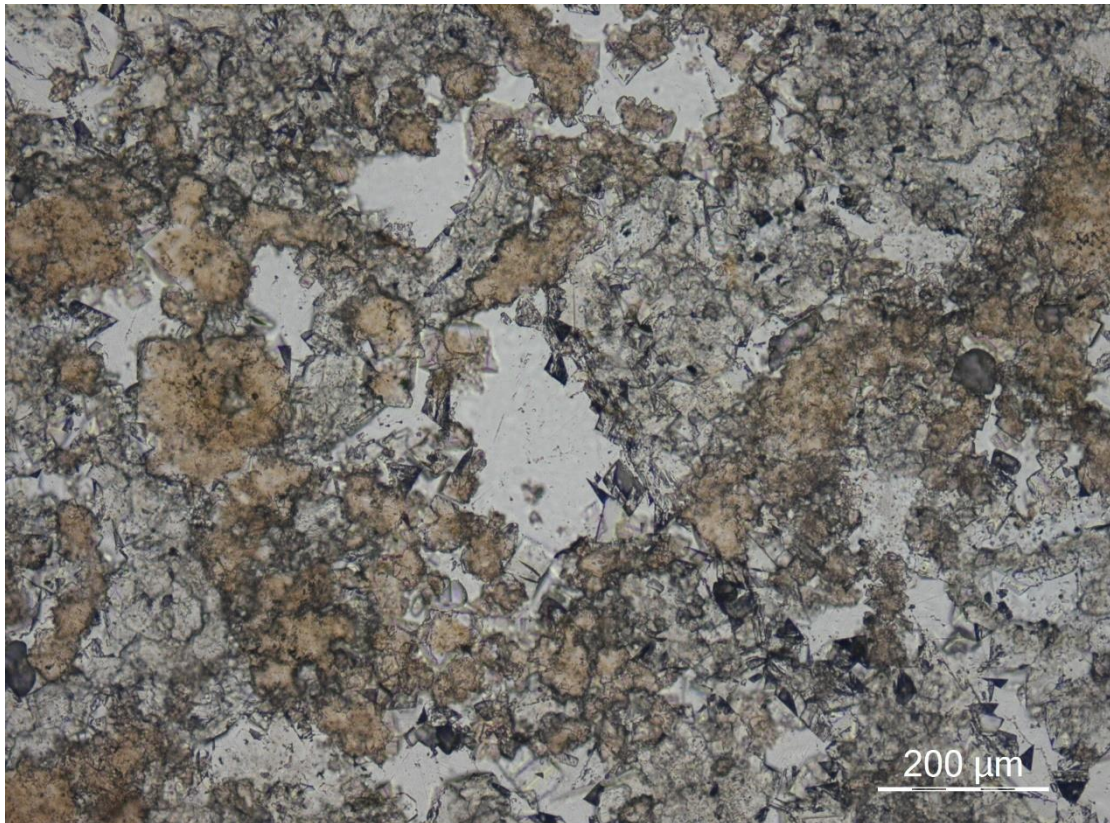


Figure 5.39. BKLm-04-2 under plane polarized light. Possible clay minerals surrounded the vugs.

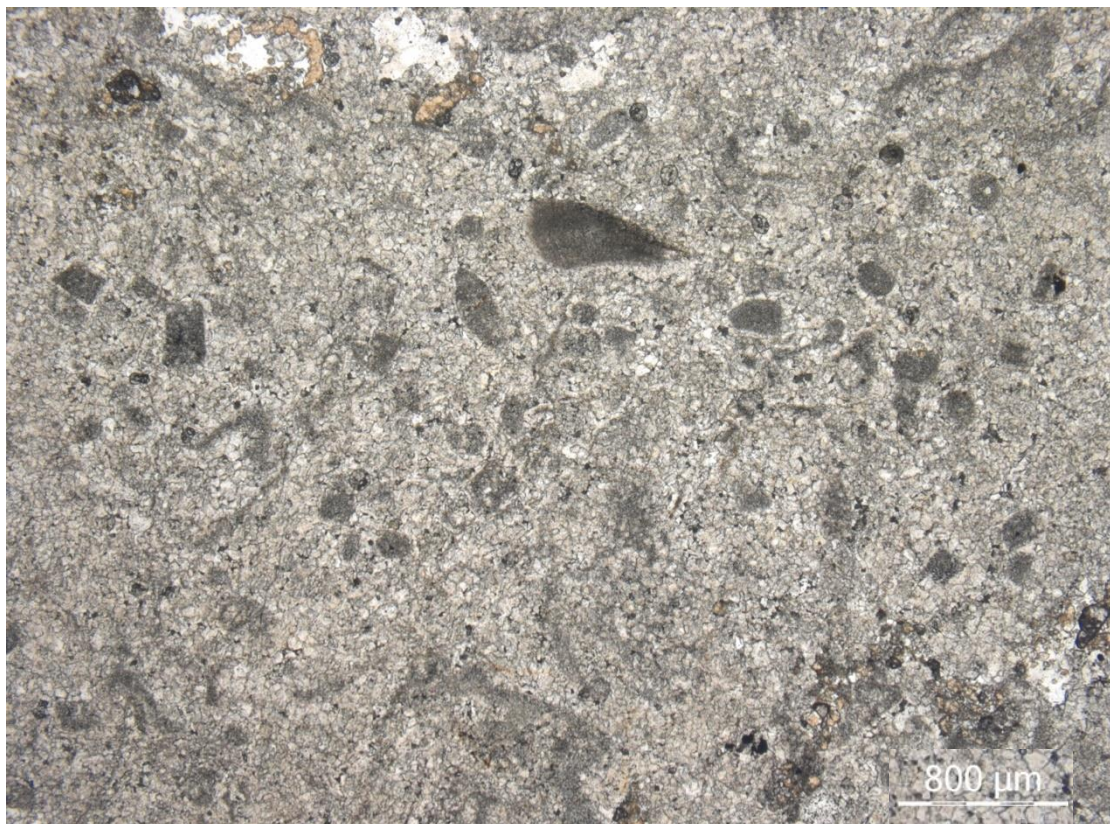


Figure 5.40. BKLm-04-2 under plane polarized light. Mimic dolomitized ooid grains (packstone).

### 5.2.2.3 BKLM-04-3, Sequence 1, 1998.5m

The rock sample is a grainstone with fine/mid-grained matrix. The dolomite crystals are matrix replacive, planar, and polymodal (figure 5.41). The mimic dolomitic grains are around 20 $\mu\text{m}$ , and the dolomitic matrix is around 60 $\mu\text{m}$ . There is also dolomitic cement in between the grains. The cement is mostly drusy or granular mosaic. The sample is relatively more porosity than the previous two samples. Most porosity types are intraparticle, granular, intercrystal, and vug (figure 5.42). Interclasts are also found in the thin section. Combining with previous observation, it is possible to say the original limestone is deposited in a subtidal environment. Furthermore, some of the ooid grains are replaced by quartz.

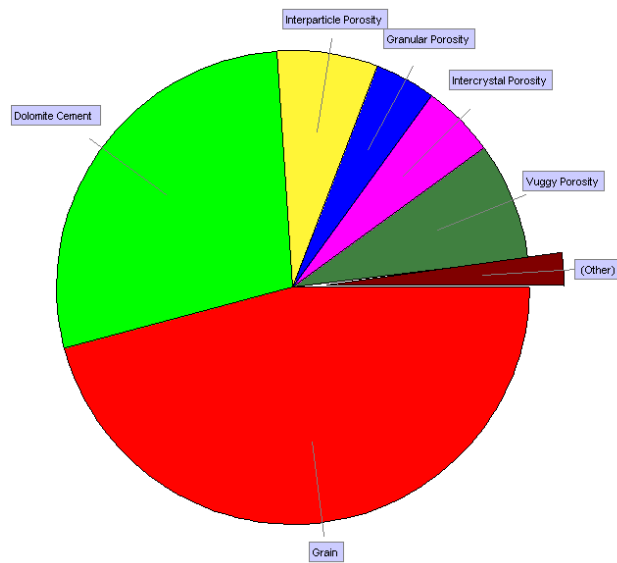


Figure 5.41. Quantification of BKLM-04-3.

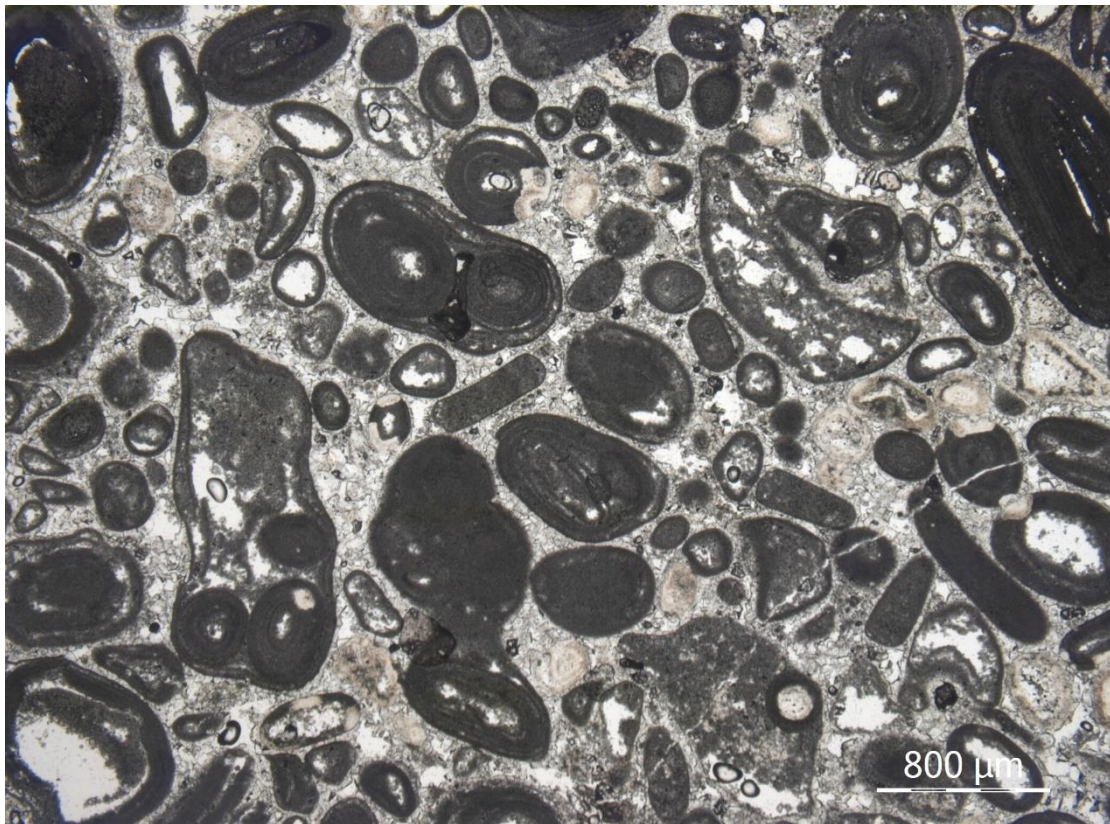


Figure 5.42. BKLM-04-3 under plane polarized light. Grainstone compacted with ~1 mm large shelly fossils, ooids, and interclasts with high porosity.

#### 5.2.2.4 BKLM-04-4, Sequence 1, 1994.5m

Compacted with ooids and shelly fossils, the sample is originally an oosparite (figure 5.43). The rock is a grainstone with fine/mid-grained dolomite matrix and cement. The dolomite is matrix replacive, planar and unimodal. And the dolomitic cement is drusy, meniscus texture and granular mosaic. The porosity types included intercrystal, granular, and interparticle (figure 5.44(a)). However, the sample lacks significant porosity. Small anhydrite clasts can be spotted in the dolomitic matrix. The second phase of anhydrite clasts can be found in the mimic dolomitized grains (figure 5.44(b)) formed after the dissolution of dolomite.

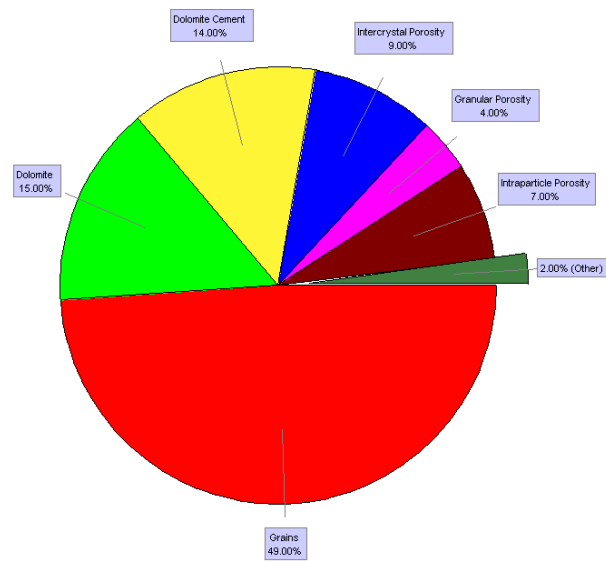


Figure 5.43. Quantification of BKLM-04-4.

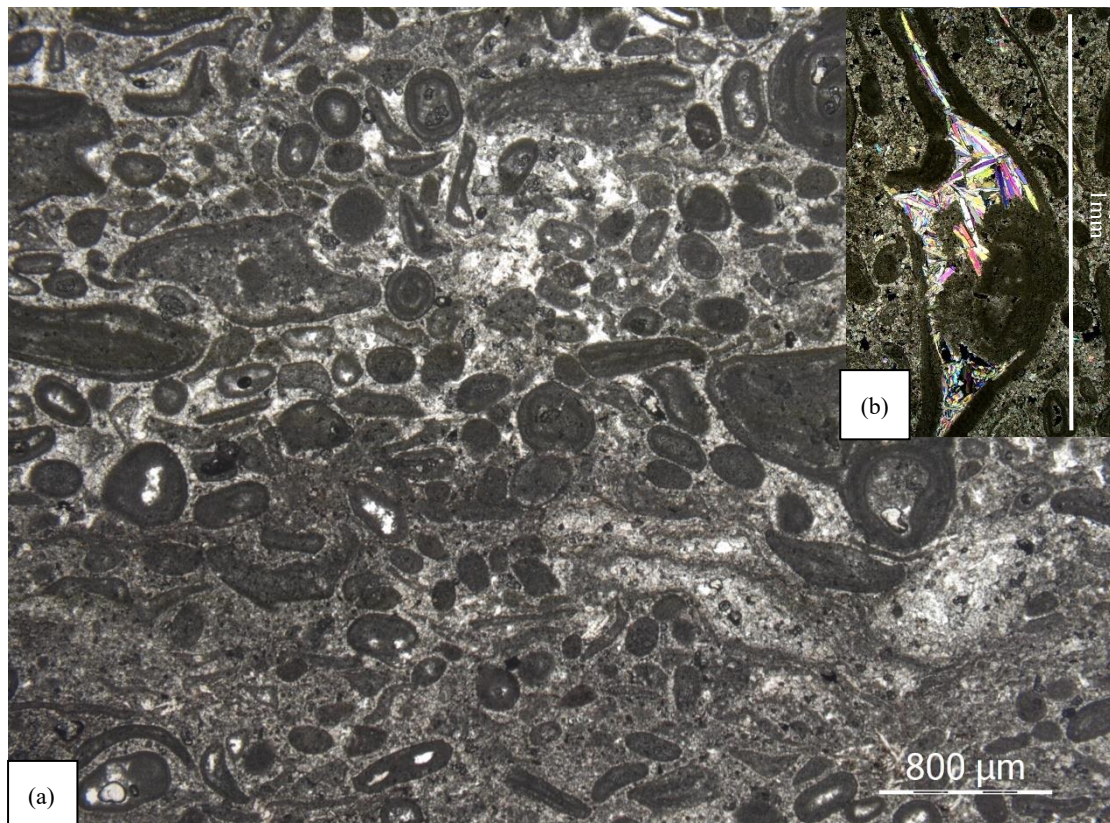


Figure 5.44. (a) BKLM-04-4 under plane polarized light with mimic dolomitized grains around  $400\mu\text{m}$  and interclasts around  $800\sim 1000\mu\text{m}$ . (b) BKLM-04-4 under cross polarized light. Second phase anhydrite clasts in dolomitized grain.

#### 5.2.2.5. BKLM-04-5, Sequence 1, 1989.7m

The sample is fine/mid-grained dolomicrite ( $\sim 20\mu\text{m}$ ). The crystalline is matrix replacive, non-planar, and unimodal. Although the sample is a fine-grained dolomicrite, it has relatively high intercrystal porosity (18%) (figure 5.45). The pore spaces are often filled with opaque matters, which might be oxide minerals, organic matters, or oil (figure 5.46).

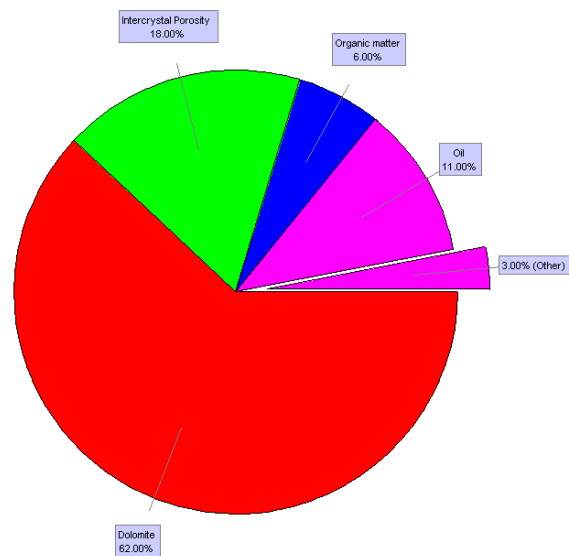


Figure 5.45. Quantification of BKLM-04-5.

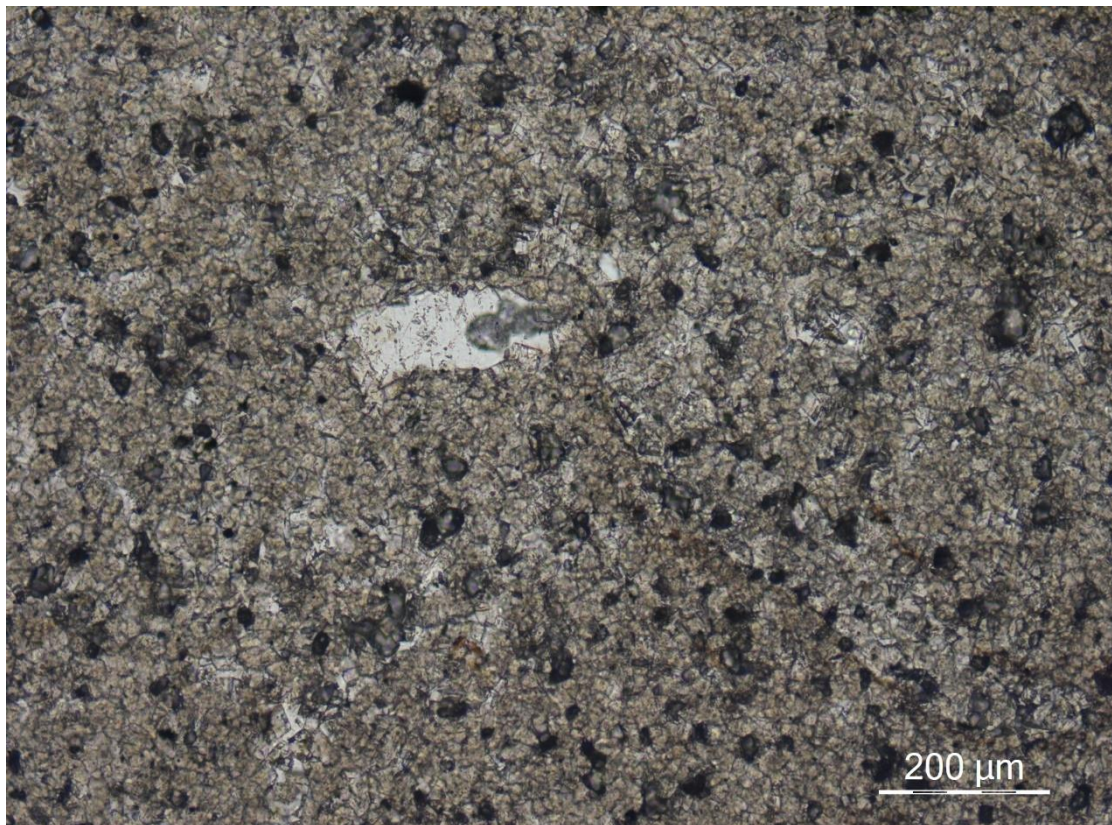


Figure 5.46. BKLM-04-5 under cross polarized light. Fine/mid grained dolomicrite. And gypsum crystal in the middle of the photo.

### 5.2.2.6. BKLM-04-6, Sequence 1, 1984.9m

The sample is a packstone with the mid-grained dolomitic matrix. The dolomitic crystalline is matrix replacive, planar, and polymodal. The mimic dolomitized grains are  $\sim 40\mu\text{m}$ , and the dolomitic matrix is  $80\sim 100\mu\text{m}$ . The sample also included dolomitic cement. The cement types mostly are dog tooth and drusy with granular mosaic. The porosity types of the sample included intergranular, intercrystal, intraparticle, modic and vug, which can be seen in figure 5.49 and 5.50, and the total porosity is 19%.

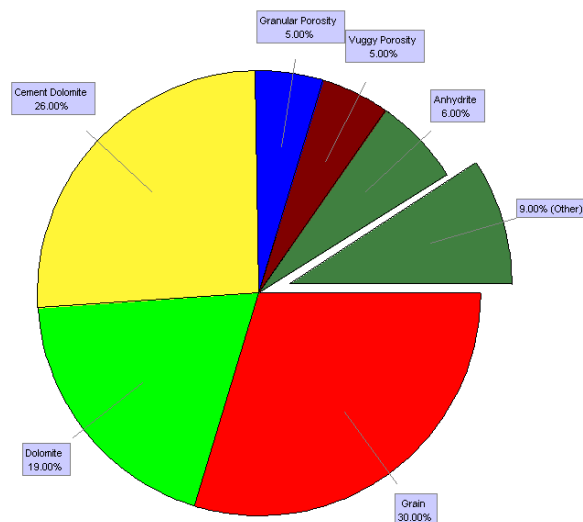


Figure 5.47. Quantification of BKLM-04-6.

Furthermore, large anhydrite clasts can be seen in the thin section as well. It is evidence that the rock might have experienced evaporation after dolomitization, which means the rock might have been deposited in a lagoon environment.

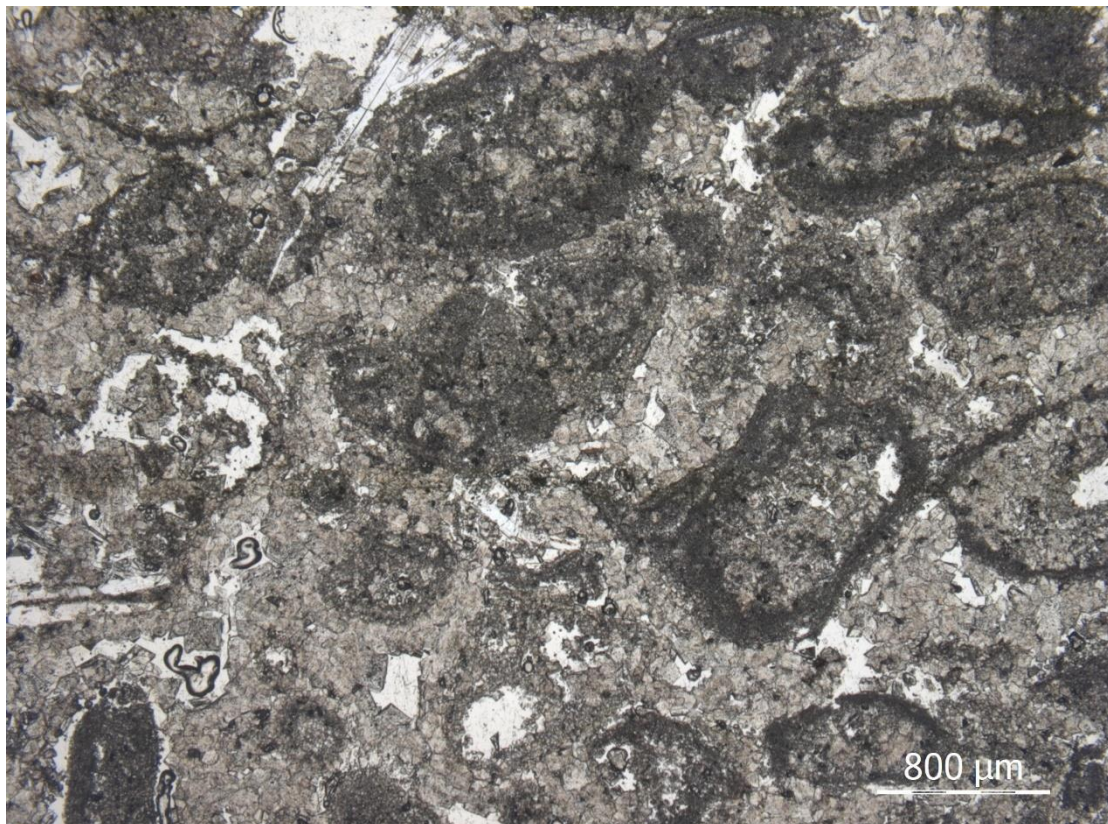


Figure 5.48. BKLM-04-6 under plane polarized light.

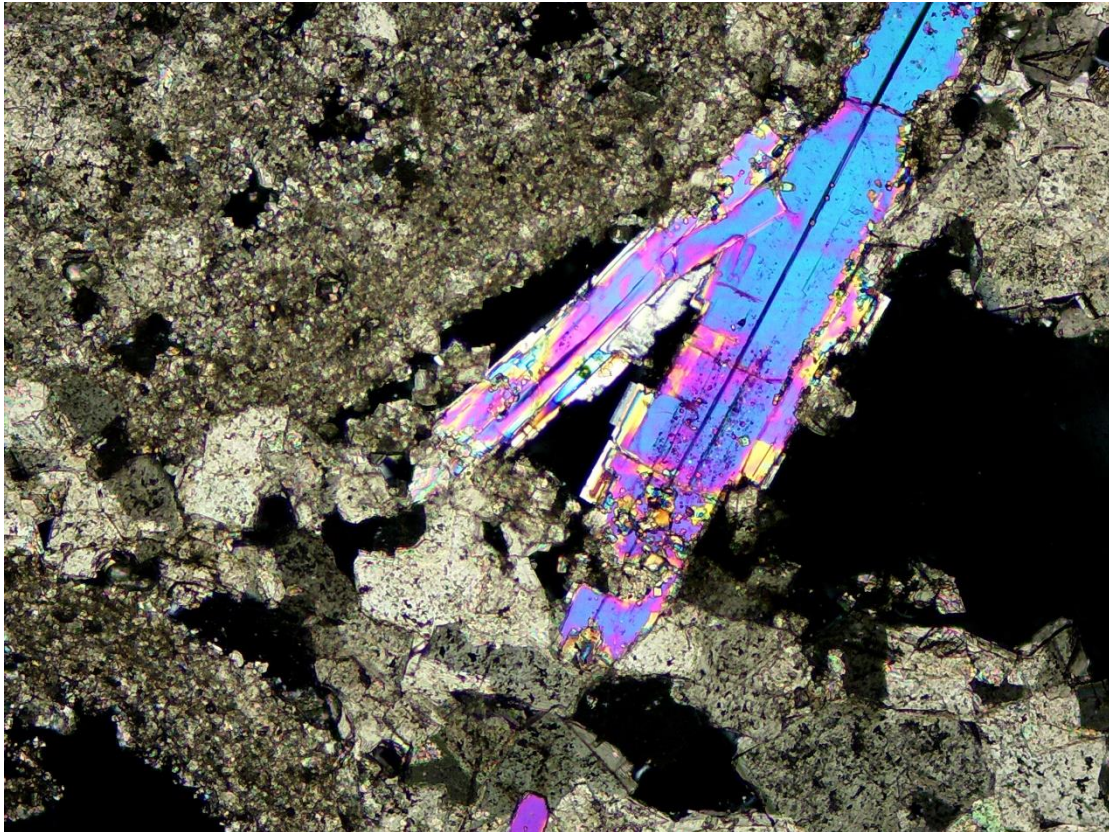


Figure 5.49. BKLM-04-6 under cross polarized light. 1mm long anhydrite clast grew in between the dolomitic cement, which is evidence that the rock experienced evaporation.

#### 5.2.2.7. BKLM-04-7, sequence 1, 1976.2m

The sample is a packstone. However, unlike other grain-supported samples, the mimic dolomitized grains are all dissolved, only 200~500  $\mu\text{m}$  sized molds and dolomitic matrix and cement left. The dolomitic matrix is replacive, planar, and unimodal. The dolomitic cement is drusy mosaic. Both matrix and cement crystalline are fine/mid-grained (80~100 $\mu\text{m}$ ).

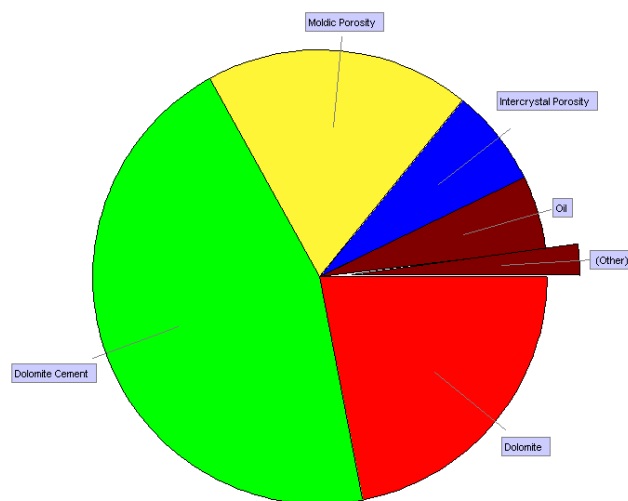


Figure 5.50. Quantification of BKLM-04-7.

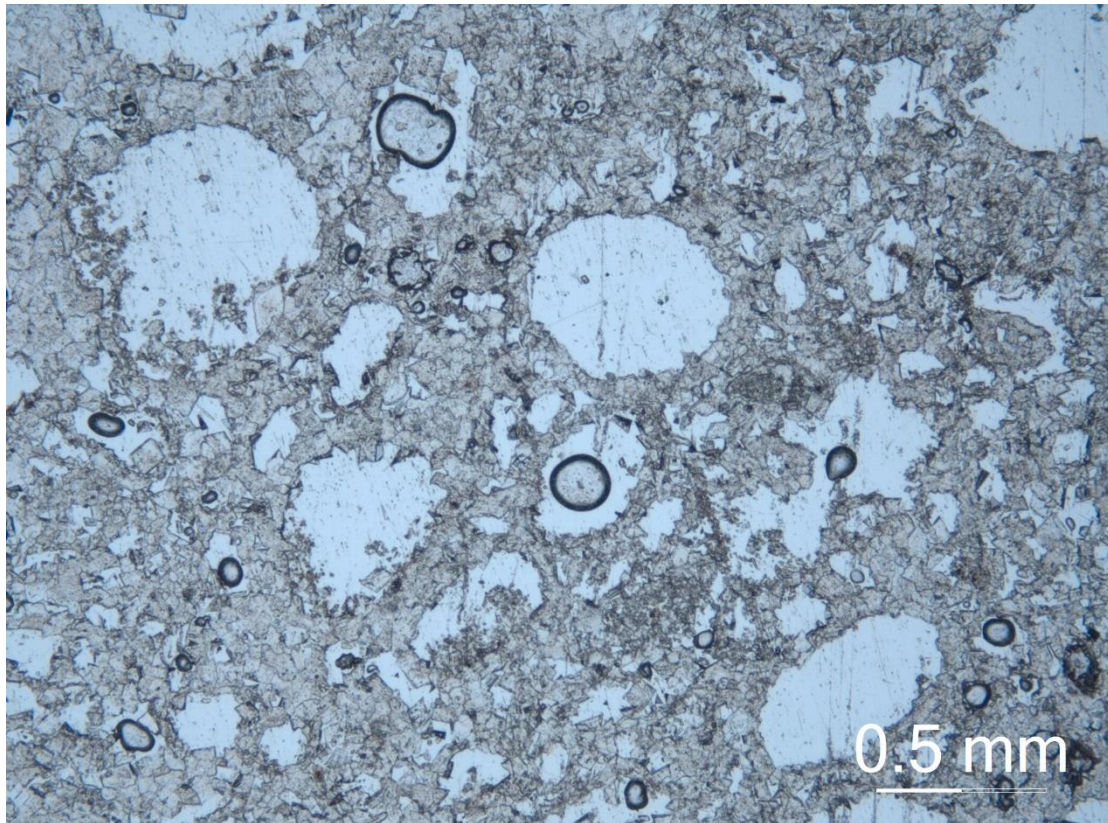


Figure 5.51. BKLM-04-7 under plane polarized light. Original grains are all dissolved, with molds left. The bubbles in the figure are side products of the poorly made thin section.

#### 5.2.2.8. BKLM-04-8, Sequence 2, 1973.8m

The sample is fine-grained ( $\sim 50\mu\text{m}$ ). It is matrix replacive, planar, and unimodal (figure 5.53(a)). The porosity types in the sample are mostly intercrystal and vug (figure 5.52). The intercrystal porosity is often filled with opaque materials, which might be organic matters or oil. And the clay minerals can be found in the larger vugs (1mm) (figure 5.53(b)).

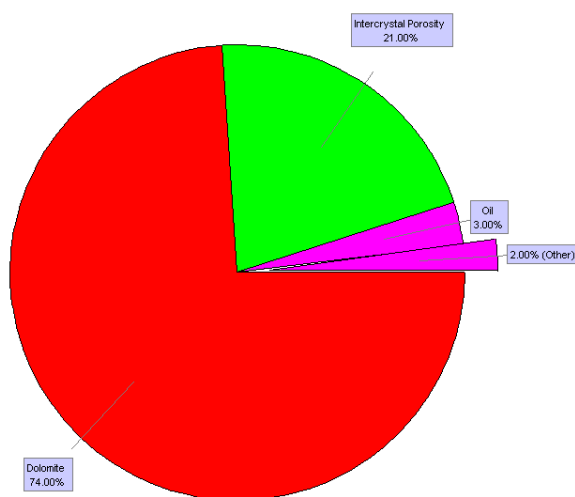


Figure 5.52. Quantification of BKLM-04-8.

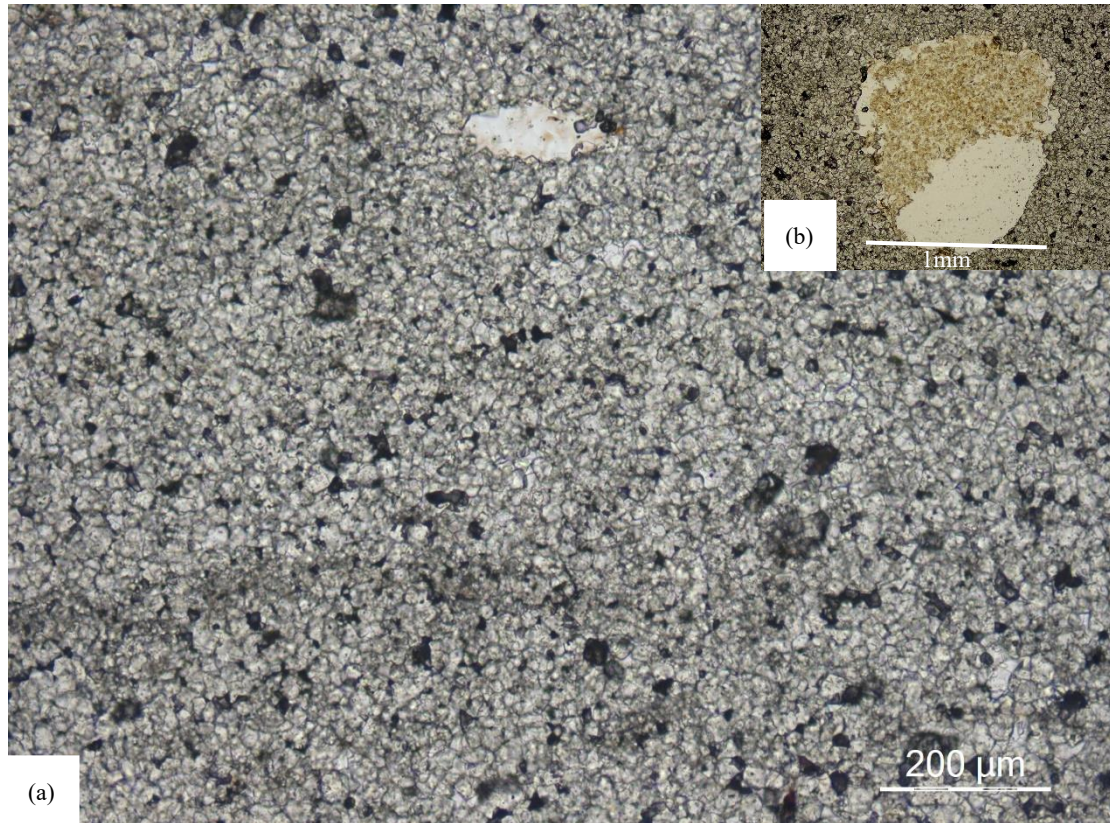


Figure 5.53. (a) BKLM-04-8 under plane polarized light. (b) Possible clay mineral with in the vug.

#### 5.2.2.9 BKLM-04-9, Sequence 2, 1972.8m

The sample is a fine-grained dolomitic. It is matrix replacive, planar, and polymodal (fine-grained and very fine-grained). The two layers are separated by stylolite (figure 5.53). the fine-grained dolomite is  $\sim 40\mu\text{m}$ , and the very fine-grained dolomite is  $\sim 20\mu\text{m}$ . Furthermore, the stylolite is filled with organic matter. The most common porosity types are intercrystal and vugs. The intercrystal porosity is often filled

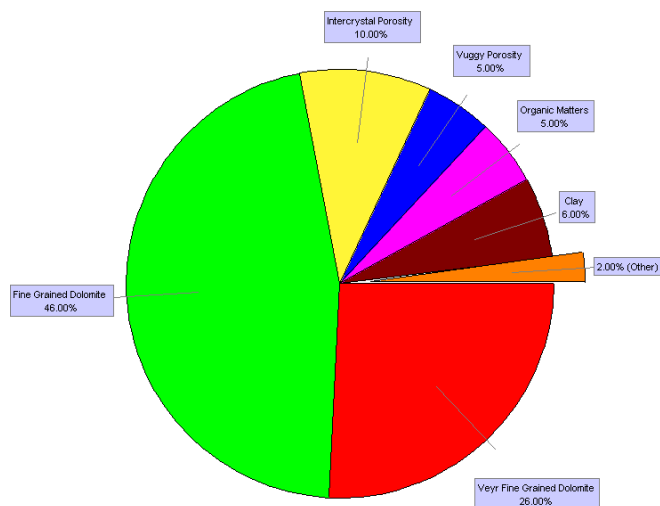


Figure 5.54. Quantification of BKLM-04-9.

with opaque organic matters, and the larger vuggy porosity is more often seen in the very fine-grained layer. Large needle-shaped anhydrite grains ( $600\sim 1000\mu\text{m}$ ) are only seen in the fine-grained layer (figure 5.55). This might be caused by the stylolite acting as a seal between the fine-grained and very fine-grained layer. The seal allowed water to flow through the coarse-grained layer. Therefore the crystals can grow larger



Figure 5.55. BKLM-04-8 under cross polarized light. Very fine grained layer sandwiched between two fine grained layer by stylolite.

#### 5.2.2.10. BKLM-04-10, Sequence 2, 1964.2m

The sample is a grainstone, originally oosparite (figure 5.57). The sample is matrix replacive, planar, and polymodal. The fine-grained mimic dolomitic grains are  $\sim 20\mu\text{m}$ , and the dolomitic matrix is  $\sim 40\mu\text{m}$ . The dolomitic cement between the grains is generally meniscus and granular mosaic. The porosity types included modic, granular, intercrystal, and vug. The intercrystal pore spaces are often filled with opaque materials. Furthermore, small (0.1mm) anhydrite clasts can also be seen in the thin section.

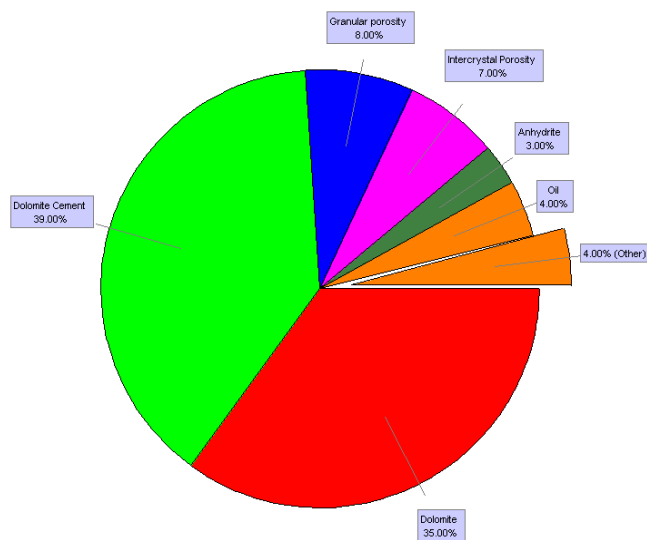


Figure 5.56. Quantification of BKLM-04-10.

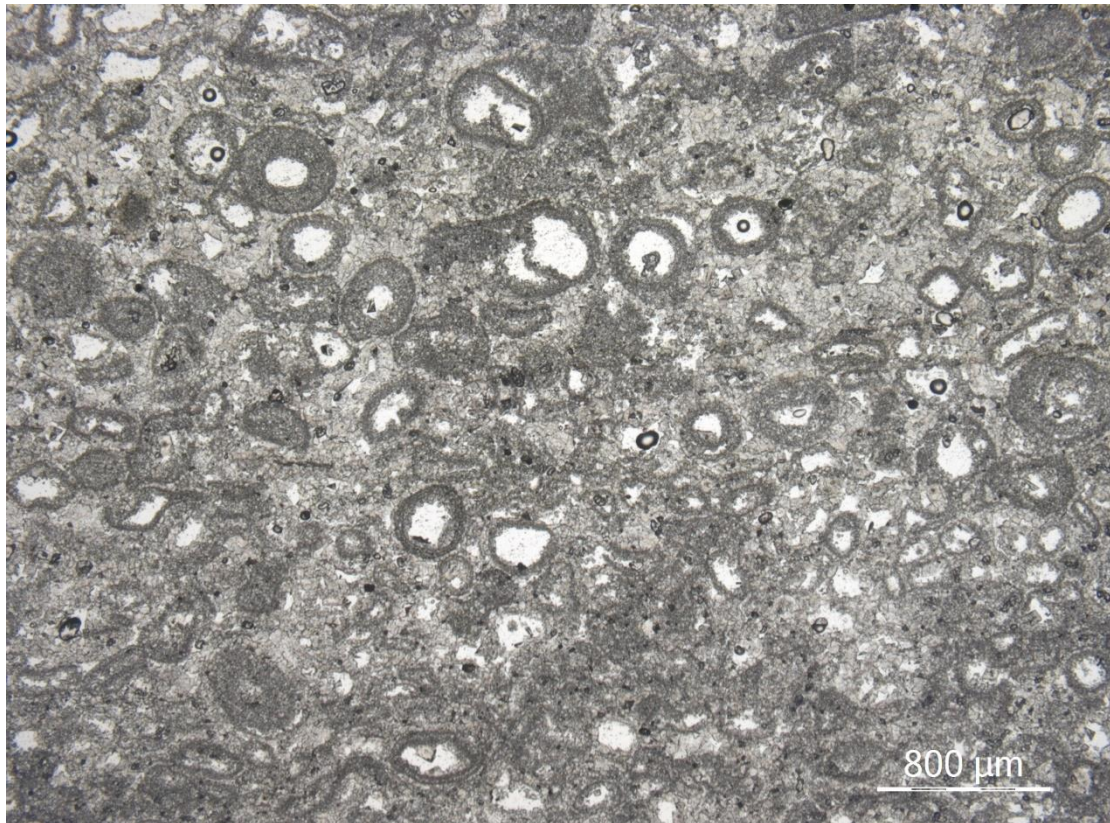


Figure 5.57. BKLm-04-10 under plane polarized light.

#### 5.2.2.11. BKLm-04-11, Sequence 2, 1957.8m

The sample is almost the same as the previous sample, but the mimic dolomitized grains are larger (600~800 $\mu\text{m}$ ) (figure 5.59). The sample is grainstone with fine-grained dolomitic matrix (~50 $\mu\text{m}$ ). It is matrix replacive, non-planar, and polymodal. The dolomitized grains are ~20 $\mu\text{m}$ , the dolomitic matrix is ~50 $\mu\text{m}$ , and the dolomitic cement is ~80 $\mu\text{m}$  (figure 5.58). The dolomitic cement texture is dog tooth, drusy, and granular mosaic. The porosity types are intergranular, intercrystal, and vug. Opaque materials can also be found within the intercrystal porosity, as well as small anhydrite clast.

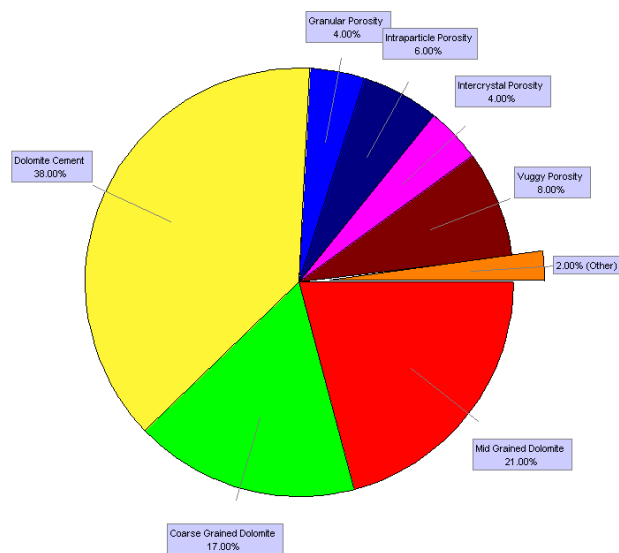


Figure 5.58. Quantification of BKLm-04-11.

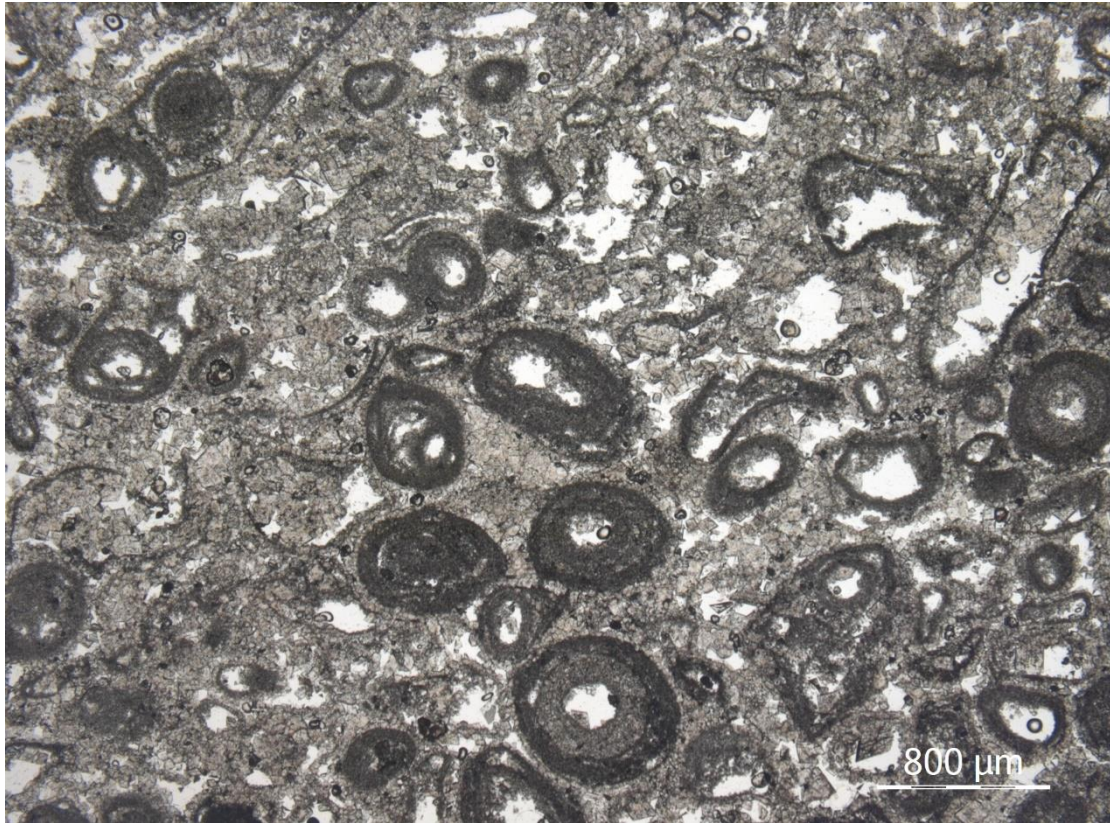


Figure 5.59. BKLm-04-11 under plane polarized light.

#### 5.2.2.12. BKLm-04-12, Sequence 3, 1956.2m

The sample is a mid-grained dolomiticrite. It is matrix replacive, planar, and polymodal. The fine-grained dolomite is  $\sim 40\mu\text{m}$  (54%), and the mid-grained dolomite is  $\sim 100\mu\text{m}$  (20%) (figure 5.60). The porosity is generally intercrystal, and the crystalline is not compacted. Hence, the porosity is relatively high (20~25%). Furthermore, larger anhydrite crystals can be found in the thin section (figure 5.61).

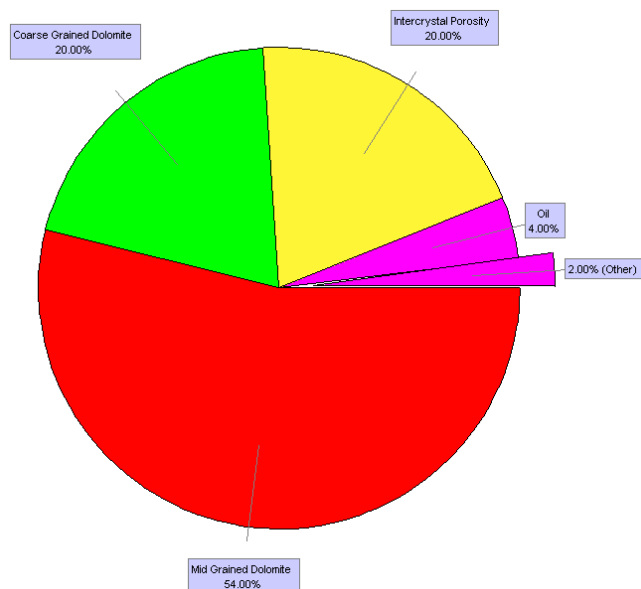


Figure 5.60. Quantification of BKLm-04-12.

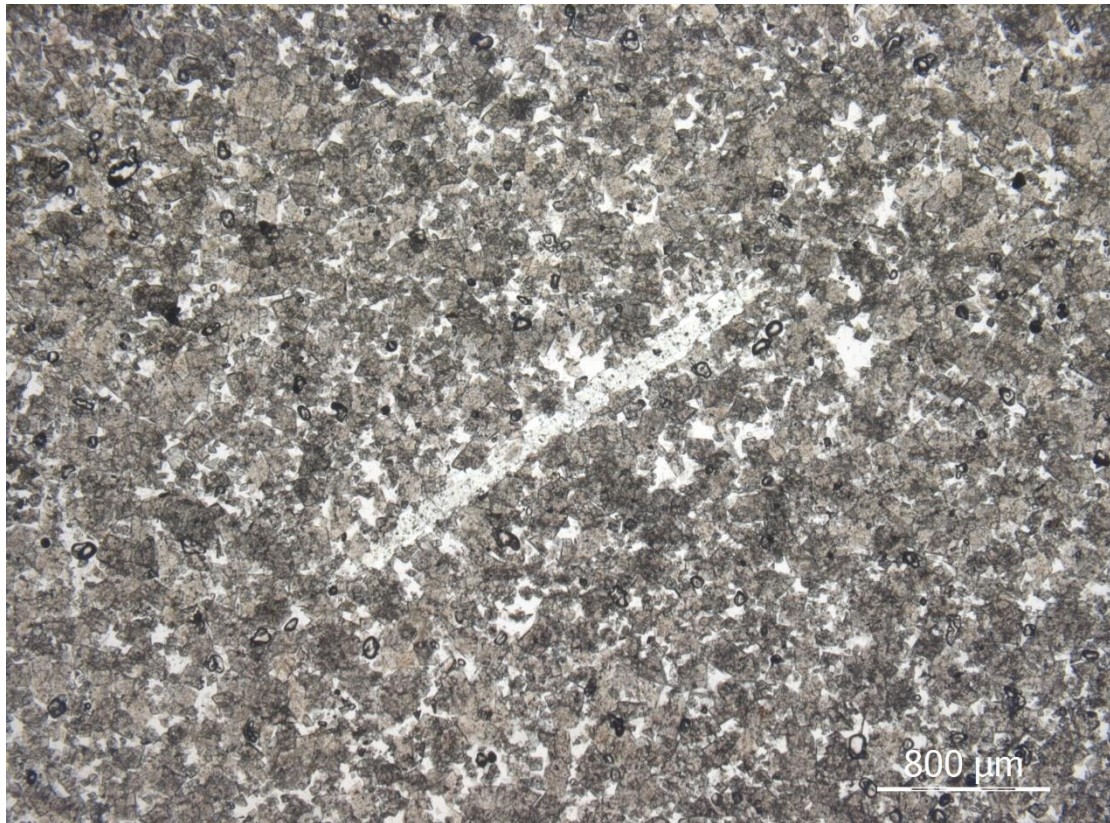


Figure 5.61. BKLm-04-12 under plane polarized light. A large anhydrite crystal (~1.2mm) can be seen in the center of the image

#### 5.2.2.12 BKLm-04-13, Sequence 3, 1951.8m

The sample is fine-grained dolomicrite (20~40μm). It is matrix replacive, planar, and unimodal. The porosity types are intercrystal and vug (figure 5.62). And the opaque materials are often found in the intercrystal pore space.

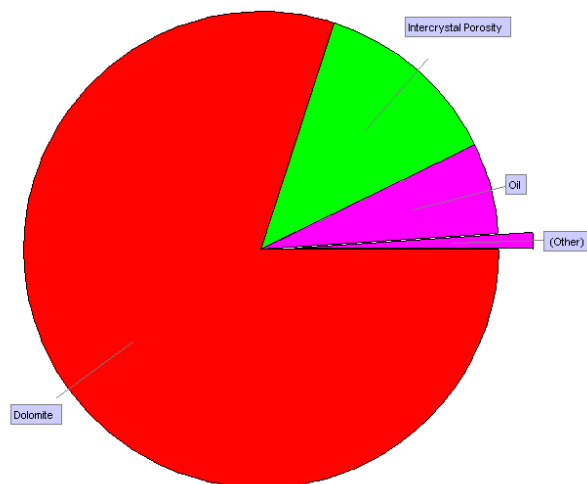


Figure 5.62. Quantification of BKLm-04-13.

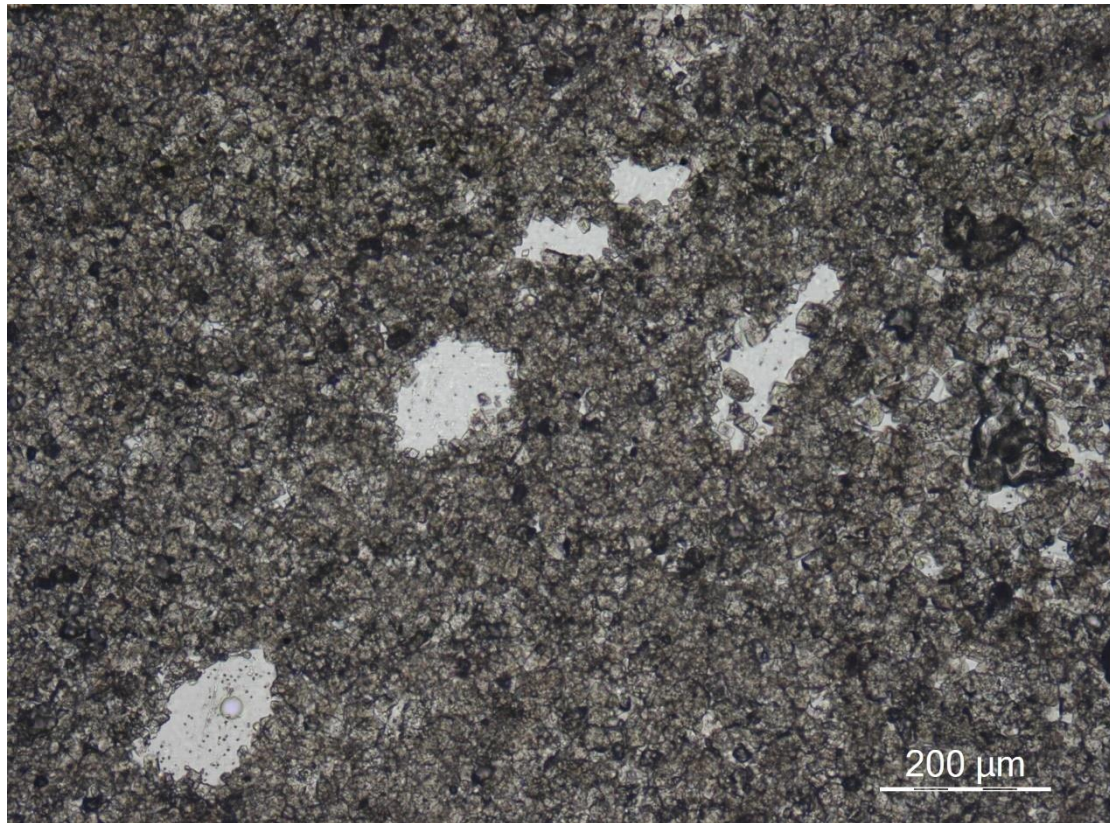


Figure 5.63. BKLM-04-13 under plane polarized light. Fine grained dolomiticite with 200µm vugs.

#### 5.2.2.14 BKLM-04-14, Sequence 4, 1949.6m

This sample is almost the same fine-grained dolomiticite as the previous sample. Even the quantification is similar (figure 5.64). However, there is dark material in the sample, which might be iron oxide or clay (figure 5.66).

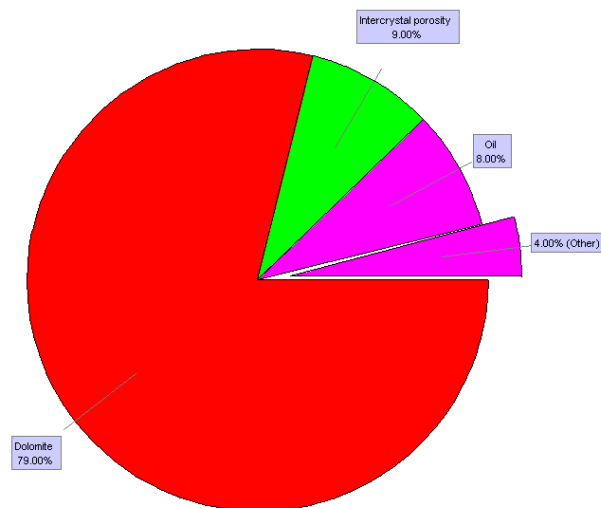


Figure 5.64. Quantification of BKLM-04-14.

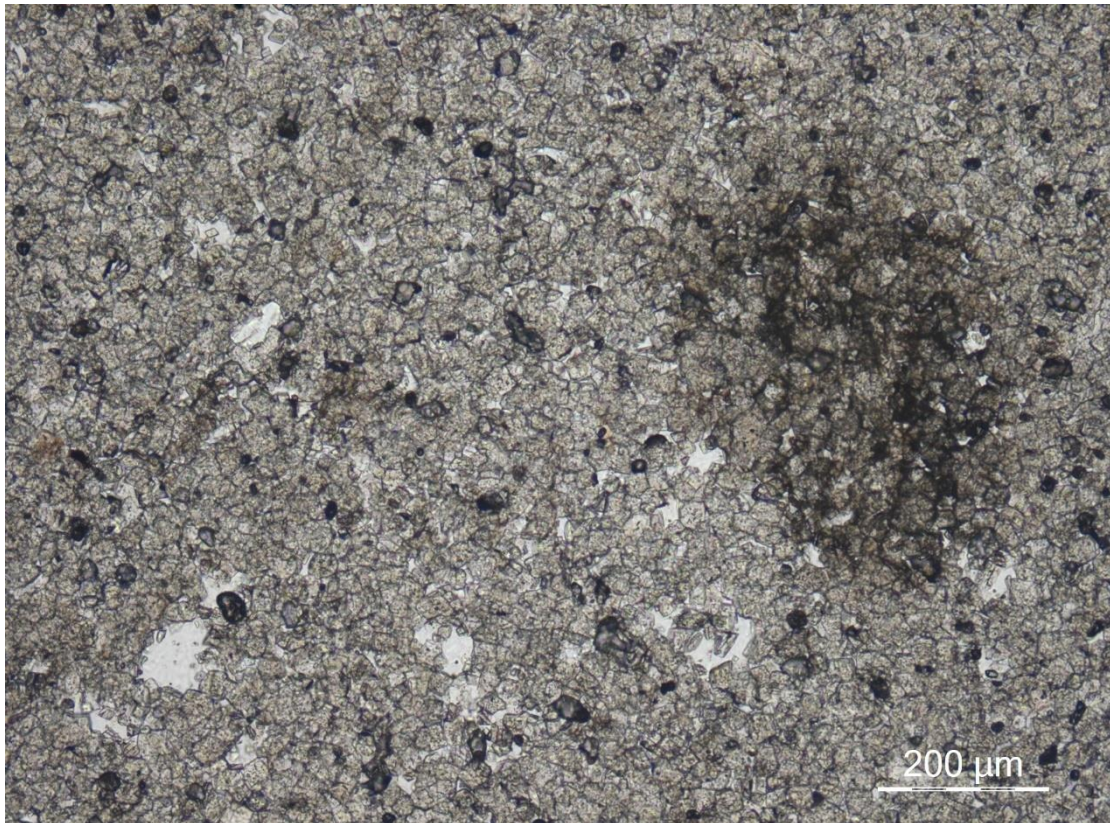


Figure 5.65. BKLM-04-14 under plan polarized light. Dark materials on the right that might be iron oxide or clay material.

#### 5.2.2.15 BKLM-04-15, Sequence 4, 1947.2m

Similar fine-grained dolomicrite as previous two samples, with similar quantification (figure 5.66). However, the crystalline is slightly more compacted than BKLM-04-14 (figure 5.65, 5.67).



Figure 5.66. Quantification of BKLM-04-15.

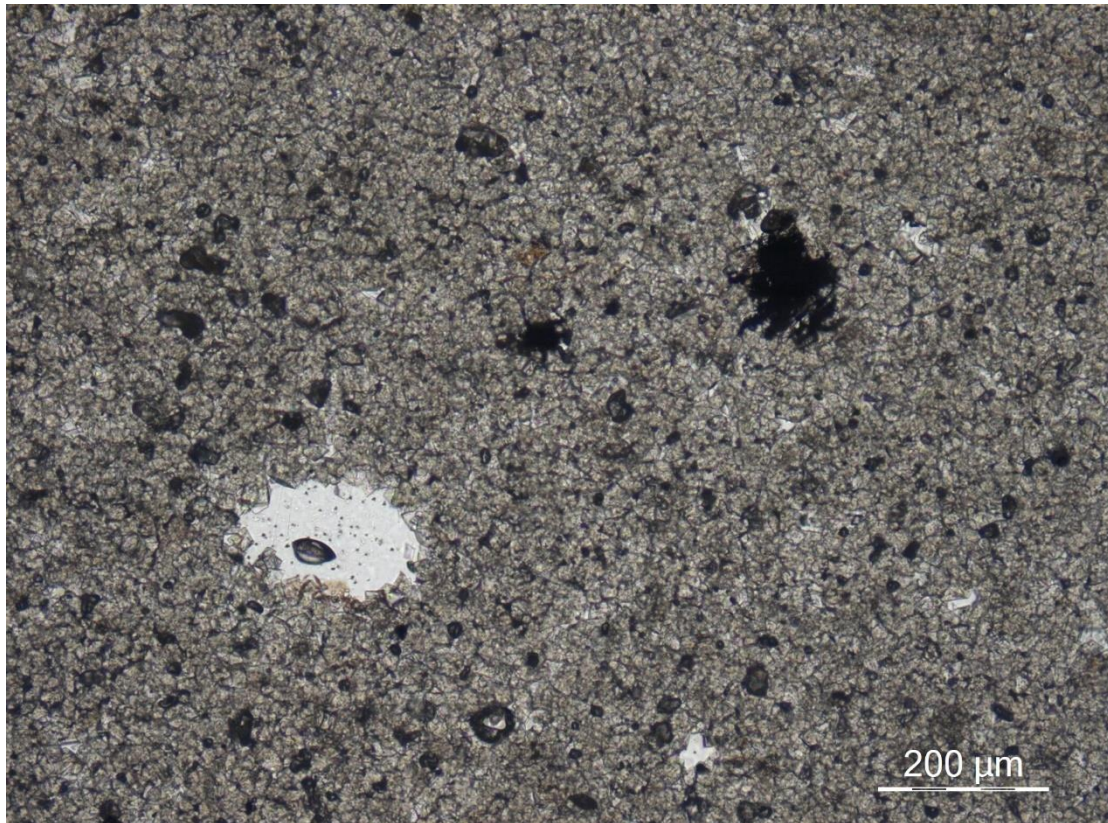


Figure 5.67. BKLM-04-14 under plane polarized light.

### 5.2.3. Cathodoluminescence Microscopy (CL)

When viewed under CL, all the dolomite rock samples reflected a general mottled red color (figure 5.68, 5.69). All the anhydrite, gypsum and clay minerals are black (figure 5.69(e)). The small shiny bright, yellow-coloured dots on the dolomite crystal shown in figure 5.68 and figure 5.69 are pyrite. The dolomite crystals in both figures showed carpet-like structure, which could mean that all the dolomite in all the samples formed under uniform conditions (temperature and pressure) simultaneously during the burial of shallow marine deposits.

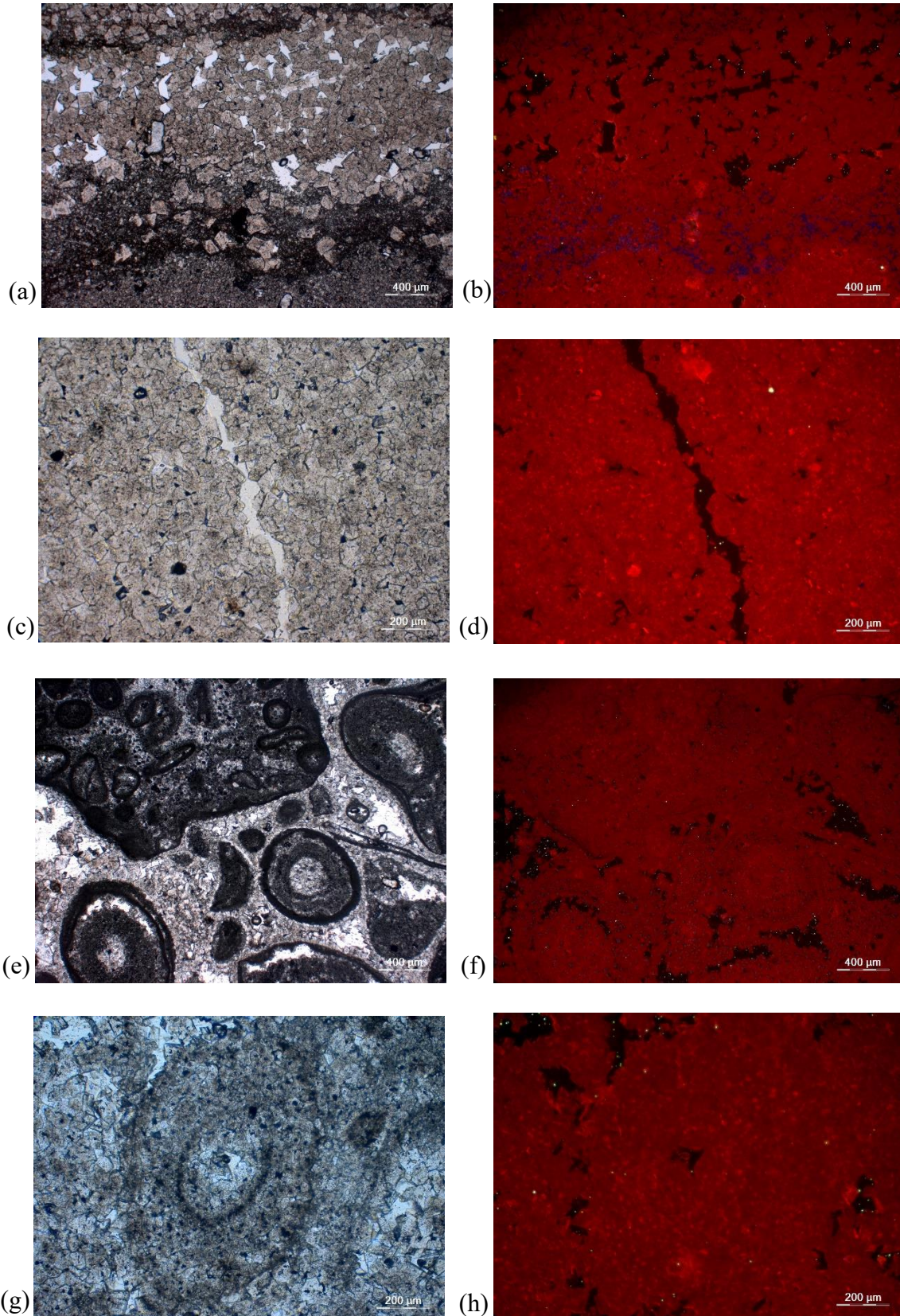


Figure 5.68. BKLM-01 (a) 1973.8m under PPL; (b) 1973.8m under CL; (c) 1978.7m under PPL; (d) 1978.7m under CL; (e) 1981.8m under PPL; (f) 1981.8m under CL; (g) 1986.2m under PPL; (h) 1986.2m under CL.

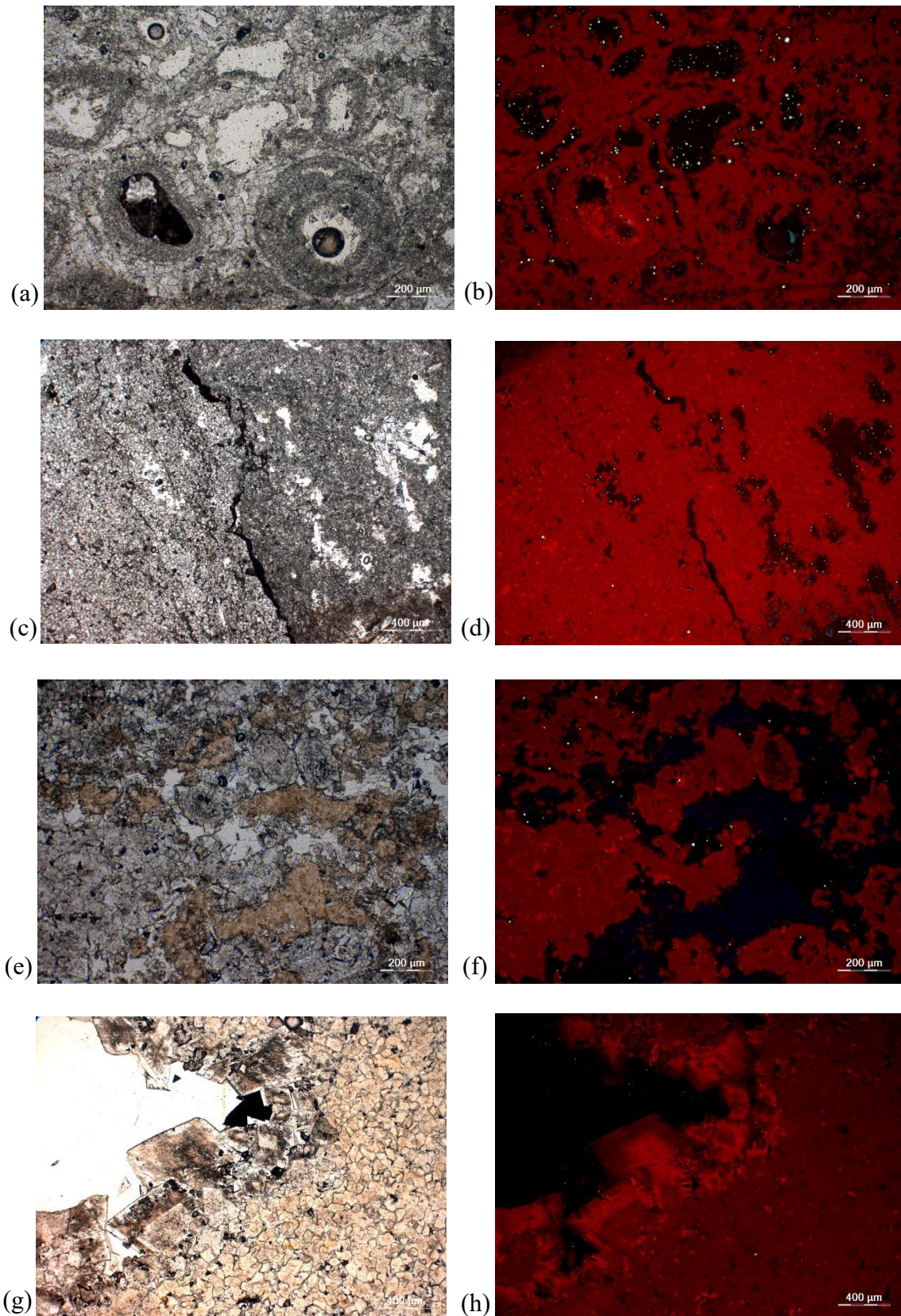


Figure 5.69. BKLM-01 (a) 1964.2m under PPL; (b) 1964.2m under CL; (c) 1972.8m under PPL; (d) 1972.8m under CL; (e) 1999.8m under PPL; (f) 1999.8m under CL; (g) 2005m under PPL; (h) 2005m under CL.

#### 5.2.4, Staining with Alizarin Red S and Potassium Ferricyanide

Alizarin Red S and potassium ferricyanide are often used to distinguish between carbonate minerals. From observing the core samples and the thin section analysis, it is known that the entire research samples are composed of dolomite. Hence, after staining with Alizarin Red S, the thin section samples appear colourless (figure 5.70, 5.71). After staining with potassium ferricyanide, all the rock samples still appear colourless, which means the rock samples are non-ferroan carbonate (figure 5.70, 5.71).

#### 5.2.5. Petrographic Log and Quantitative Result

In figure 5.72, both wells showed that when the samples are more grain supported, the grain size is usually larger, especially in the BKLM-04 well. However, the petrology logs are drawn based on the 25 collected samples. The accuracy of the logs cannot represent the actual wells. Furthermore, based on the quantitative analysis of the lithology, porosity and mineral composition (gypsum/anhydrite content), BKLM-01 well can be separated into five sequences, and the BKLM-04 well can be separated into seven sequences (table 5.1). The sub-sequences separated the fine-grained, matrix-supported dolomiticrite, and the coarse-grained, grain-supported grainstone.

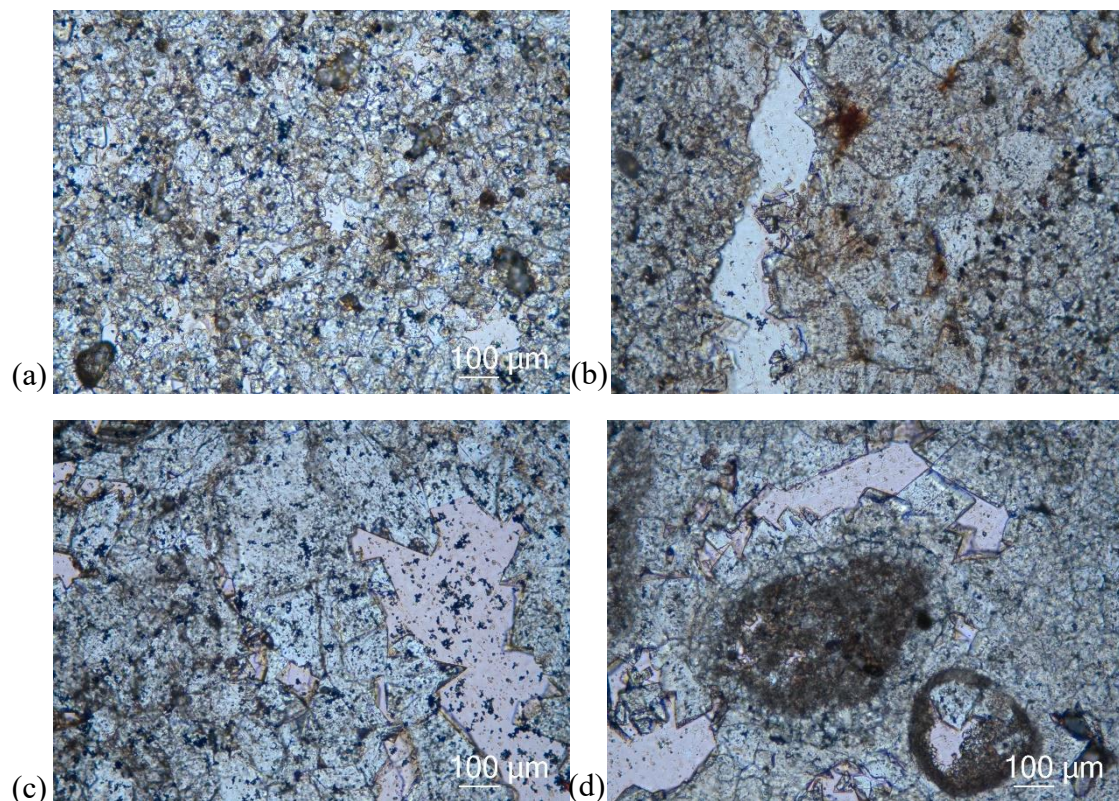


Figure 5.70. Stained BKLM-01 samples under PPL (a) 1969m; (b) 1973m; (c) 1975m; (d) 1981m.

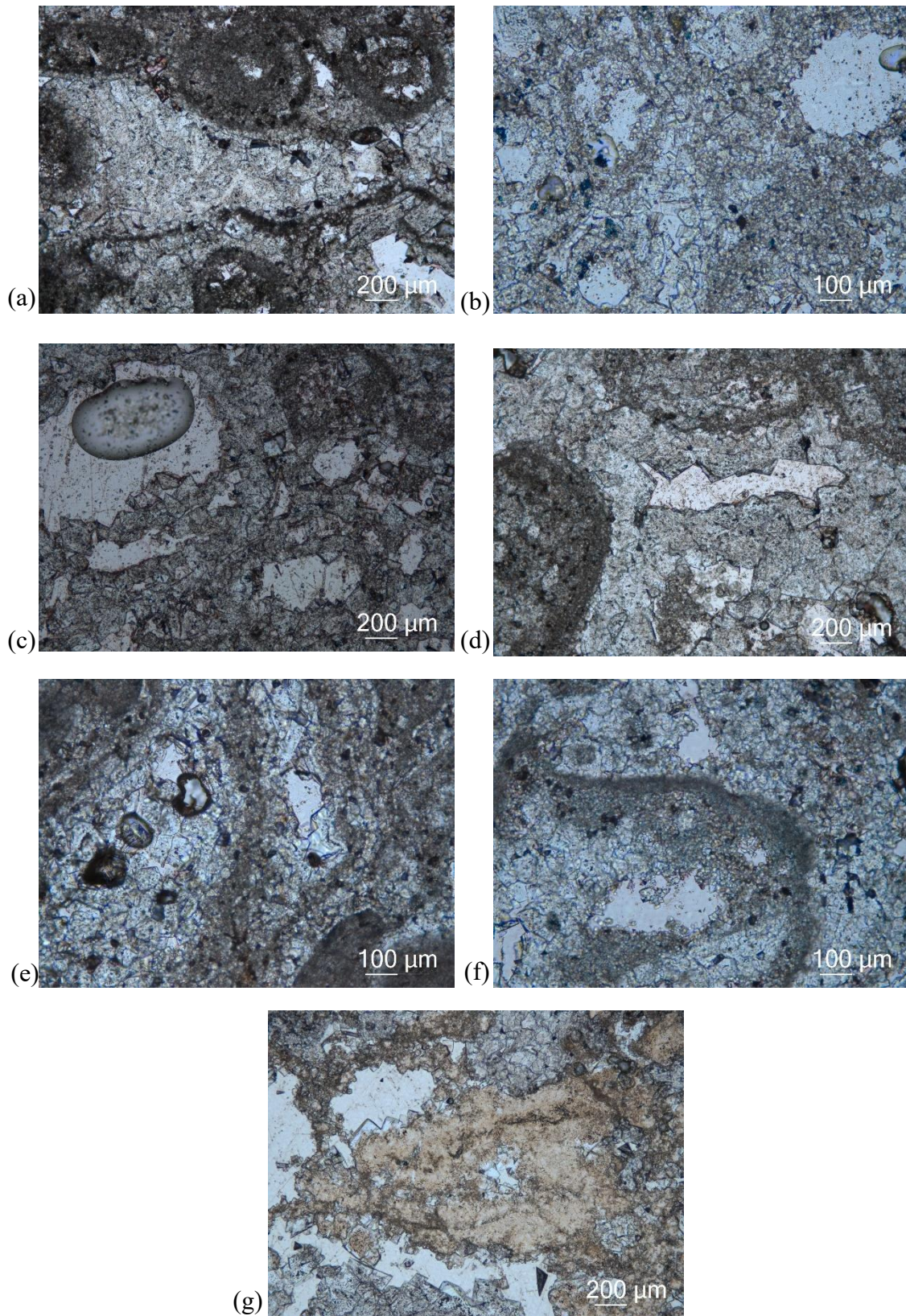


Figure 5.71. Stained BKLM-04 samples under PPL (a) 1957m; (b) 1964m; (c) 1976m; (d) 1984m; (e) 1994m; (f) 1998m; (g) 2000m.

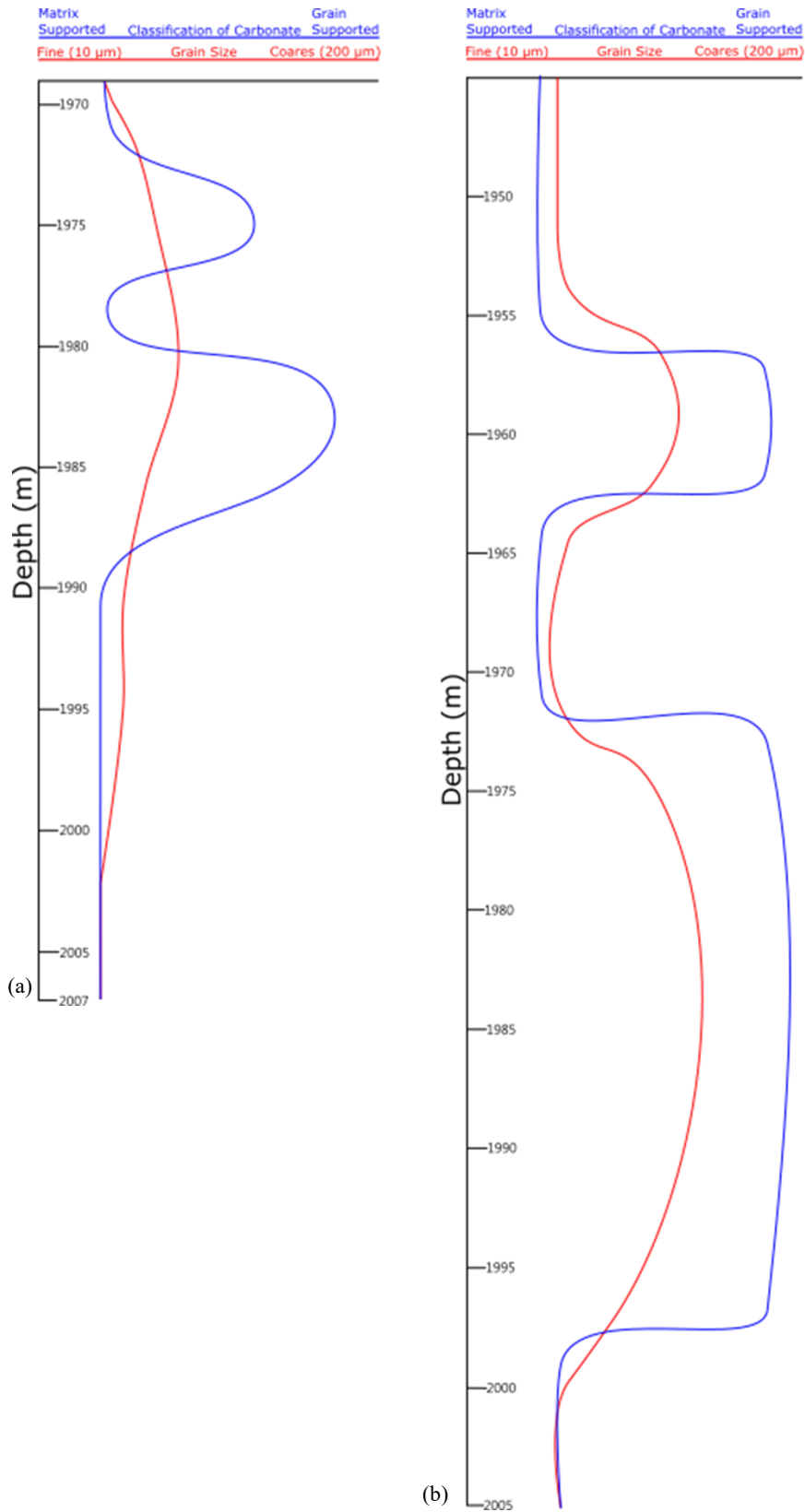


Figure 5.72. Petrographic log. (a) BKL01; (b) BKL04



Table5.1. The result of quantitative analysis.

BKLM 01	Depth (m)	Original Limestone	Dolomite	Cement	Porosity	Anhydrite/Gypsum	Quartz	Clay	Opaque
0.043.549	2003.9	cannot be classified							
0.043.551-1	1995.5	cannot be classified	76.50%	0%	10.50%	0%	0%	0%	13%
0.043.551-2	1993.5	Granoblastic							
0.043.546	1991.2	cannot be classified	75%	0%	12.50%	5%	0.00%	0%	7.50%
0.043.542-1	1986.2	Oosparite							
0.043.542-2	1981.8	Oosparite	62%	20%	16%	2%	0%	0%	0%
0.043.543-1	1978.7	cannot be classified	75%	0%	21%	0%	0%	0%	4%
0.043.543-2	1975.2	Oosparite	62%	13%	21%	1%	0%	0%	3%
0.043.545-1	1973.8	cannot be classified							
0.043.545-2	1969.2	cannot be classified	74%	0%	23.00%	2%	0%	0%	2%
BKLM-04									
0.043.544	2005	cannot be classified	87%	8%	5%	0%	0%	0%	0%
0.043.537-1	2000	oosparite							
0.043.537-2	1998.5	oosparite	58%	17%	16%	<1%	<2%	7%	0%
0.043.541	1994.5	oosparite							
0.043.540	1989.7	cannot be classified	76%	0%	17%	0%	0%	0%	7%
0.043.539	1984.9	oosparite							
0.043.538	1976.2	oosparite	35.50%	35.50%	25.00%	4.00%	0%	0%	0%
0.043.536-1	1973.8	cannot be classified							
0.043.536-2	1972.8	cannot be classified	75%	0%	18.00%	1.00%	0%	4.00%	2%
0.043.535	1964.2	oosparite							
0.043.534-1	1957.8	oosparite	43.50%	29.00%	25.00%	2.00%	0%	0%	0%
0.043.534-2	1956.2	cannot be classified							
0.043.532-1	1951.8	cannot be classified							
0.043.532-2	1949.6	cannot be classified	77.50%	0%	19.50%	3%	0%	0%	0%
0.043.532-3	1947.2	cannot be classified							

### 5.3. Well Data Analysis and Correlation

#### 5.3.1 BKLM-01

The gamma-ray (GR) data in figure 5.73 represents the amount of clay mineral in the rock sample. With higher GR comes higher clay mineral content. The GR data in BKLM-01 well showed a clear shallowing upward pattern. The next column showed the density (RHOB) and effective porosity (PHIE). The porosity of the reservoir can be calculated by assuming the matrix density and fluid density:

$$\Phi = \frac{\rho_{ma} - \rho_b}{\rho_{ma} - \rho_f} \quad \text{Eq. (1)}$$

$\Phi$  = Porosity

$\rho_{ma}$  = Matrix density

$\rho_b$  = Bulk density

$\rho_f$  = Fluid density

The slight separation of the RHOB and PHIE possible meant gas is present in the reservoir (PHIE > RHOB). It is presented as a yellow-colored area, which means the entire targeted section of the well has the potential to be a hydrogen reservoir. The next column in figure 5.73 is the water saturation. The water saturation usually is around 10~20%. However, at 1993m depth, where the GR is the highest, and the RHOB and PHIE are the lowest (0), VSH (shale volume) and VP (p-wave velocity) are both high in the well, which is shown in figure 5.73 as



well. Anhydrite content appears when VSH is high, which might present high evaporation. VSH is important in the research because it is vital for computing fluid content, formation porosity and formation permeability. The petro-porosity shows the result of thin sections analysis compared to PHIE. Although most of the analysis results match the well data, there are still some errors, which might be caused by sample selection. Since the samples are selected based on representativeness, they do not represent the whole section. The Marker2 separates the sequence 2 into fine-grained dolomicrite and coarse-grained grainstone. The average data of PHIE and RHOB based on Marker2 roughly align with the original datasets and the RT (resistivity). The RT represents the aqueous solution in the borehole fluids, vital for geochemical or microbiological reaction prediction in the reservoir rock.

### 5.3.2 BKLM-04

The GR in BKLM-04 well only showed a proper shallowing upward pattern at 1998-2007m and 1975-1998m. Above 1975m, no clear pattern can be seen (figure 5.74). However, like the BKLM-01 well, the entire researched well is potential hydrogen storage property. The PHIE and RHOB value also show that the entire column of the core is suitable for gas storage. Like BKLM-01, BKLM-04 well also has a water-saturated layer. However, instead of one, there are two water-saturated layers. One at ~2000m depth, and another at ~1945m. There is no VP value for BKLM-04 well, there are more peaks for VSH value, and there is also a lot more anhydrite/gypsum content in the BKLM-04, as shown in figure 5.74. The VSH peaks are correlated to the GR value. However, there is less correlation between RHOB/PHIE. Even though some errors remain, the petro-porosity from the quantitative analysis aligns with the PHIE better. Based on the lithology, the Marker2 in BKLM-04 separates sequence 1 and sequence 2 into two sub-sequences. The average data of PHIE and RHOB based on Marker2 also roughly align with the original dataset. However, BKLM-04 well does not provide resistivity data.

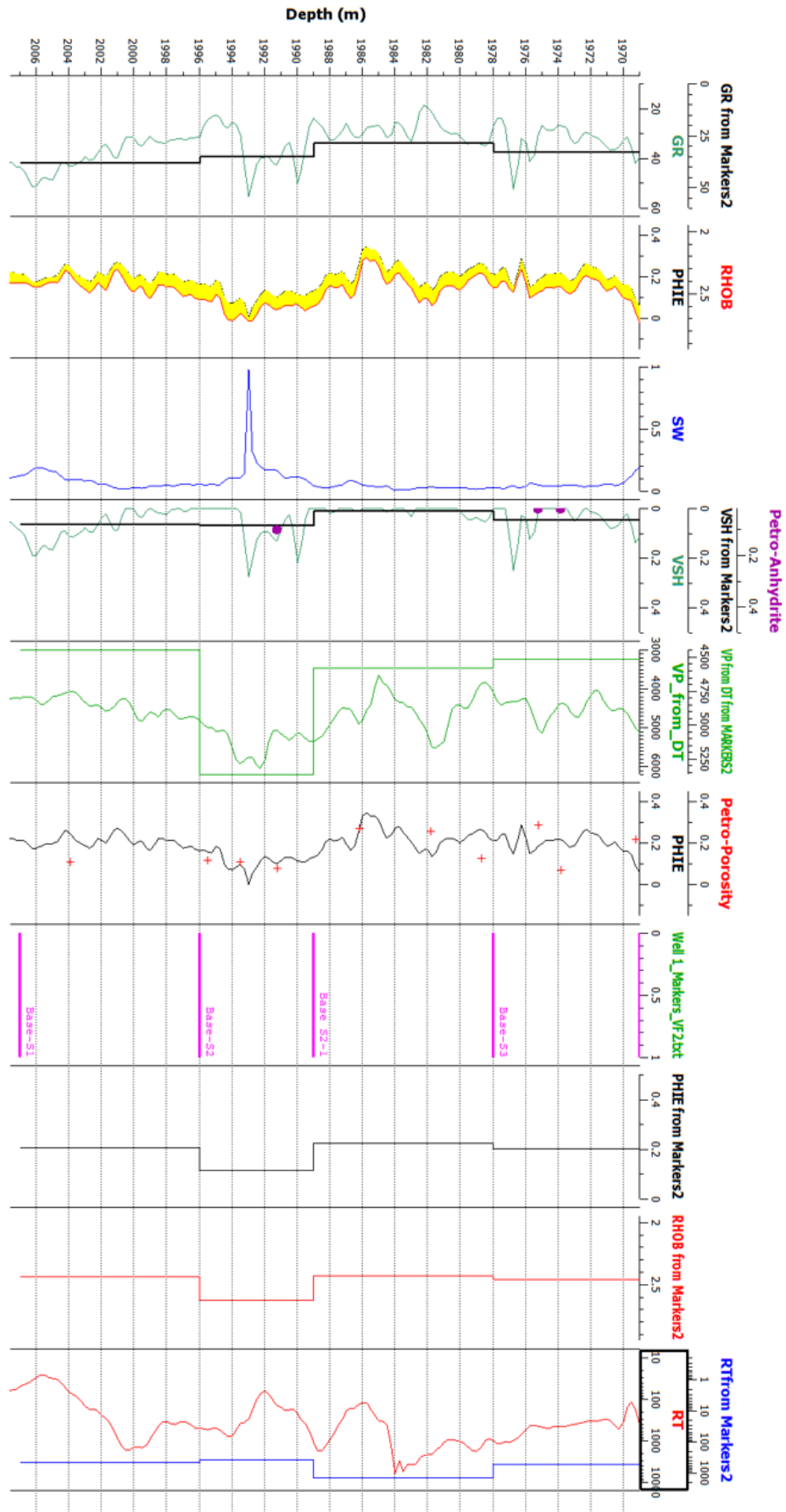


Figure 5.73. BKL01 wire logs.

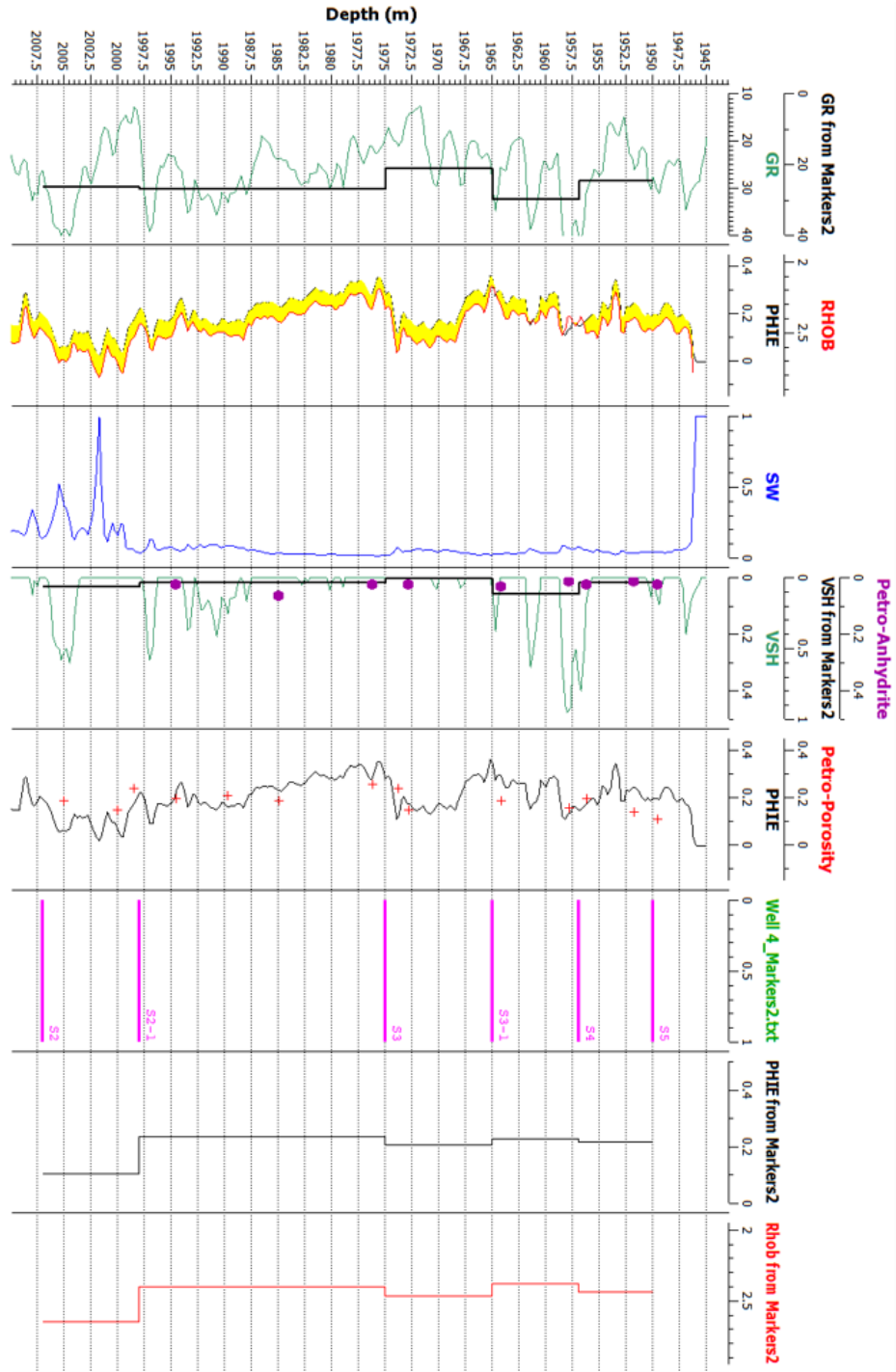


Figure 5.74. BKL04 wire line logs.



#### 5.4. Hydrogen Impact on reservoir

Hydrogen has a higher energy density per mass than methane and carbon dioxide at about 120MJ/kg. However, hydrogen has a lower density, which leads to a higher requirement for more volumetric storage capacity (Heinemann et al., 2021). However, hydrogen density increases with increasing pressure and depth. In a deeper reservoir, hydrogen storage has higher efficiency. Hydrogen injection also causes multiphase displacement of formation fluid, where the displacement is controlled by fluid and rock properties (fluid viscosity, density, compressibility, porosity and permeability). Furthermore, with the low density, injected hydrogen might float above brine and form a hydrogen cap below the caprock.

Since the injected hydrogen reacts with the free ions in brine in order to cause geochemical or microbiological reactions with the reservoir rock, it is important to understand the groundwater component. The groundwater component in table 3.2 is from different wells, but the groundwater in the Zechstein group should stay in equilibrium, so the groundwater component should also be the same in the Alkmaar field. According to table 3.2, the pH value is close to neutral to acidic, with a high concentration of sodium, calcium, magnesium, and potassium. This could be caused by the dissolution of the dolomite in the Z3 carbonate group. Equation 3.1 shows calcium sulphate can react with methane and produce calcite, hydrogen sulphide, and water at 80°C. Since the Alkmaar used to be a gas field, and the temperature at the Alkmaar field is 80°C, there might potentially be hydrogen sulphide in the reservoir before injecting hydrogen, which can cause potential leakage of H<sub>2</sub>S even before the operation of UHS. Furthermore, the molar solubility of hydrogen is higher than natural gas. Hence the one-time loss at the beginning of the operation is higher (De Lucia et al., 2015), and 1~3% of the injected hydrogen might mix with cushion gas (Srinivasan, 2006).

When injecting admixture with 0.5% of hydrogen, chemical reactions in the reservoir include methanogenic (eq. (3.2)), acid-forming (eq. (3.3)), and sulphate reducing (eq. (3.4)), where the reactions mentioned may potentially cost the loss of hydrogen. The sulphate reduction produces H<sub>2</sub>S that is toxic for the surface and the society if leaked. Iron sulphide (FeS) formation might reduce the permeability of the reservoir rock. However, the concentration of hydrogen is too low to have a significant impact on the reservoir rock. But the Alizarin Red S and Potassium Ferricyanide staining result showed that the dolomite reservoir lacks iron. Hence, there might be less free Fe<sup>2+</sup> ions in the brine water. On the other hand, when injecting admixture with 10%, the reaction includes methanogenesis (eq. (3.5)), sulphate reduction (eq. (3.6)), iron reduction (eq. (3.7)), and calcification (eq. (3.8)). The reactions also cause the loss in hydrogen. The calcification might turn the dolomite reservoir into calcite and cause potential migration through the reservoir rocks, which might lead to leakage of hydrogen. Furthermore, the geochemical reaction on the reservoir rock is slow for the DBI GUT report in 2017, which



means the impact of the geochemical in the reservoir rock might be less relevant. The non-polar nature of hydrogen limits the solubility in water, which also limits the change in pH value. Hence, the clay swelling caused by pH value might not be significant in the reservoir rocks.

The microbiological reaction is important to hydrocarbon reservoirs (oil/gas reservoirs). However, there are limited studies of the microbial in carbonate reservoir. The major microbials include: methanogens, sulphate-reducers, homoacetogenic bacteria, and iron (III) reducer, which the reactions are controlled by temperature, salt concentration, pH value, and substrate supply. The microbiological reactions cause the loss of  $H_2$ . Furthermore, the reaction might also form biofilms or mineral precipitation that might cause pore-clogging and lead to the reduction of porosity, permeability, and pore space. However, there are several uncertainties, like the non-culturability of subsurface microorganisms and the risk of allochthonous organisms from surface, surface gas or drilling fluid during storage operation.

According to Heinemann et al., in 2021, the hydrogen injection and reproduction lead to: (1) cyclical pressure change on intact and fault rock behaviour, (2) short- and long-term chemical interaction of hydrogen on intact rock and faults, (3) stress-strain-sorption on mechanical and transport behaviour, which all have an important effect on storage integrity. Injecting cold, pressurised hydrogen leads to changes in chemical, pressure, and temperature in the reservoir and nearby faults and injection wells. The impacts of hydrogen injection might possibly lead to deformation of reservoir, porosity reduction, reduced fluid flow, subsidence, and potential fault reactivation. Furthermore, clay swelling by sorption may also stress change in the reservoirs, caprocks, and faults. The swelling effects of clay minerals in the Z3 carbonate reservoir or the Z3 salt clay member lying above also may lead to permanent damage to the reservoir, porosity and permeability reduction, and potential deformation in the salt clay member that could possibly lead to the creation of leakage pathway.



## 6. Discussion

### 6.1. Characterization and inferred impact of the reservoir rocks

From the BKLM-01 stratigraphic log and table 5.1, the sequence of the core sample with the most reservoir rock potential is sequence 2, located between 1978-1996 meters (red-, green-, blue-, and orange-coloured rows in table 5.1) of true vertical depth. Within sequence 2, the reservoir can further be sub-divided into two sub-sequences, sequence 2-1 (1989-1996m) and sequence 2-2 (1978-1989m), which separates the fine/mid-grained dolomicrite (sequence 2-1, red-coloured row) and the grain/packstone (sequence 2-2, green- and blue-coloured row). According to the stratigraphic log, the best reservoir rock in the BKLM-04 well is located at 1972-1998m depth, at sequence 1. Like the BKLM-01 well, the sequence can be separated by the rock types. Sequence 1-1 is the fine-grained dolomicrite, and sequence 1-2 is mostly grainstone, which is the potential reservoir rock. From the petrographic analyses using the microscope, the packstone/grainstone generally has a fine grained dolomite matrix and cement, and the porosity is around 20% for both wells (table 5.1). However, in BKLM-01, larger dolomite cement can also be spotted, which means the carbonate rock underwent evaporation before dolomitization (figure 5.23). Interclasts were often seen in the thin sections (figure 5.25), where the larger clasts can even be spotted by eye (1-2 mm). The presence of these clasts means that the carbonate rocks were deposited in a subtidal/lagoon environment, where sudden sea-level changes happened often. On the other hand, the petrographic analysis of BKLM-04 also showed that the reservoir rocks are mostly packstone and grainstone. However, the samples in BKLM-04 had clay minerals in the carbonate samples (figure 5.39), and larger second phase anhydrite in the grains and in between the matrix that formed after the dolomitization (figure 5.44(b) and 5.49), which confirms the observation of the core samples that samples at BKLM-04 underwent more intense evaporation event after dolomitization.

The gamma-ray value of BKLM-01 from EasyTrace (figure 5.73) shows the lowest value at the depth of the sequence (1978-1989m), which fits the observation from the stratigraphic log and the petrographic analysis. When injecting a mixture of gas with 0.5% hydrogen into BKLM-01, no significant geochemical or microbiological reactions will happen because the hydrogen concentration is too low. When injecting a mixture with 10% hydrogen, hydrogen ions might react with the free  $SO_4^{2-}$  in the groundwater and produce hydrogen sulphide. However, the content of anhydrite/gypsum minerals is low in the BKLM-01 well. Only three thin section samples had a significant amount of sulfate minerals. Hence, there might not be enough free  $SO_4^{2-}$  in the fluid, for the hydrogen to react with. Furthermore, the carbonates buffer the reaction, so it is very unlikely for  $H_2S$  to be released from the reservoir. Unlike BKLM-01, the samples in BKLM-04 well contained more clay minerals according to gamma-ray value in figure 5.73 and 5.74. The clay minerals might swell if the pH value changes, which lowers the porosity and permeability, reducing the storage capacity. Furthermore, the samples also had



more anhydrite/gypsum minerals, which might lead to more free  $\text{SO}_4^{2-}$  anions in the dissolution, resulting in the creation of hydrogen sulphide, further impacting the society once leaked.

## 6.2. Characterization and inferred impact of the non-reservoir rocks

The non-reservoir rocks in BKLM-01 are located within sequence 1 and 3. In both stratigraphic log and petrographic analysis, the rock samples turned from fine-grained dolomicrite to mid/coarse-grained dolomicrite. At the top of the sequence, there were more anhydrite clasts (figure 5.19). Sequence 3 had a similar pattern. However, at ~1973 m, fine-grained dolomite and coarse-grained dolomite were separated by stylolite (figure 5.32). The stylolite acted as a boundary separating the fine and coarse-grained layers. The stylolite allowed seawater to flow in between two fine-grained layers, and the original carbonate rocks were allowed to grow larger before dolomitization. Large anhydrite crystals (1000  $\mu\text{m}$ ) can be found in the thin section (figure 5.32), suggesting that the deposition environment has high salinity. Larger anhydrite clasts can also be seen in sequence 3. It can be boldly proposed that sequence 3 had undergone more intense evaporation than sequence 1. The non-reservoir rocks in BLKM-04 were located at sequence 1-1, 2, 3, and 4 from the stratigraphic log and petrographic analysis. The top of sequence 2 (1957-1964m) was packstone/grainstone. However, the GR value at the section was almost the highest in the whole researched section. Hence, the sequence might not be the most ideal section for storage. The clay minerals in the section might swell when injecting hydrogen, therefore lowering the porosity and permeability of the storage and reducing the storage capacity. Furthermore, at 1972m depth, BLKM-04 also has the layer of very fine grained dolomicrite separated by stylolite. However, the thin section contains more anhydrite/gypsum clasts and moldic pore space, which can be assumed that the depositional environment contains more free sulphate for the salts to grow during the evaporation and diageneses.

The non-reservoir rocks generally shows higher GR and VSH values, where the peaks of GR and VSH were correlated. Anhydrite/gypsum minerals also appeared at the peak of both values. The type and amount of geochemical and microbiological reactions should be similar to the reservoir rock. BKLM-04 well also had high VSH values from 1987-2007 m and 1957-1962 m, and the high VSH value corresponds to the presence of anhydrite. The non-reservoir rocks were also the same dolomite as the reservoir rocks. Hence, the type and amount of geochemical and microbiological reaction should be the same as the reservoir rocks.

Furthermore, at the bottom of sequence 2, there is a water-saturated layer and a layer with the highest GR value. Only the clay minerals that have direct contact with moving fluid (injected admixture with hydrogen) in the rock will react (Schlumberger, 2022), the swelling lowers the reservoir porosity and permeability, and the reservoir rock mechanism might be weakened, therefore create leakage pathway. However, no swelling affect is observed at water saturated



layers (Heinemann et al., 2021). Furthermore, the diffusion rate of the clay decreases significantly when the clay is 100% water-saturated, which could prevent hydrogen from leaking for 100,00 years (DBI GUT, 2017).

### **6.3. Overall potential impact on Z3 carbonate hydrogen storage**

Overall, the stratigraphic logs created in this research shows exactly the same lithology as the well reports provided by TNO, in which the entire sections are dolomite. The BKLM-01 dataset did not include the stratigraphic log. However, the stratigraphic log created in this research (figure 5.8) is very similar to the log provided in the BKLM-04 well report (figure 5.7). With more diagenetic information of the core samples provided in this research, it might be useful for future research. The quantitative petrographic analysis shows more information about the diagenesis of the reservoir rocks. Based on the conventional microscope analysis results, it can be assumed that the carbonate rocks from both wells are dolomitized after the original deposition of the carbonate rocks. CL microscope analysis shows further information about the reservoir rocks dolomitized under uniformed conditions during the same burial event. However, even though the thin section samples are selected based on the representativeness of the core sample, there are still some errors that exist, which can be seen in figure 5.73 and 5.74.

The reservoir rocks, in general, are packstone/grainstone, with vugs, moldic porosity. The porosity of BKLM-01 is around 20%, and the porosity of BKLM-04 is slightly higher at around 20~25%. On the other hand, the non-reservoir rocks are mostly dolomicrite with porosity of 10~15%. Expect sequence 3 at the BKLM-04 well, which is a grainstone with porosity of around 25%. This grainstone sequence has high clay mineral content, which might absorb the injected hydrogen and lead to swelling that might reduce the porosity and permeability of the reservoir rock. The results performed by quantitative analysis are similar to the well data shown on the EasyTrace wire log, and the well report done by Acomo Netherlands B.V. However, only BKLM-04 has well documented well report with porosity, permeability, and fractures. The reason for the BKLM-01 well lacking documented report might be that the two well are only 14 meters apart from each other, and the other eight wells in the Alkmaar field are all close by (figure 4.1(b)). So, the operator did not measure all the well data since measuring the data might be expensive. The permeability of BKLM-04 mostly aligns with the porosity, and higher porosity comes with higher permeability. However, the fractures mostly appear at the less porous, non-reservoir property sequence of the well.

According to the DBI GUT report in 2017, the partial pressure in the UGS Grijskerk was 2 bar when injecting 0.5% of hydrogen in the admixture gas and 38.5 bar when hydrogen concentration was 10%, and the storage capacity was reduced by 0.6%. Besides the loss of the storage capacity, it is possible to lose hydrogen by the one-time loss during the operation and



mixing with cushion gas in the reservoir. However, 0.5% of hydrogen is too low to cause any significant reaction in the carbonate rock. It might not be the most efficient way to store hydrogen. Injecting admixture with 10% hydrogen is probably more efficient for storage, but it leads to more geochemical and microbiological reactions, where the most important reactions in the carbonate might be sulphate reduction and calcification. Sulphate reduction produces hydrogen sulphide, and calcification consumes dolomite to produce methane, water, and calcite, which might weaken the Z3 carbonate reservoir integrity. All the geochemical or microbiological reactions involving hydrogen led to loss in hydrogen, hence, loss in sustainable energy. Fortunately, as mentioned by Heinemann et al. in 2021, pure hydrogen is non-toxic, non-poisonous, and non-corrosive. Hence, the environmental risk is lower compared to CH<sub>4</sub> and CO<sub>2</sub>. Furthermore, using non-hydrogen gas can prevent injected hydrogen from mixing with the cushion gas and reduce the density contrast between hydrogen and the formation water. Depending on the alternative cushion gas used, it can reduce storage cost (CH<sub>4</sub>, N<sub>2</sub>), or greenhouse gas emissions (CO<sub>2</sub>) (Heinemann et al., 2021). However, there is not much research about the impact of hydrogen in carbonate reservoirs, since most of the hydrogen storages are in salt cavern. There are also more depleted sandstone oil/gas reservoirs in the Netherlands.



## 7. Conclusion

As a result, the carbonate reservoir in Alkmaar/Boekelermeer field can be considered a suitable reservoir property. This research project which is based on stratigraphic logging, quantitative petrography, well log interpretation/analysis, and possible chemical reactions can be broken down into the following three conclusions: (1) The potential of the Z3 carbonate reservoir at Alkmaar/Boekelermeer field; (2) The potential of the internal sealing layers of Z3 carbonate at Alkmaar/Boekelermeer field; (3) Uncertainties and future studies.

First of all, the potential of the Z3 carbonate reservoir at Alkmaar can be easily spotted from the RHOB/PHIE wire logs, which both researched wells were considered potential reservoir properties, and there were sequences of high porosity reservoir rock with low clay mineral and anhydrite/gypsum content, which might not react with brine water and injected hydrogen that might cause further damage to the reservoir rocks. There are two sequences in BKLM-01 and BKLM-04 that can be considered to be the best reservoir properties in the two wells. When injecting admixture with 10% hydrogen, the possible chemical reaction such as methanogenesis, sulphate reduction, iron reduction, and calcification can lead to hydrogen loss, and reservoir clogging caused by precipitation. However, the carbonate rock will buffer the geochemical reaction, where the injected hydrogen might be relatively stable in the reservoir rock.

The second conclusion can be proposed based on the GR value, where the sequences have higher clay minerals. The clay minerals tend to swell when the pH value changes, whereas injecting hydrogen might lead to the pH value in the reservoir. However, research has shown that due to the non-polar nature of hydrogen, it limits the solubility in water, causing no significant pH value change. Hence, no significant swelling. Furthermore, both wells lack clay minerals based on the quantitative analysis. There are also water-saturated layers in both wells below the potential reservoir rock. No swelling is observed in the water-saturated clay, and there is a sharp contrast between injected hydrogen and formation. It would be wise to use non-hydrogen cushion gas to reduce the huge difference. Therefore, it can be concluded that the potential of the internal seal within the reservoir rock is low.

Finally, more research must be done to understand the potential of the Z3 carbonate storage. Creating the correlation between the two well might be the next task for future researchers, as well as combining other well data (ALK-01, BKLM-02, -03, -05-09) to build an underground topographic map of the Alkmaar field, which can help to predict the total capacity of the reservoir since the original gas reservoir is smaller than the other oil/gas reservoir in the north of the Netherlands. Geochemical modelling is required. However, the modelling often ignored the reaction rate, which lead to overestimating the extent of the reaction. The report by DBI GUT in 2017 suggested that the clay rock seal in the Z3 ground still contained certain elements



that can react with hydrogen. It was highly recommended to perform laboratory experiments for possible microbiological reactions when injecting admixture with higher hydrogen concentration. Furthermore, it is also important to calculate the general reservoir integrity. For example, suppose the gypsum is dissolved. In that case, the pore space might collapse and impact the porosity and permeability, further lowering the accessibility of storage and the possibility of reproducing the injected gas. It is also important to consider the fault and seismic activities since this research ignored the impact of the faults in gas reservoirs. Therefore, it is important to calculate the abovementioned factors and the economic value before operating the hydrogen storage. Overall, BKLM-01 and -04 can be considered good reservoir properties, but more research must be done before starting the operation for hydrogen storage.



## 8. Reference

- CarbonBrief. 2021. Met Office: Atmospheric CO<sub>2</sub> now hitting 50% higher than pre-industrial levels. [ONLINE] Available at: <https://www.carbonbrief.org/met-office-atmospheric-co2-now-hitting-50-higher-than-pre-industrial-levels/#:~:text=Atmospheric%20CO2%20has%20been%20rising,levels%20from%201700%20to%202021..> [Accessed 17 June 2022].
- Chadwick, R.A., Livermore, R.A. and Penn, I.E., 1989. Continental Extension in Southern Britain and Surrounding Areas and Its Relationship to the Opening of the North Atlantic Ocean: Chapter 26: European-African Margins.
- Chen, L.L.Y., Katz, D.L. and Tek, M.R., 1977. Binary gas diffusion of methane-nitrogen through porous solids. *AIChE Journal*, 23(3), pp.336-341.
- DBI GUT, 2017. The Effects of hydrogen injection in natural gas networks for the Dutch underground storages.
- De Lucia, M., Pilz, P., Liebscher, A. and Kühn, M., 2015. Measurements of H<sub>2</sub> solubility in saline solutions under reservoir conditions: preliminary results from project H2STORE. *Energy Procedia*, 76, pp.487-494.
- Doornenbal, H. and Stevenson, A., 2010. Petroleum geological atlas of the Southern Permian Basin area. EAGE.
- Geluk, M.C., 2000. Late Permian (Zechstein) carbonate-facies maps, the Netherlands. *Netherlands Journal of Geosciences*, 79(1), pp.17-27.
- Griffioen, J., Verweij, H. and Stuurman, R., 2016. The composition of groundwater in Palaeogene and older formations in the Netherlands. A synthesis. *Netherlands Journal of Geosciences*, 95(3), pp.349-372.
- Götze, J., 2012. Application of cathodoluminescence microscopy and spectroscopy in geosciences. *Microscopy and Microanalysis*, 18(6), pp.1270-1284.
- Hangx, S., Bakker, E., Bertier, P., Nover, G. and Busch, A., 2015. Chemical–mechanical coupling observed for depleted oil reservoirs subjected to long-term CO<sub>2</sub>-exposure—A case study of the Werkendam natural CO<sub>2</sub> analogue field. *Earth and Planetary Science Letters*, 428, pp.230-242.
- Heinemann, N., Alcalde, J., Miocic, J.M., Hangx, S.J., Kallmeyer, J., Ostertag-Henning, C., Hassanpouryouzband, A., Thaysen, E.M., Strobel, G.J., Schmidt-Hattenberger, C. and Edlmann, K., 2021. Enabling large-scale hydrogen storage in porous media—the scientific challenges. *Energy & Environmental Science*, 14(2), pp.853-864.
- Howie, R.A., Zussman, J. and Deer, W., 1992. An introduction to the rock-forming minerals. London, UK: Longman.
- James, N., 1977. Facies models 8. Shallowing-upward sequences in carbonates. *geoscience Canada*, 4(3), pp.126-136.
- JMicroVision. 2019. User-friendly software for analyzing large images. [ONLINE]



Available at: <https://jmicrovision.github.io/>. [Accessed 11 April 2022].

- Juez-Larré, J., Van Gessel, S., Dalman, R., Remmelts, G. and Groenenberg, R., 2019. Assessment of underground energy storage potential to support the energy transition in the Netherlands. *First Break*, 37(7), pp.57-66.
- Juez-Larré, J., Van Gessel, S., Dalman, R., Remmelts, G. and Groenenberg, R., 2019. Assessment of underground energy storage potential to support the energy transition in the Netherlands. *First Break*, 37(7), pp.57-66.
- Kombrink, H., Ten Veen, J.H. and Geluk, M.C., 2012. Exploration in the Netherlands, 1987-2012. *Netherlands Journal of Geosciences*, 91(4), pp.403-418.
- Liu, W., Muhammad, N., Chen, J., Spiers, C.J., Peach, C.J., Deyi, J. and Li, Y., 2016. Investigation on the permeability characteristics of bedded salt rocks and the tightness of natural gas caverns in such formations. *Journal of Natural Gas Science and Engineering*, 35, pp.468-482.
- Nader, F.H., 2017. Multi-scale quantitative diagenesis and impacts on heterogeneity of carbonate reservoir rocks (pp. 15-69). Springer International Publishing.
- NLOG. 2020. Boreholes. [ONLINE] Available at: <https://www.nlog.nl/datacenter/brh-overview?lang=en>. [Accessed 9 April 2022].
- Paterson, L., 1983. The implications of fingering in underground hydrogen storage. *International journal of hydrogen energy*, 8(1), pp.53-59.
- Peryt, T.M. and Scholle, P.A., 1996. Regional setting and role of meteoric water in dolomite formation and diagenesis in an evaporite basin: studies in the Zechstein (Permian) deposits of Poland. *Sedimentology*, 43(6), pp.1005-1023.
- Pray, H.A., Schweickert, C.E. and Minnich, B.H., 1952. Solubility of hydrogen, oxygen, nitrogen, and helium in water at elevated temperatures. *Industrial & Engineering Chemistry*, 44(5), pp.1146-1151.
- Schlumberger. 2022. Clay Swelling. [ONLINE] Available at: [https://glossary.oilfield.slb.com/en/terms/c/clay\\_swelling#:~:text=A%20type%20of%20damage%20in,exchange%20or%20changes%20in%20salinity..](https://glossary.oilfield.slb.com/en/terms/c/clay_swelling#:~:text=A%20type%20of%20damage%20in,exchange%20or%20changes%20in%20salinity..) [Accessed 13 June 2022].
- Srinivasan, B. S. (2006). The impact of reservoir properties on mixing of inert cushion and natural gas in storage reservoirs. Morgantown, West Virginia, US: Department of Petroleum & Natural Gas Engineering, College of Engineering and Mineral Resources, West Virginia University.
- TNO-GDN (2022). Grey Salt Clay Member. In: Stratigraphic Nomenclature of the Netherlands, TNO – Geological Survey of the Netherlands. Accessed on 04-04-2022 from <http://www.dinoloket.nl/en/stratigraphic-nomenclature/grey-salt-clay-member>.
- TNO-GDN (2022). Z3 Anhydrite-Carbonate Member. In: Stratigraphic Nomenclature of the Netherlands, TNO – Geological Survey of the Netherlands. Accessed on 04-04-2022 from <http://www.dinoloket.nl/en/stratigraphic-nomenclature/z3-anhydrite-carbonate->



[member](#)

- TNO-GDN (2022). Z3 Carbonate Member. In: Stratigraphic Nomenclature of the Netherlands, TNO – Geological Survey of the Netherlands. Accessed on 04-04-2022 from <http://www.dinoloket.nl/en/stratigraphic-nomenclature/z3-carbonate-member>.
- TNO-GDN (2022). Z3 Fringe Claystone Member. In: Stratigraphic Nomenclature of the Netherlands, TNO – Geological Survey of the Netherlands. Accessed on 05-04-2022 from <http://www.dinoloket.nl/en/stratigraphic-nomenclature/z3-fringe-claystone-member>.
- TNO-GDN (2022). Z3 Fringe Sandstone Member. In: Stratigraphic Nomenclature of the Netherlands, TNO – Geological Survey of the Netherlands. Accessed on 05-04-2022 from <http://www.dinoloket.nl/en/stratigraphic-nomenclature/z3-fringe-sandstone-member>.
- TNO-GDN (2022). Z3 Main Anhydrite Member. In: Stratigraphic Nomenclature of the Netherlands, TNO – Geological Survey of the Netherlands. Accessed on 04-04-2022 from <http://www.dinoloket.nl/en/stratigraphic-nomenclature/z3-main-anhydrite-member>.
- TNO-GDN (2022). Z3 Salt Member. In: Stratigraphic Nomenclature of the Netherlands, TNO – Geological Survey of the Netherlands. Accessed on 05-04-2022 from <http://www.dinoloket.nl/en/stratigraphic-nomenclature/z3-salt-member>
- Van Adrichem Boogaert, H.A. and Burgers, W.F.J., 1983. The development of the Zechstein in the Netherlands. In Petroleum Geology of the southeastern North Sea and the adjacent onshore areas (pp. 83-92). Springer, Dordrecht.
- Van Der Baan, D., 1990. Zechstein reservoirs in the Netherlands. Geological Society, London, Special Publications, 50(1), pp.379-398.
- Van Wees, J.D., Stephenson, R.A., Ziegler, P.A., Bayer, U., McCann, T., Dadlez, R., Gaupp, R., Narkiewicz, M., Bitzer, F. and Scheck, M., 2000. On the origin of the southern Permian Basin, Central Europe. Marine and Petroleum Geology, 17(1), pp.43-59.